Cavity Ring-down Spectroscopy of Nitric Oxide

Vincent Kan Shuali
Mississauga, Ontario, Canada

B.S., University of Toronto, 2008

A Thesis presented to the Graduate Faculty
of the University of Virginia in Candidacy for the Degree of
Master of Science

Department of Physics

University of Virginia
May, 2015

_____

_____

_____

Table of Contents

Table of Figures

Acknowledgements

As I finish my graduate work at the University of Virginia, I'd like to thank my advisor Kevin K. Lehmann for the years of advising and support. Without his vast knowledge of spectroscopy, physics, and general knowledge about the world, I would not be here today. My sincerest gratitudes go to Dr. Vitali Stsiapura, my collaborator on this project. Thanks for being patient with me and working so hard and putting so much effort into our project. I'd like to thank Dr. Benjamin Gaston, our project's co-PI for your biological expertise and helping to secure our grant. I'd also like to thank Prof. Robert Jones for lending his time and energy to teach me how to use a frequency comb. I'd like to thank Prof. Patrick Hopkins for letting me share his lab space and tools. Profs. Charles Sackett, Despina Louca, and Nilanga Liyanage, thank you for advising me through my graduate studies in the Physics department. Dr. Joseph Hodges, thank you for showing me your lab at NIST and helping me understand frequency-stabilized cavity ring-down. Prof. Millard Alexander and Dr. Jacek Kłos for helping me understand molecular collision theory. I'd like to thank Dr. Sam Crivello at Daylight Solutions for helping me learn to use and diagnose problems with the ec-QCL laser, George Perry from Perry Amplifier for helping me diagnose electronics issues, Dr. Xunchen Liu at the University of Alberta for pointers on how to use a Herriott cell. I'd like to thank the undergraduate students who assisted in my research and taught me a thing or two about life: Ahmed Ragab, Jennifer Finelli (nee Veldhuyzen), George Schwartz, and Dominic DeLotto. I'm grateful to have my labmates both present and past: Dr. Mausumi Goswami, thanks for being a role model and mentor to me. Dr. Robert Fehnel, thanks for showing me around when I first came in and for tolerating my initial

cluelessness with vacuum technology. Dr. Shaoyue (Luna) Yang, thanks for sharing your advice on programming and lab skills. Thanks also to the newer lab mates: Mingyun Li, Mary Rad, and Chris Nichols, as well as former lab mates I wish I had more time to meet: Dr. Yongxin Tang, Dr. Quanli Gu, Alex Wu, Eun Yi, and Dr. Paul Johnston, and Dr. George Tikhonov. In addition, I'd like to thank some graduate students who have assisted in my research over the years: Dr. Jirakan Nunkaew, Dr. Hyunwook Park, Dr. Monica McEntee, Dr. Lynn Mandeltort, Dr. Nathan Seifert, Dr. Robert Leonard, and Dr. Brent Harris. I'd like to thank the rest of my research committee, Prof. Bellave Shivaram and Prof. Thomas Gallagher for their advice and criticism of my research. I'd also like to thank Prof. Gallagher for advising me my first summer here. Many thanks go to my former research supervisors Prof. Vitaly Kresin at USC, Prof. Walter Duley at the University of Waterloo, and Prof. Joseph Thywissen at the University of Toronto. Thanks also go to the amazing staff at the Department of Physics: Dawn Shifflett, Tammie Shifflett, Beth Guyton (nee Orser), Suzie Garrett, Chris Floyd, David Wimer, Vicky Ingram, and Helen McLaughlin. I'm grateful for the career advice from Dr. Phil Trella at UVa and Dr. Nada O'Brien at JDS Uniphase. And thank you to my friends and family I've met in Charlottesville for the emotional support throughout my years here at UVa, in alphabetical order by the last letter of their first name:

Rebecca, Jessica, Annika, Svetlana, Ilya, Dale, Andre, Sarah, Zach, Josh, Seth, Kai, Mordi, Rachel, Joel, Sam, Ben, Austin, Andon, Jon, Markus, Tonu, Debby, and Liz, and my friends at CBI, in my UU covenant group, and in my book club.

Introduction

In 1988, O'Keefe and Deacon developed the method of spectroscopy known as cavity ring-down. This method of spectroscopy measures the decay rate of light within an optical cavity, rather than the absolute absorption of light by a sample, allowing, to first order, insensitivity to laser light intensity compared to traditional laser absorption spectroscopy [1] .

S-nitrosothiols are compounds containing nitric oxide (NO) that play an important role in signaling in biological systems. The level of S-nitrosothiols is an important diagnostic tool for certain illnesses and disorders including cancer and cystic fibrosis. Nitric oxide serves as an important vasodilator and levels of nitric oxide in the lungs can be used to diagnose asthma. An important research goal in our project is to be able to achieve a limit of detection (LOD) in the range of parts per trillion, allowing the measurement of S-nitrosothiol / nitric oxide levels in individual cells, providing a minimally invasive method of diagnosing medical conditions [2], [3].

Kosterev, et al., previously measured nitric oxide with continuous wave cavity ring-down spectroscopy, and we improved on his group's work by using an AOM for faster shutoff times. We are also using a room temperature thermoelectrically-cooled external cavity quantum cascade laser rather than a liquid-nitrogen-cooled DFB-type QCL, which we hoped would be more stable than the DFB QCL (linewidth of 4 MHz over 0.500 μs), but turned out to be comparable. Furthermore, we developed a delivery system capable of photolyzing biological samples. [4]

This research project also aims to observe Lamb dips, a sub-Doppler saturated absorption feature at the center of a Doppler broadened line observed when two counter-propagating beams excite the same velocity class of molecules and saturate the absorption line. The observation of Lamb dips at different pressures and with noble gases will elucidate the collision kernel of NO with itself and these gases. As nitric oxide is present in trace amounts in the atmosphere, developing an empirical model for pressure broadening and lineshape modification will allow for more precise measurements of NO content in the atmosphere.

The present work describes the construction of a mid-infrared cavity ring-down spectroscopy (CRDS) apparatus, used to measure the concentration of nitric oxide in both artificially created NO/He gas mixtures and in biological samples, preliminary results, and future experiments. Results are compared with direct laser absorption spectroscopy using a Herriot multi-pass astigmatic cell. The challenges in building a robust optical instrument in an optical region (> 5 μm) where many conventional mid-infrared materials are not effective will be explained along with methods used to overcome such obstacles. An introduction to the theory and operation of the instrument as well as a model for saturated cavity ringdown decay will be presented. This writing documents the work done by myself and my collaborator Vitali Stsiapura.

Theoretical Background

Principles of cavity ring down spectroscopy

In conventional direct laser absorption spectroscopy, laser light of intensity I_0 resonant with an electronic, vibrational, or rotational transition of the gas is passed through a sample of concentration N (number per volume) and optical path length L. In the limit of where the upper state population $N_{upper} << N_{lower}$, the light intensity detected after the gas cell follows the Beer-Lambert law:

$$I = I_0 e^{-\sigma NL} \tag{1}$$

where σ is the absorption cross section of the transition. The optical depth τ is defined as the negative logarithm of intensity, with a related quantity A the absorbance:

$$\tau = -ln\frac{I}{I_0} = \sigma NL = A\,ln10 \tag{2}$$

A quantity that scales proportionately with the number density and path length. Detection of τ ≈ 0, or equivalently, concentrations of gas that are very small compared with σ require extraordinary sensitivity of the detector, light intensity well above the shot noise limit, and low fluctuations of the laser intensity itself.

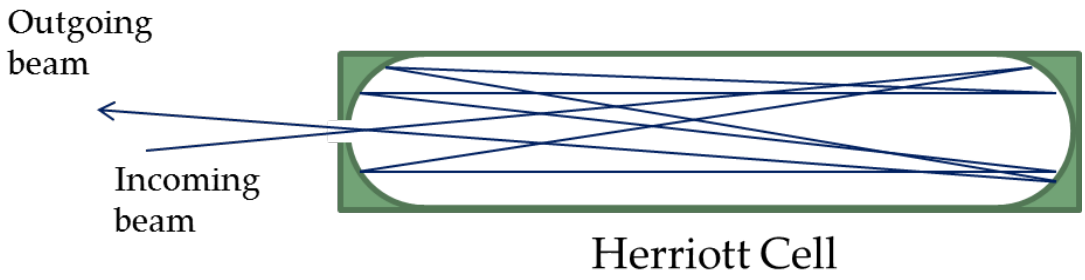

Figure 1: Schematic picture of a multi-pass cell

Our initial experiments used this type of spectroscopy with a type of gas cell called a Herriott cell. A Herriott cell achieves a long optical path by having light entering the cell bounce many times (multi-pass) between two mirrors at the ends of the cell before exiting at a hole in the cell. A Herriott cell differs from a White cell in that the entrance and exit beams pass through the same hole, allowing for more precise alignment of the cell [5]. Our Herriott cell is a New Focus 5612 astigmatic mirror cell aligned for 182 passes, leading to a 100 m long optical path length in a volume of 3.2 L. The astigmatic mirrors lead to the light more evenly sampling the mirrors by tracing out a Lissajou pattern as it goes from the first pass to the 182nd pass.

Cavity ring-down spectroscopy overcomes the need for high light intensity and low fluctuations of the laser intensity itself.

Figure 2: Constructive interference of the electric field of light in a resonant cavity

In cavity ring-down spectroscopy, light enters an optical cavity formed by two mirrors of very high reflectivity (R > 99.9%). If the length of the cavity is an integral number of half wavelengths of light, a standing wave forms within the cavity, resulting in a dramatically larger intensity of light within the cavity compared to the intensity entering the cavity. The intensity can be calculated by considering the constructive interference of light on successive passes. If light enters the cavity with an intensity I_0 and electric field E_0, E_0t will be transmitted, where $t=\sqrt{T}$. The light will then reflect twice before returning to constructively interfere, having $E = E_0tr^2$ in electric field strength, where $r=\sqrt{R}$. Two reflections later, the light will again constructively interfere, with $E = E_0tr^4$. This series can be summed in a geometric series to yield:

$$E_{intracavity}=E_0t+E_0tr^2+E_0tr^4+\ldots=\frac{E_0t}{1-r^2} \quad (3)$$

Since light intensity is proportional to E^2:

$$I_{intracavity}=\frac{I_0t^2}{1-r^2}=\frac{I_0T}{(1-R)^2} \quad (4)$$

Likewise, the electric fields of every pass transmitted through the cavity can be summed:

$$E_{transmit}=E_0t^2+E_0t^2r^2+E_0t^2r^4+\ldots=\frac{E_0t^2}{1-r^2} \tag{5a}$$

$$I_{transmit}=\frac{I_0T^2}{(1-R)^2}=I_{intracavity}T \tag{5b}$$

If the laser light source is shut off, the intensity of light within the cavity will decay at a rate of:

$$k_0=\frac{c(1-R)}{L} \tag{6}$$

where L is the length of the cavity. Thus:

$$I(t)=I(t=0)e^{-k_0t} \tag{7}$$

An alternative to the concept of a decay rate is a time constant τ that light takes to decay to 1/e of its original value.

$$\tau_0=\frac{1}{k_0} \tag{8}$$

When gas is added to the cavity, the rate of the extinction of light is increased to:

$$k=\frac{c(1-R+\alpha L)}{L} \tag{9}$$

where α is the absorption coefficient, which is, in the non-saturated absorption limit $\alpha=\sigma N$.

This can be used to measure the concentration of gas in a sample. To first order, the decay rate is independent of the initial intensity of the light I_0, thus allowing this method to be insensitive to intensity fluctuations.

The method of cavity ring-down spectroscopy has an additional advantage in that frequency fluctuations of the laser are filtered out. The length of the cavity dictates what frequencies will be resonant in the cavity and thus be amplified in intensity. If the frequency of light changes so that it is no longer resonant with the cavity, very little light will be coupled through the cavity and detected by the detector. This frequency filtering means that the change in σ with frequency in a single measurement is not as important as with direct laser absorption spectroscopy.

Theory of Optical Cavities

In the simplest theory of the propagation of light, ray optics, an optical cavity is where light bounces back and forth between a set of mirrors ad infinitum:

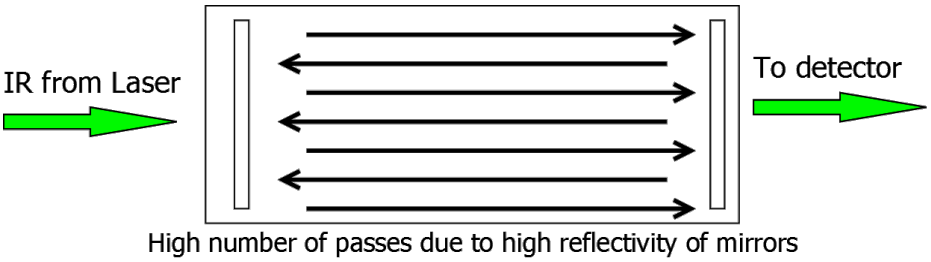

Figure 3: Schematic diagram of Fabry-Pérot interferometer

A slightly more complete theory of propagation incorporates the wave nature of light by considering the phase of a propagating light beam. In this model, one can see that in order for the light intensity to build up within the cavity, the wavelength of light must be a factor of the length of the cavity formed by the optical elements, in this diagram consisting of the two super mirrors:

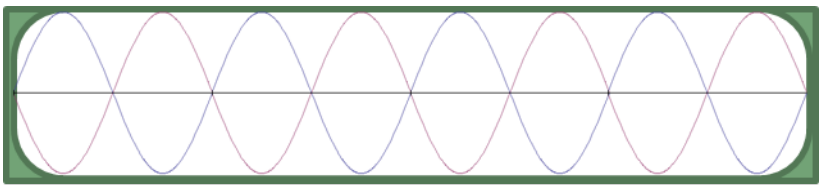

Figure 4: Standing wave pattern within a Fabry-Pérot interferometer

Another way of phrasing this condition is that the frequency of light must be an integral multiple of a quantity known as the free spectral range (FSR). This is in order to form a standing wave. The free spectral range of an etalon is given by:

$$FSR = \frac{c}{2nL} \tag{10}$$

where n is the refractive index of the material between the mirrors of the etalon, in our case air (n ≈ 1), and L the distance between the two etalon mirrors.

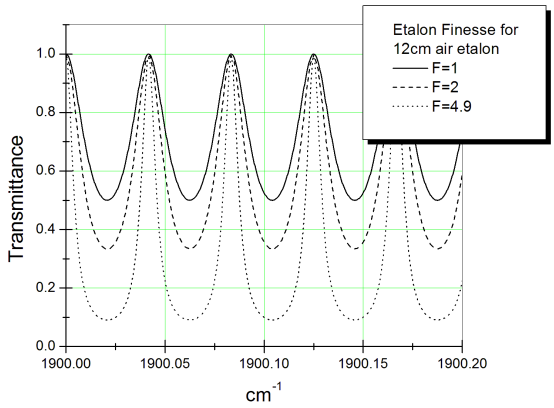

Figure 5: Transmittance as a function of light frequency, at various finesses

For two perfectly reflecting mirrors (i.e. R = 1), this equation is exactly true. However for real mirrors, the result of having R < 1 leads to a small range of frequencies around each multiple of

the FSR being able to build a standing wave within the cavity. The range of frequencies describes the width of the cavity resonant mode, given by

$$\Delta\nu = \frac{FSR}{\mathscr{F}} \tag{11}$$

with $\mathcal{F}$ called the finesse of the optical cavity given by:

$$\mathcal{F} = \frac{\pi}{2\arcsin\left(\frac{1}{F}\right)}; \tag{12a.}$$

where $F = \frac{4R}{(1-R)^2}$ (12b.)

For high reflectivities, we use the approximation:

$$\mathcal{F} = \frac{\pi\sqrt{R}}{1-R} \tag{13}$$

A narrow width allows the cavity to serve as a frequency filter as described in the previous section.

An even more complete model for the propagation of a laser beam is physical optics, incorporating the finite spread of the beam in the transverse direction. Light, as a form of electromagnetic radiation, propagates according to the following wave equation derived from Maxwell's equations:

$$\frac{1}{c^2}\frac{\partial^2 E(\vec{r},t)}{\partial t^2} = \nabla^2 E(\vec{r},t) \tag{14}$$

If we assume that E can be separated into a spatial part and a time dependent part:

$$E(\vec{r},t)=A(\vec{r})T(t) \tag{15}$$

Then both sides of wave equation are constant and can be set equal to each other.

$$\frac{1}{T(t)c^2}\frac{\partial^2 T(t)}{\partial t^2}=\frac{\nabla^2 A(\vec{r})}{A(\vec{r})}=-k^2 \tag{16}$$

The temporal part admits the familiar sine and cosine functions as solutions.

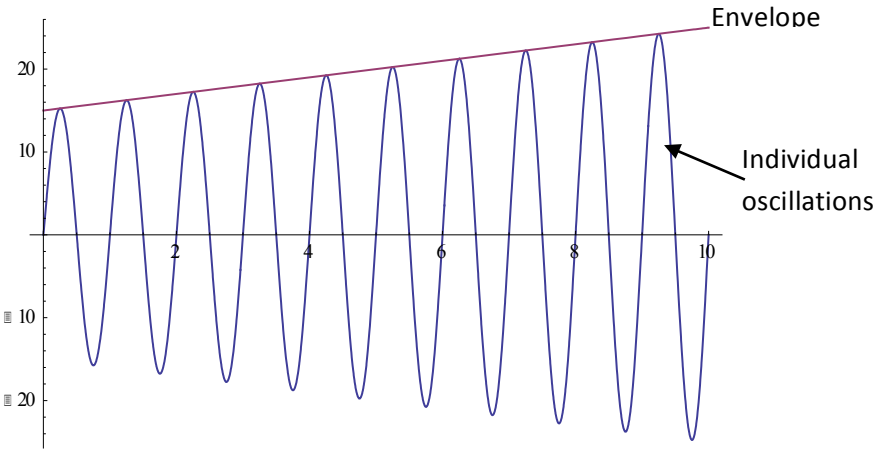

Figure 6: Diagram of amplitude of envelope varying slowly compared to oscillations

If we focus on the spatial part, this is known as the Helmholtz equation. Assuming that the amplitude (i.e. envelope) of the electric field varies slowly compared to the individual oscillations of the E-M wave, i.e.

$$\left|\frac{dA(\vec{r})}{dz}\right| \ll |kA(\vec{r})| \tag{17}$$

We can write A(r) = A(x, y, z) in the following form, separating out the z-part:

$$A(\rho,z)=A(\rho)e^{ikz} \tag{18}$$

where $\rho^2 = x^2 + y^2$, the cylindrical coordinate displacement from the propagation axis z.

Then the following approximation can also be made:

$$\left|\frac{d^2A(\vec{r})}{dz^2}\right| \ll \left|k\frac{dA(\vec{r})}{dz}\right| \tag{19}$$

This is known as the paraxial approximation. By substituting the equation for A(ρ, z) into the Helmholtz equation and ignoring the $\frac{d^2A(\vec{r})}{dz^2}$ term, the Helmholtz equation becomes:

$$\frac{d^2A(\vec{r})}{dx^2} + \frac{d^2A(\vec{r})}{dy^2} + -2ik\frac{dA(\vec{r})}{dz} = 0 \tag{20}$$

This admits the following solution:

$$A(\rho, z) = A_0\frac{w_0}{w(z)}\exp\left(\frac{-\rho^2}{w(z)^2} - ikz - ik\frac{\rho^2}{2R(z)} + i\zeta(z)\right) \tag{21}$$

With these being the definitions of w(z) and R(z):

$$w(z) = w_0\sqrt{1+\left(\frac{z_R}{z}\right)^2} \tag{22a}$$

$$R(z) = z\left(1+\left(\frac{z_R}{z}\right)^2\right) \tag{22b}$$

The beam's effective transverse size changes with z, from a minimum at the z position known as the waist, toward a size that approaches a linear limit with z at large displacements of z. We define the Rayleigh range z_R as the z displacement from the beam waist at z = 0 where

$w(\pm z_R) = \sqrt{2}w_0$, which occurs at $z_R = \frac{\pi w_0^2}{\lambda}$.

The equation for A(ρ, z) shows that the intensity of such a beam falls off as a Gaussian of width w(z) as one moves transversely away from the propagation axis. Unlike a plane wave, there is a radius of curvature R(z) of the wave fronts that changes with z, which effectively leads to a change in phase of

$$\Delta\phi = \frac{k\rho^2}{2R(z)} \tag{23}$$

as one moves transversely away from the propagation axis. In addition, the phase of the beam is not given exactly by ikz like a plane wave, but is modified by the factor ζ:

$$\zeta(z) = \arctan\left(\frac{z}{z_R}\right) \tag{24}$$

Which is known as the Gouy phase shift. The equation of the propagation of the Gaussian beam can be made more compact by introducing the complex number q(z), known as the complex beam parameter, defined as follows:

$$\frac{1}{q(z)} = \frac{1}{R(z)} - i\frac{\lambda}{\pi w(z)^2} \tag{25}$$

The propagation of a Gaussian beam throughout a system composed of lenses, optical media, and mirrors can be modeled by changing the complex beam parameter with a function of the form:

$$q_{out} = \frac{Aq_{in} + B}{Cq_{in} + D}, \tag{26}$$

whose parameters ABCD can be expressed in matrix form: $\begin{pmatrix} A & B \\ C & D \end{pmatrix}$

Passing through free space of length d is equivalent to changing the complex beam parameter by:

$$q_{out} = q_{in} + d \tag{27}$$

which is equivalent to defining ABCD as:

$$M_D = \begin{pmatrix} 1 & d \\ 0 & 1 \end{pmatrix} \tag{28}$$

Propagation through a thin lens of focal length f or equivalently a mirror of radius of curvature 2f, is equivalent to changing the complex beam parameter by:

$$\frac{1}{q_{out}} = \frac{1}{q_{in}} - \frac{1}{f} \Rightarrow q_{out} = \frac{q_{in}}{-\frac{q_{in}}{f} + 1} \tag{29}$$

Which is equivalent to defining ABCD as:

$$M_L = \begin{pmatrix} 1 & 0 \\ -\frac{1}{f} & 1 \end{pmatrix} \tag{30}$$

Bouncing off a concave mirror of radius of curvature R is equivalent to having an ABCD matrix of the form:

$$M_M = \begin{pmatrix} 1 & 0 \\ -\frac{2}{R} & 1 \end{pmatrix} \tag{31}$$

The ABCD matrix of a series of optical elements and free space can be obtained by matrix multiplication of each element's ABCD matrix. For example, propagation of a beam a free space distance of z_1, then through a lens of focal length f_1, followed by a free space of distance d, then

a lens of focal length f_2, followed by the distance z_3 would be represented as:

$$M_{propag} = \begin{pmatrix} 1 & z_3 \\ 0 & 1 \end{pmatrix} \begin{pmatrix} 1 & 0 \\ -\frac{1}{f_2} & 1 \end{pmatrix} \begin{pmatrix} 1 & d \\ 0 & 1 \end{pmatrix} \begin{pmatrix} 1 & 0 \\ -\frac{1}{f_1} & 1 \end{pmatrix} \begin{pmatrix} 1 & z_1 \\ 0 & 1 \end{pmatrix} = \begin{pmatrix} A_{propag} & B_{propag} \\ C_{propag} & D_{propag} \end{pmatrix}$$

$$= \begin{pmatrix} 1 - f_2 \cdot z_3 - f_1(z_3 + d(1 - f_2 \cdot z_3)) & z_3 + d(1 - f_2 \cdot z_3) + z_1(1 - f_2 \cdot z_3 - f_1(z_3 + d(1 - f_2 \cdot z_3)) \\ -f_2 - f_1(1 - d \cdot f_2) & 1 - d \cdot f_2 + (-f_2 - f_1(1 - d \cdot f_2))z_1 \end{pmatrix}$$

(32)

An optical cavity is a series of optical elements whose equivalent transfer function $q_{out} = \frac{Aq_{in}+B}{Cq_{in}+D}$ reproduces the initial entering complex beam parameter q_{in} after one or more passes, leading to, in the absence of mirror losses and absorption, an indefinitely stable beam size and radius of curvature.

Stability of optical cavities

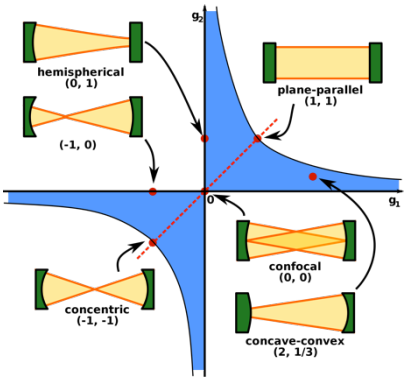

Figure 7: Region of stability of optical cavities in g_1-g_2 space[6]

A typical cavity is formed by two mirrors of radii of curvature R_1 and R_2 respectively, separated by a length of space L. Such a cavity can only be stable for certain ranges of R_i and L, as indicated by the diagram above, with g defined as:

$$g = 1 - \frac{L}{R} \tag{33}$$

A given stable cavity will admit a beam of a certain radius of curvature and beam size, i.e. a specific complex beam parameter. Intuitively, the beam must have the property that wavefronts do not interfere with previous passes of the beam, requiring wavefronts to be parallel to each reflecting surface of the cavity. The entering beam must be manipulated through the uses of lenses and mirrors in order to produce the correct complex beam parameter when entering the cavity, a process known as mode-matching.

Resonant modes of a cavity

The function:

$$A(\rho, z) = A_0 \frac{w_0}{w(z)} \exp\left(\frac{-\rho^2}{w(z)^2} - ikz - ik\frac{\rho^2}{2R(z)} + i\zeta(z)\right) \tag{34}$$

with appropriate w(z), R(z), and $\zeta(z)$ describes one possible solution for propagation of an electromagnetic wave within the optical cavity. It describes a "TEM_{00}" mode, i.e. one where there are no electric or magnetic nodes transverse to the optical axis z. As one moves away from the optical axis, the electric and magnetic fields of light fall off according to the Gaussian distribution. Because the cavity acts as a waveguide that constrains light in the transverse direction, it also admits other solutions for A(z) that have nodes in their electric and magnetic fields. These are known as higher-order modes, each mode being denoted by TEM_{nm}, where n and m denote the number of modes in the x- and y- direction respectively, perpendicular to the optical axis z. The electric and magnetic fields as a function of x and y displacement are the Hermite polynomials seen in solutions of the quantum harmonic oscillator.

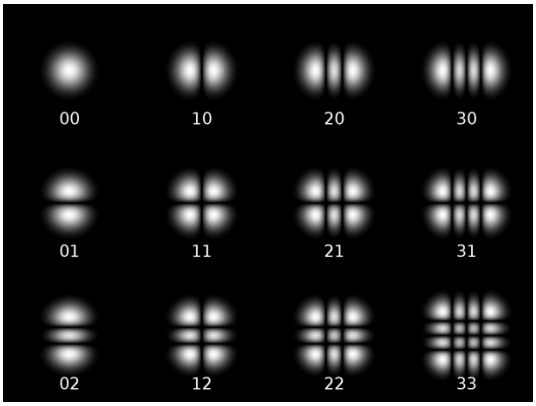

Figure 8: Transverse Electric and Magnetic Modes[7]

A real laser beam is not a pure Gaussian beam, which is a pure TEM_{00} mode. A beam can be decomposed as a linear combination of higher order TEM_{nm} modes. In terms of frequency, longitudinal resonant modes of a cavity are separated by the free spectral range (FSR). However, transverse modes TEM_{nm} are separated by:

$$\Delta\nu_{transv} = \frac{c}{2\pi L}[\zeta(z_{M1}) - \zeta(z_{M2})] \tag{35}$$

where $\zeta(z_{M1})$ and $\zeta(z_{M2})$ are the Gouy phase shifts at the first and second mirror of the cavity respectively. Increasing either m or n by one requires a shift in laser frequency of $\Delta\nu_{trans}$ to be excited.

By solving for the Rayleigh range z_R that would allow a standing wave pattern in the cavity, i.e. the phase fronts of the Gaussian beam match those of the mirrors, we can derive that:

$$z_R{}^2 = \frac{L(-R_1 - L)(R_2 - L)(R_2 - R_1 - L)}{(R_2 - R_1 - 2L)^2} \tag{36}$$

[8]

where R_i are the radii of curvature of the mirrors L is the length of the cavity along the optical axis. From the equation for the Gouy phase, since $\arctan(z) \leq \pi/2$ one can see that the transverse modes are always more closely spaced together than the longitudinal modes, and are exactly half the spacing when the cavity is confocal, i.e. $R_1 = R_2 = d$.

There are several reasons why we would like to concentrate laser power into the TEM_{00} mode.

1.) Highly reflective mirrors result in narrow cavity resonance widths as seen in Equation (11). The higher order modes are at a different frequency than the TEM_{00} mode and when the cavity is exciting this mode, if these higher order mode frequencies do not match the TEM_{00} cavity resonance mode, then they are not amplified by the cavity and are wasted.

2.) To accurately determine gas concentration, the absorption coefficient α should be well-determined. If several frequencies caused by different modes are being measured simultaneously with the TEM_{00}, this can lead to absorption at the wings of the absorption line at a different α value, increasing the error in the determination of $\alpha(\nu_{TEM00})$.

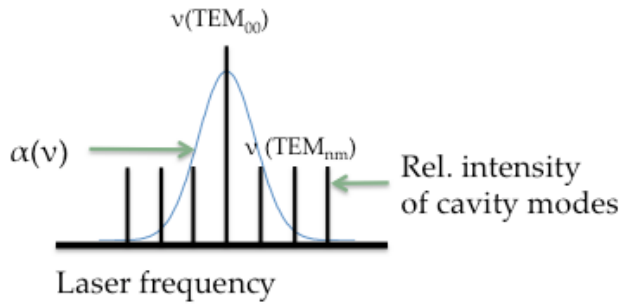

Figure 9: Schematic of cavity modes superimposed on absorption line

3.) Due to nodes of intensity, higher order modes have more intensity away from the center of the mirror, compared to the TEM_{00} mode. This causes the reflectivity R, and thus the cavity ringdown rate k, to be more vulnerable to mirror surface/coating inhomogeneity.

Mode matching

To concentrate light intensity into the TEM_{00} mode, we use a technique called mode matching.

Even if the beam enters the cavity as a pure TEM_{00} Gaussian, the beam may not have the same radius of curvature and same size that would resonate with the cavity. The resonant TEM_{00} mode for a given wavelength of a cavity can be defined by its complex beam parameter q_{cavity} at a given point, e.g., the entrance of the cavity:

$$q(z_{cav}) = \left(\frac{1}{R(z_{cav})} - i \frac{\lambda_0}{\pi w(z_{cav})^2} \right) \tag{37}$$

The problem of mode matching becomes that of changing the complex beam parameter of the beam from the laser head, $q_{laserhead}(z = 0)$, through the use of lenses/mirrors, to match q_{cavity} when it gets to the entrance of the cavity. Given two thin lenses of focal length f_1 and f_2 respectively, placed at z_1 and $z_2 = z_1 + d$, where d is the separation between the two lenses, the complex beam parameter $q_{laserhead}$ becomes, as in Equation 32:

$$= \begin{pmatrix} 1 - f_2 \cdot z_3 - f_1(z_3 + d(1 - f_2 \cdot z_3)) & z_3 + d(1 - f_2 \cdot z_3) + z_1(1 - f_2 \cdot z_3 - f_1(z_3 + d(1 - f_2 \cdot z_3)) \\ -f_2 - f_1(1 - d \cdot f_2) & 1 - d \cdot f_2 + (-f_2 - f_1(1 - d \cdot f_2))z_1 \end{pmatrix}$$

By equating this q_{out} with q_{cavity}, the equation can be solved for the required positions of the two lenses, i.e. z_1 and $z_1 + d$. Due to practical considerations, different focal lengths may be chosen to produce a solution that would allow easy placement of the two lenses.

Spectroscopy of Nitric Oxide

Introduction to spectroscopy

In the presence of light in resonance between two energy levels E_u and E_l of a molecule, the rate at which absorption of the radiation occurs is proportional to the density of radiation ρ(v) and the number of molecules in the lower state l:

$$\frac{dN_l}{dt} = -g(E_l)B_{u\leftarrow l}\rho(\nu)N_l \tag{38}$$

Where $B_{u\leftarrow l}$ is known as the Einstein B coefficient, and $g(E_l)$ is the degeneracy of the lower state. This equation assumes that there are a negligible number of molecules in the upper state. When there are a significant number of molecules in the upper state then we must consider emission of radiation from the upper state when looking at the change in population of the lower level. This occurs when the spacing between energy levels $\Delta E = E_u - E_l$ is small, because the probability of a system (e.g. a molecule) being in a given state is proportional to the "Boltzmann factor":

$$P(E) = g(E)e^{-\frac{E}{kT}} \tag{39}$$

where g(E) is the degeneracy of the given energy level. Thus the relative number of molecules in the upper state vs. the lower state is given by:

$$\frac{N_u}{N_l} = \frac{g(E_u)e^{-\frac{Eu}{kT}}}{g(E_l)e^{-\frac{El}{kT}}} = \frac{g(E_u)}{g(E_l)}\exp\left(-\frac{E_u - E_l}{kT}\right) \tag{40}$$

For mid-infrared transitions of nitric oxide, the population of the upper state relative to the lower state is:

$$e^{-\frac{\Delta E}{kT}} = e^{-\frac{hc}{kT}\tilde{\nu}} \\ = \exp(-4.87\times10^{-3}\,\mathrm{cm}\times1900\,\mathrm{cm}^{-1}) \approx 10^{-4} \tag{41}$$

where we used:

$$\frac{hc}{kT} = 4.87\times10^{-3}\,\mathrm{cm} \\ \tilde{\nu} \equiv \frac{\nu}{c} = \frac{1}{\lambda}\ \text{“wavenumber”} \tag{42}$$

Thus the upper state population is negligible. Significant numbers in the upper state can be induced however when a laser has pumped a large proportion of the molecules in the lower state into the upper state. This occurs when the laser intensity is comparable to that described in Equations (79) and (80).

The rate at which stimulated emission of radiation occurs is proportional to the density of radiation and the number of molecules in the upper state u, and the rate constant B for the stimulated emission is the same as for the lower state multiplied by the relative degeneracy of the upper vs. the lower energy level , i.e.:

$$\frac{B_{u\leftarrow l}}{B_{l\leftarrow u}} = \frac{g(E_u)}{g(E_l)} \tag{43}$$

Thus a more general change in population would be:

$$\frac{dN_l}{dt} = -g(E_l)B_{u\leftarrow l}\rho(\nu)N_l + g(E_u)B_{l\leftarrow u}\rho(\nu)N_u \tag{44}$$

The density of radiation actually stimulates emission from the upper state to the lower state.

The B coefficient is proportional to the dipole moment of the molecule $B_{u\leftarrow l}=\frac{2\pi|\mu_{ul}|^2}{3\hbar}$. Nitric oxide's electric dipole moment is 0.153 D [9]. It can be proved [10] that the change in population of the lower state, and thus the absorption and emission rate of light, will oscillate at a rate proportional to the amplitude of the light's electric field, the Rabi frequency. The light emitted and absorbed by each molecule will be in phase, in the same direction, and constructively interfere. However in general, there are two processes that prevent this, and lead to a decrease in the light signal after passing through a sample of molecules. In addition to stimulated absorption/emission, molecules may spontaneously emit and relax to the lower state, and this rate A_{ul} is independent of radiation density and in random directions. Thus a more complete rate equation would be:

$$\frac{dN_l}{dt}=-g(E_l)B_{u\leftarrow l}\rho(\nu)N_l+g(E_u)B_{l\leftarrow u}\rho(\nu)N_u+g(E_u)A_{ul}N_u \tag{45}$$

Thus even in absence of radiation, the upper state population will decrease exponentially:

$$\frac{N_u(t)}{N_u(0)}=e^{-A_{ul}t} \tag{46}$$

From the Planck frequency distribution of photons, A can be calculated in terms of B, and thus μ_{ul}:

$$A_{ul}=\frac{8\pi h\nu_{ul}^3}{c^3}B_{l\leftarrow u};\ B_{l\leftarrow u}=\frac{2\pi|\mu_{ul}|^2}{3\hbar} \tag{47}$$

Also, collisions between molecules may induce molecules in the upper state to drop to the lower state without emitting a photon (a T_1 process) or destroy the phase relationship between population of the upper state and the population in the lower state (a T_2 process). This also prevents the wave functions of the individual molecules from constructively interfering. The collision rate of molecules is proportional to the pressure of the gas[11]. From the uncertainty principle, the finite life-time of the upper state leads to a spread in its energy level, where $\Delta E\, \Delta t \geq \hbar$.

The effect of this spread is that light does not need to be exactly in resonance with the energy difference between the two states to pump molecules up to the upper state. A range of frequencies, called the homogeneous linewidth of the transition, will excite the molecules. By taking a Fourier transform of the exponential decay of the populations, it can be seen that the absorption cross-section as a function of light frequency assumes a Lorentzian distribution:

$$g_L(\nu) = \frac{\frac{\Delta\nu_L}{2\pi}}{(\nu-\nu_{ul})^2+(\frac{\Delta\nu_L}{2})^2} \tag{48}$$

where $\Delta\nu_L = \frac{A_{ul}}{2c} + bP$ is the full width half maximum of the Lorentzian, with b being the pressure broadening coefficient relating increased pressure to an increased width of the absorption peak. This is known as “homogeneous broadening” because every molecule in a gas has an equal probability of being excited by light at a given frequency. b is on the order of 2.5 MHz/Torr[12] for the mid-IR transitions we are studying, and with the pressures of gas our experiments work in (from 0.1 Torr to 100 Torr), the pressure broadened width is ≥ 250 kHz.

For relatively low light frequencies such as in the mid-IR, the spontaneous decay rate is negligible. In the case of nitric oxide, the 1/e decay time of the upper states due to spontaneous emission is on the order of 0.02 s, equivalent to a homogeneous broadening of 6 Hz.[13] Thus the dominant contribution to homogeneous broadening in our experiment is due to collisions.

However, molecules in a gas have a range of velocities, and the distribution of molecular velocities as a function of frequency depends on the temperature T, known as the Maxwell-Boltzmann distribution:

$$P(\nu) = \exp\left(-\frac{E_{kin}}{kT}\right) = \exp\left(-\frac{mv^2}{2kT}\right) \tag{49}$$

This velocity causes a Doppler shift in the frequency of light seen by a given molecule. A molecule at velocity v will only be excited by the light if it has frequency:

$$\nu = \nu_{ul}\left(1+\frac{v}{c}\right) \tag{50}$$

Where ν_{ul} represents the resonant frequency if the molecule were at rest. Solving for v:

$$v = \frac{c}{\nu_{ul}}(\nu - \nu_{ul}) \tag{51}$$

Thus the distribution of molecules as a function of frequency to excite becomes, after normalization:

$$g_D(\nu) = \sqrt{\frac{mc^2}{2\pi kT\nu_{ul}^2}}\exp\left(-\frac{mc^2(\nu-\nu_{ul})}{2kT\nu_{ul}^2}\right) \tag{52}$$

This is a Gaussian or normal distribution of FWHM:

$$\Delta\nu = 2\nu_{ul}\sqrt{\frac{2kT\ln 2}{mc^2}} \tag{53}$$

Thus the absorption cross-section takes the form of a Gaussian. Given nitric oxide's molecular mass of 30.01 amu and a temperature of approximately 296 K, the Doppler width we see is $\Delta\nu_D \approx 128$ MHz. Doppler broadening is a type of "inhomogeneous broadening" because which molecules are affected by the broadening depends on the individual molecule's velocity.

A simple model for combining the effects of homogeneous broadening and Doppler broadening is by considering that the molecules at every given velocity class have a range of frequencies of width $\Delta\nu_L$ around $\nu = \nu_{ul}(1 + v/c)$. Thus a convolution of a Gaussian with a Lorentzian is gives an approximate line shape for absorption, known as the Voigt profile:

$$g_V(\nu, \Delta\nu_D, \Delta\nu_L) = \int_{-\infty}^{+\infty} g_D(\nu', \Delta\nu_D) g_L(\nu - \nu', \Delta\nu_L) d\nu' \tag{54}$$

Ro-vibrational spectroscopy

Nitric oxide is a diatomic molecule of mass 30.01 amu. It has an electric dipole moment of 0.166 D and a ground electronic state of $X^2\Pi$. Due to symmetry, diatomic molecules do not have a well-defined total orbital angular momentum L; only the projection of L along the internuclear axis, or Λ, is well-defined. In the ground state above, Λ = 1, also known as a Π state. It has one unpaired electron and that leads to two possible projections of S = 1/2 onto the internuclear axis (Σ): Σ = -1/2 and Σ = 1/2. The projection of the total electronic angular momentum is denoted Ω = Λ + Σ, and has thus two possible values: Ω = 1/2 where the projection of S (i.e. Σ) is

opposite that of Λ, and Ω = 3/2 where Σ is in the same direction as Λ. This splits the electronic ground state $^2\Pi$ into two levels separated by A ≈ 124 cm^{-1}: $^2\Pi_{3/2}$ and $^2\Pi_{1/2}$. The splitting is due to a spin-orbit interaction:

$$\Delta E_{s-o} = A\Lambda\Sigma \tag{55}$$

In addition to this splitting, there is a small splitting caused by a coupling between the rotation of the two nuclei: N, and Λ (whether it points toward the nitrogen atom or toward the oxygen atom). This splitting into “e” and “f” states is small, and the difference in energy for the equivalent state at the higher v and J values even smaller, in fact for the Ω = 3/2 states it is less than half the FWHM of the Doppler broadening at room temperature. This leads to unresolved doublets in the absorption spectrum.

We are studying ro-vibrational transitions of NO from the fundamental vibrational mode to the first excited vibrational mode, and a change in total angular momentum ΔJ of ± 1. The simplest model for vibration is that of a harmonic oscillator, where the energy levels are given by:

$$E_v = \hbar\omega_e\left(v+\frac{1}{2}\right) \tag{56}$$

Where ω_e is given by:

$$\omega_e = \frac{1}{2\pi}\sqrt{\frac{k}{\mu}} \tag{57}$$

Here, k is the effective spring constant of the system, and μ here is the reduced mass of the system, given by:

$$\mu_{^{14}NO} = \frac{m_{^{14}N}m_O}{m_{^{14}N}+m_O} = \frac{14.00\ \text{amu}\times 15.99\ \text{amu}}{14.00\ \text{amu}+15.99\ \text{amu}} = 7.464\ \text{amu} \tag{58}$$

To correct for deviation of a molecule from harmonic behavior, an anharmonic correction term is added:

$$E_v = \hbar\omega_e(v+\frac{1}{2}) + \omega_e x_e(v+\frac{1}{2})^2 \quad (59)$$

where $x_e = \frac{\hbar\omega_e}{4D_e}$ (60)

and where D_e is the dissociation energy, the energy required to dissociate the nitrogen atom from the oxygen atom at a given electron configuration, in our case, $X^2\Pi$.

We now consider the rotational energy of the molecule. The first approximation we use is that the bond length between the nitrogen and oxygen atoms is fixed. This is the "rigid rotor" approximation. Rotating molecules then have a rotational kinetic energy:

$$E_{rot} = \frac{\hbar^2}{2I}J(J+1) \quad (61)$$

Here I is the moment of inertia, given by $I = \mu R_e^2$, where R_e is the equilibrium distance between the nitrogen and oxygen atoms. We can re-write E_{rot} as:

$$E_{rot} = \frac{h}{8\pi^2\mu R_e^2}hJ(J+1) = B_e hJ(J+1) \quad (62)$$

We have to consider that the average separation between the nitrogen and oxygen atoms at higher vibrational levels is larger, which leads to a larger moment of inertia, which reduces the energy of the rotational terms. Therefore another correction we add is:

$$E_{rot} = B_e hJ(J+1) - \alpha_e(v+\frac{1}{2})J(J+1) \quad (63)$$

With the negative sign showing that the rotational energy is reduced from what is expected, at higher vibrational levels v. We can simplify this expression if we introduce a v-dependent B_e:

$$B_v = B_e - \alpha_e(v+\frac{1}{2}) \tag{64}$$

such that:

$$E_{rot} = B_v h J(J+1) \tag{65}$$

We can thus combine the vibrational and rotational energies into one expression:

$$\frac{E_{J,v}}{h} = \omega_e(v+\frac{1}{2}) - \omega_e x_e(v+\frac{1}{2})^2 + B_v J(J+1) \tag{66}$$

Or in terms of "wavenumber" units (in cm^{-1}),

$$\tilde{\nu} = \frac{E_{J,v}}{hc} = \widetilde{\omega_e}(v+\frac{1}{2}) - \widetilde{\omega_e} x_e(v+\frac{1}{2})^2 + \widetilde{B_v} J(J+1) \tag{67}$$

where $\widetilde{\omega_e} = \frac{\omega_e}{c}; \widetilde{B_v} = \frac{B_v}{c}$ (68)

In our setup, the transitions that we are looking at are only between v = 0 and v = 1. We can think of the transition frequency as having a vibrational contribution and a rotational one.

The vibrational part is:

$$\widetilde{v_0} = \frac{\Delta E_{v',v''}}{hc} = \widetilde{\omega_e}(v'-v'') - \widetilde{\omega_e} x_e[(v'+\frac{1}{2})^2 - (v''+\frac{1}{2})^2] \tag{69}$$

For our experiment, v' = 1 and v'' = 0, thus

$$\widetilde{v_0} = \widetilde{\omega_e} - 2\widetilde{\omega_e} x_e \tag{70}$$

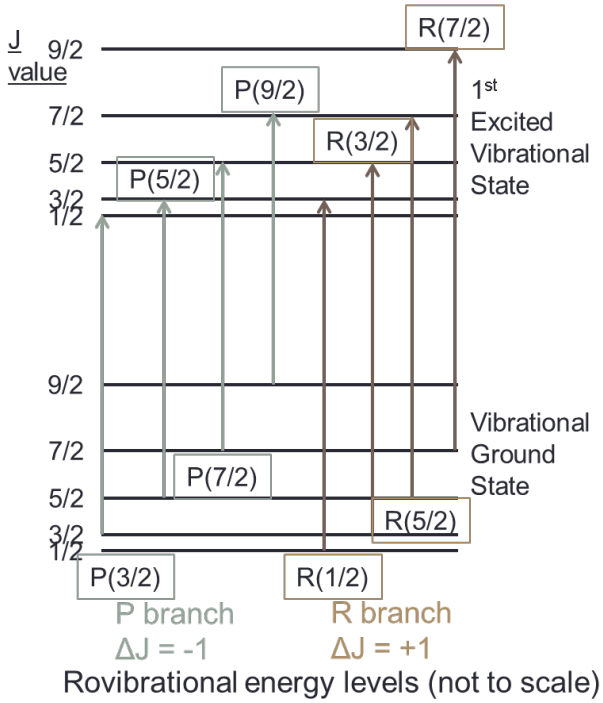

Figure 10: P- and R- type rovibrational transitions from the fundamental to the first excited vibrational state

To add the rotational contribution, we have to consider three cases:

1.) one where J → J - 1 upon going to the excited vibrational state, known as a P-branch transition

2.) one where J → J , known as a Q-branch transition

3.) one where J → J + 1, known as an R-branch transition.

For P-branch transitions:

$$\widetilde{\nu_P}(J) = \widetilde{\nu_0} + B_{v'=1}(J-1)J - B_{v''=0}J(J+1)$$
$$= \widetilde{\nu_0} - J(B_{v'=1} + B_{v''=0}) + J^2(B_{v'=1} - B_{v''=0}) \quad (71)$$

One can expect to see a spectrum of lines that starts out roughly evenly spaced apart and getting lower in frequency as J is increased. Since ($B_{v'=1} - B_{v''=0}$) < 0, the lines will spread out at higher J.

For R-branch transitions,

$$\widetilde{\nu_R}(J) = \widetilde{\nu_0} + B_{v'=1}(J+2)(J+1) - B_{v''=0}J(J+1) \\ = \widetilde{\nu_0} + (J+1)(B_{v'=1} + B_{v''=0}) + (J+1)^2(B_{v'=1} - B_{v''=0}) \quad (72)$$

One can expect to see a spectrum of lines that starts out roughly evenly spaced apart and getting higher in frequency as J is increased. However, due to the negative ($B_{v'=1} - B_{v''=0}$) factor, the lines will get closer together at higher J.

For Q-branch lines,

$$\widetilde{\nu_Q}(J) = \widetilde{\nu_0} + B_{v'=1}J(J+1) - B_{v''=0}J(J+1) \\ = \widetilde{\nu_0} + J(J+1)(B_{v'=1} - B_{v''=0}) \quad (73)$$

Due to the lack of a summed B term ($B_{v'=1} + B_{v''=0}$), the Q-branch lines are spaced very close together, especially at low J. Due to the negative ($B_{v'=1} - B_{v''=0}$) factor, as J increases, the transition frequency decreases, at a roughly quadratic rate.

At low laser intensities, the intensity of the transitions depends mostly on the population of the lower state (i.e. v = 0), since the population of the upper states (v = 1) is < 10^{-4} that of the lower states. Each energy state $E_{J,v=0}$ has a multiplicity of 2J+1, because of the possible projections of J onto the internuclear axis, from –J, -J +1, … J-1, J. Thus the population of each lower state is proportional to the probability:

$$P(E_{J,v=0}) = g(E_{J,v=0})e^{-\frac{E_{J,v=0}}{kT}} = (2J+1)\exp\left(-hc\frac{\tilde{\omega}_e \times \left(\frac{1}{2}\right) - \tilde{\omega}_e x_e \left(\frac{1}{2}\right)^2 + \tilde{B}_{v=0}J(J+1)}{kT}\right)$$
$$= (2J+1)\exp\left(-hc\frac{\tilde{B}_{v=0}J(J+1)}{kT}\right)\exp\left(-hc\frac{\frac{\tilde{\omega}_e}{2} - \frac{\tilde{\omega}_e x_e}{4}}{kT}\right) \quad (74)$$

Because (2J + 1) increases while $\exp\left(-hc\frac{\widetilde{B}_{v=0}J(J+1)}{kT}\right)$ decreases with increasing J, there is a J at which the intensity of the transition is the strongest. This happens at $J \simeq \frac{11}{2}$ for both the P- and R- branch lines.

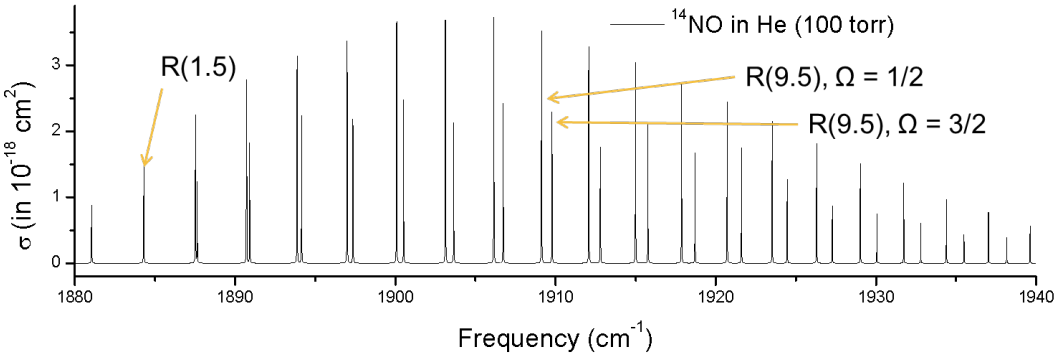

Figure 11: R-branch transitions for ^{14}NO within range of our mid-IR QCL

The appendix contains data for the transitions we used consistently for detection..

Saturated absorption

When a laser excites molecules to a mostly empty level, the amount of absorption follows the Beer-Lambert law:

$$I_{out} = I_0 \exp\left(-\frac{\sigma N_0 L}{V}\right) \quad (75)$$

Where N_0 is the number of molecules in the ground state and σ the absorption cross-section. However, in the case of either intense laser radiation or an excited energy level that isn't far from the ground state, for example, with microwave-induced purely rotational transitions, there will be significant numbers of molecules in the upper state, $N_l = N - N_u$.

This leads to what is known as saturated absorption, where an increase in light intensity reaching the sample will not lead to a proportional increase in the transmitted light intensity. If one plots an absorption spectrum, the peak will actually get wider and shallower at high light intensities, an effect known as power broadening. The Doppler-broadened inhomogeneous lineshape will have its width broadened:

$$\Delta\nu_{D'} = \Delta\nu_D\sqrt{1+\frac{I_\nu}{I_S}} \tag{76}$$

and its absorbance will be reduced to:

$$\alpha(\nu) = \frac{\alpha_0(\nu)}{\sqrt{1+\frac{I_\nu}{I_S}}} \tag{77}$$

where α_0 represents the unsaturated absorbance, and where I_v is the intensity of the laser:

$$I_\nu = \frac{P}{\frac{1}{2}\pi w_0^2} \tag{78}$$

The saturation intensity I_S is found to be:

$$I_S = \frac{2\pi^2 h\nu\Delta\nu_L}{(\tau/t_{spont})\lambda^2} \tag{79}$$

(Yariv, 8.7-16)[8] , where τ represents the lifetime of the upper state, here assumed to be equal to the T_2 collisional dephasing time, and t_{spont} the spontaneous lifetime of the upper state. These two quantities are the inverses of the homogeneous line width and A_{ul} respectively. We can thus write:

$$I_S = \frac{2\pi^3 hc\Delta\nu_L^2}{A\lambda^3} \tag{80}$$

The saturation parameter can be defined as the ratio between the laser intensity I_ν and the saturation intensity I_S, a quantity that increases for shorter excited state lifetimes (and thus wider homogeneous width), and increases at higher frequencies / smaller wavelengths. Saturation can also affect the homogeneous sub-Doppler profile. In our case, since the homogeneous width is comparable to the linewidth of our laser, it is useful to define a frequency-dependent I_S :

$$I_S = \frac{4\pi^2 hc\Delta\nu_L}{A\lambda^3 g_L(\nu)} \tag{81}$$

[8]

where $g_L(\nu)$ is the normalized Lorentzian line shape as defined in Equation 48. Away from the center, I_S is larger, requiring a larger laser intensity to saturate. At the center of the homogeneous profile, the absorbance is reduced by a factor of $1+\frac{I_\nu}{I_S}$.

A very dramatic example of homogeneous saturated absorption is the observation of Lamb dips.

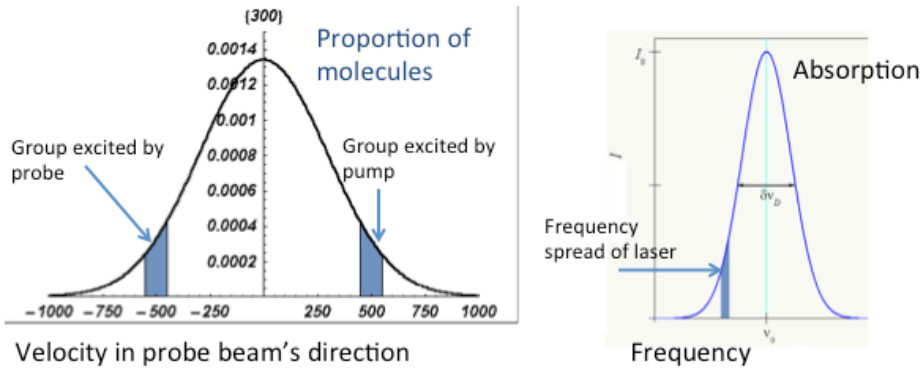

Figure 12: The two velocity classes excited by counterpropagating beams (pump + probe) when the laser frequency is below resonance but within the Doppler width.

Normally, the Doppler broadening prevents the direct measurement of the homogenous line width. However, if there are two overlapping beams at the same frequency but counterpropagating, a sub-Doppler dip with the homogeneous width can be seen at the center of the Doppler-broadening line.

When the laser's frequency is below the resonant frequency of the transition, one beam excites molecules heading toward it that have a velocity in the z-direction of $v_z = +v$, and the other beam excites molecules going in the opposite direction at velocity $v_z = -v$. As the laser's frequency is swept to the center of the resonant transition, the two beams now excite the same group of molecules: those with $v_z = 0$. If the laser power is close to the saturation power, then the doubling of laser power will lead to suppression in the absorption due to saturation.

The Cavity Ring-down Apparatus

General schematic

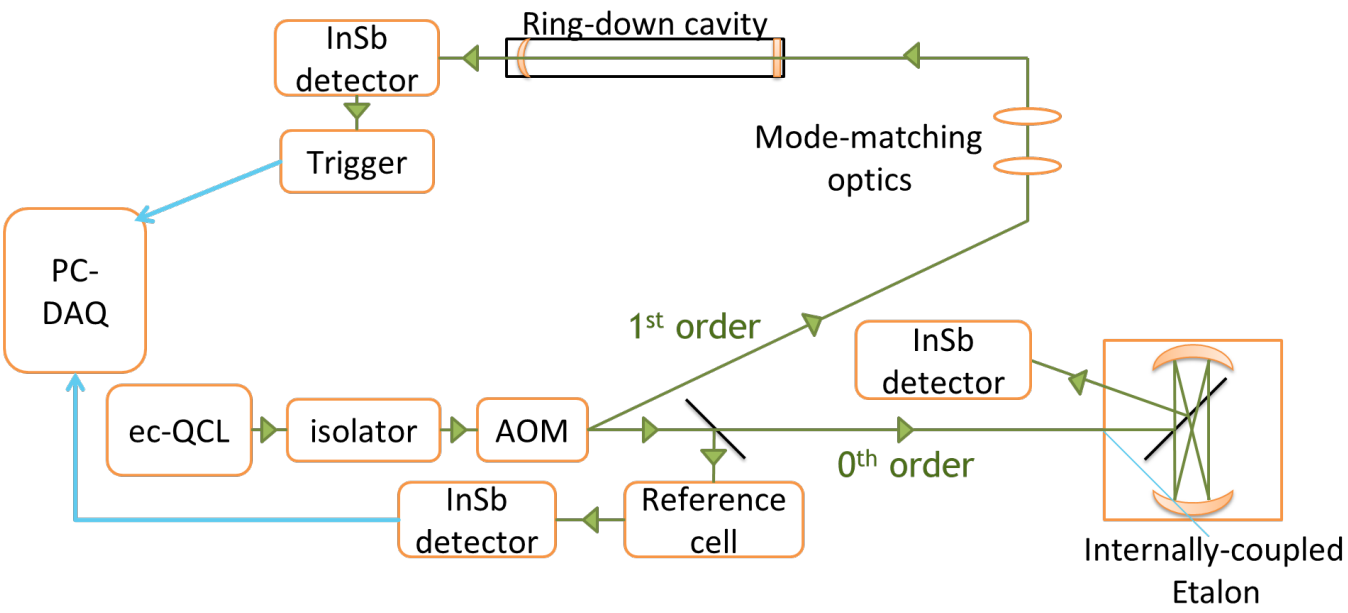

Figure 13: Scheme of Cavity Ring-down apparatus

The cavity ring-down setup uses an external cavity quantum cascade laser (ec-QCL) manufactured by Daylight Solutions, which is tuned to be resonant with either a P-type (ΔJ = -1) or R-type (ΔJ = +1) vibrational fundamental transition from the ground vibrational state. By using a reference cell filled with nitric oxide, we can determine whether we are on resonance. The laser passes through an optical isolator (Innovation Photonics), which serves to reduce laser light feedback from optical components as well as the cavity itself. After the isolator, the laser passes through the acousto-optic modulator (AOM). The 0^{th} order diffraction is sent to the internally coupled Fabry-Pérot interferometer (ic-FPI) to measure the drift and jitter of the laser. The 1^{st} order diffracted beam from the AOM passes through mode matching optics

before it is sent into the cavity and from there, to a 90° off-axis parabolic mirror which focuses the light into a 0.5 mm^2 InSb detector (Kolmar Technologies, KISDP-0.5-FJ/GE).

The cavity itself has a set of three PZTs (Thorlabs AE0505D08F) which adjust the length of the cavity and thus which laser frequencies are resonant with it. The PZTs are scanned a little over 1 FSR at a rate of 20 to 40 Hz, ensuring that the laser will be in resonance with the cavity at least twice during each PZT cycle, and slow enough to avoid the vibrations occurring at > 80 Hz. The high speed InSb detector has an internal pre-amp of transimpedance gain 1×10^4 V/A, which generates a voltage proportional to the light intensity. The detector and pre-amp are capable of capturing intensity changes up to a bandwidth of 20 MHz. The voltage from the pre-amp is connected to the trigger input of a pulse generator (DG535, Stanford Research Systems). When the cavity is in resonance, the light intensity builds over several microseconds. When the voltage reaches a preset threshold level, the DG535 is programmed to output a pulse that turns off the AOM for ≈ 40 μs, or approximately ten times the typical empty-cavity decay time of τ = 4 μs. This extinguishes the 1^{st} order beam to the cavity, and allows the light level in the cavity to begin decaying. The decay in voltage is recorded with a computer program and fitted to an exponential model, yielding a measurement of the absorption due to NO after the empty cavity decay rate is subtracted.

Review of Optical Components

Laser

The laser is a 41052-MHF continuous wave external cavity quantum cascade laser, manufactured by Daylight Solutions. This type of quantum cascade laser has a cavity that goes

from the quantum cascade lasing medium to a grating mounted on a translation stage. It has coarse tuning (≈ 0.01 cm^{-1} resolution) by way of a stepping motor that adjusts the angle of the grating, which allows adjustment of the output wavelength from 5.05 µm to 5.45 µm (1980 cm^{-1} to 1835 cm^{-1}). Finer tuning ($\Delta\nu < 1$ cm^{-1}) of the external cavity length is achieved through a PZT which can be modulated by a voltage up to 100 Hz. A voltage of 100 V applied to the laser's PZT shifts the laser's output frequency by ≈ 1 cm^{-1}. A more detailed measurement of the precise voltage – to frequency shift relationship is detailed in the next sections. The laser's wavelength and intensity can also be modulated by changing the QCL current. The laser frequency can be modulated at a rate of up to 1 MHz, with a modulation depth per voltage dependent on the modulation frequency:

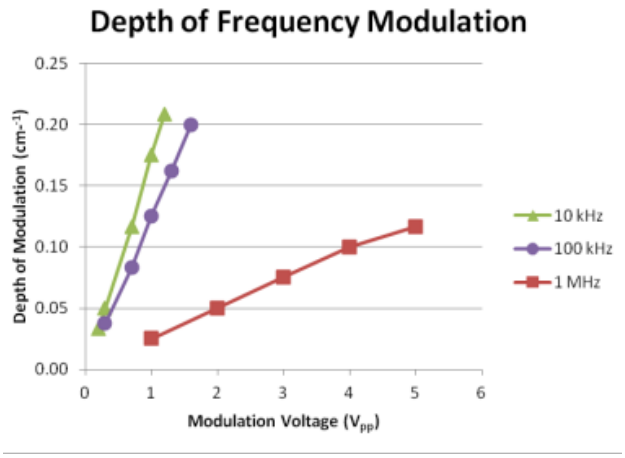

Figure 14: Depth of modulation as a function of voltage applied to QCL bias tee, at various modulation frequencies.

We primarily modulated the QCL current to dither the laser frequency around a cavity mode with a modulation frequency of < 100 Hz and a depth of ≈ 20 MHz, or several times the line width of the laser. At such modulation frequencies, we get ≈ 0.17 cm^{-1} of modulation depth per

volt applied to the current input. This was done while the cavity's mode was scanned over the absorption line using its own set of PZTs (see following section on cavity PZTs). The new laser model replaced the 21052-MHF ec-QCL used for measurements from before 2013. Comparing the two models:

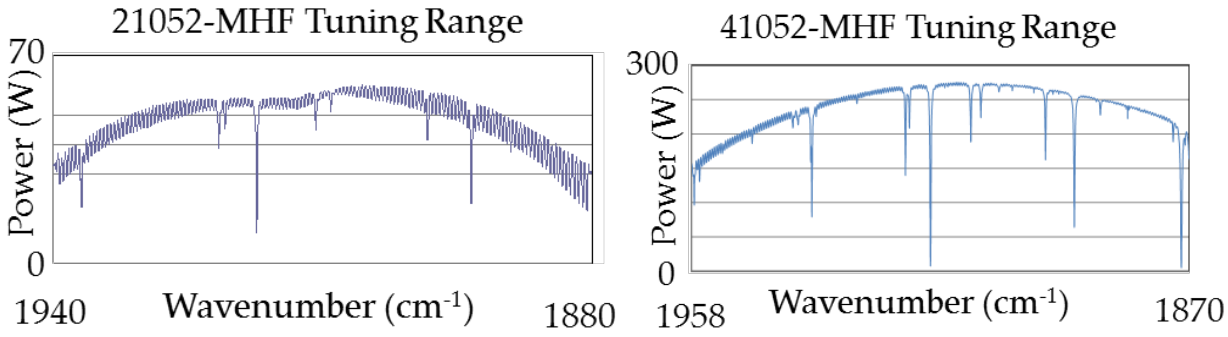

Figure 15: Mode-hop free tuning range of the two lasers: 21052-MHF on the left, 41052-MHF on the right

The advantages of the 41052-MHF model include: larger range of tunability, allowing access to P-branch NO14 lines and R branch NO15 lines, the ability to modulate the laser's QCL current down to a frequency of 0 Hz (DC), and a far greater laser power (see vertical scale on Figure 15), allowing for higher saturation parameters of an NO sample. In addition, if the laser power reaching the ring-down cavity is kept fixed to the level attained with the previous laser by attenuating the RF power to the AOM, then the relative power of the feedback from the cavity in relation to the power in the laser head will decrease. The RF to the AOM was attenuated by 8 dB during measurements of the biological NO samples.

Acousto-optic modulator (AOM)

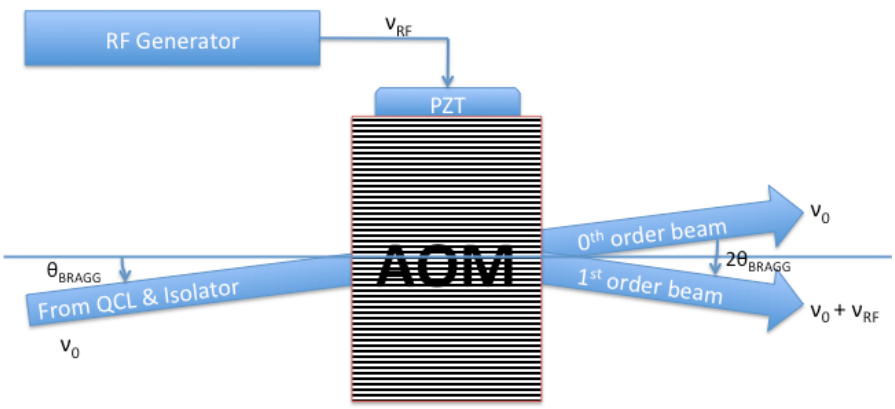

Figure 16: Diagram of operation of an AOM

An acousto-optic modulator uses an RF signal (in our case, 40 MHz) which acts on a PZT to generate spatial modulations of the index of refraction of an optical material through the use of a traveling acoustic wave. The spatial modulations turn the optical material into a diffraction grating, with the first order beam deflecting at the Bragg angle.

In our experiment, light to the cavity is extinguished by turning off the RF generated-diffraction grating. The time it takes to turn off the AOM is the latency time between when the laser voltage reaches threshold and the time the pulse extinguishes the RF signal, plus the time it takes for the electrical signal to reach the PZT, plus the time it takes for the generated acoustic signal to travel from the PZT end of the optical material to the location of the beam. This was measured to be 2.6 µs. In addition, the shut off time for the beam is given by the time it takes for the termination of the acoustic signal to propagate across the beam profile. Since this is an acoustic effect, this time is given by:

$$\Delta t_{off} = \frac{2w_{beam}}{v_{acoustic}} \tag{82}$$

Having a small beam diameter at the AOM leads to a faster shutoff time.

Our AOM is a Gooch & Housego R37040-3-5.4, whose optical element is composed of Ge with antireflective coatings on the input and output windows, and a Bragg angle of 39.2 mrad at an RF frequency of 40 MHz. The RF signal is generated by a Gooch & Housego NeOS N64025-45-3ASDFS oscillator that produces a 2 W 40 MHz signal that can deflect up to 70% of the laser beam power into the 1st order. The measured 90% to 10% extinction time based on measuring the direct light intensity with a fast InSb detector is ≈ 150 ns.

Optical isolator

Feedback of laser light from optical elements and the cavity back into the laser head turned out to be destabilizing the laser's frequency. To reduce the amount of retroreflected light, we used an optical isolator, which is composed of two polarizers and a Faraday rotator.

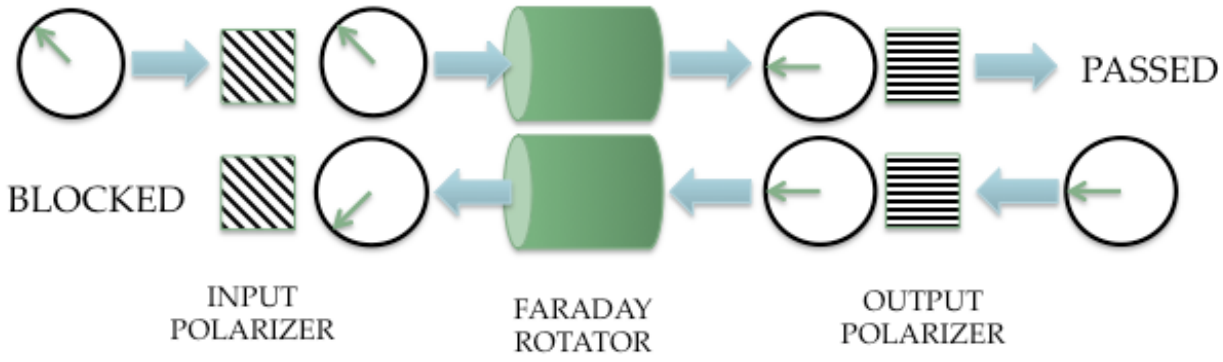

Figure 17: The effect of an isolator composed of an input polarizer, Faraday rotator, and an output polarizer. The top sequence is the laser propagating from the laser head to the cavity; the bottom sequence is the laser feedback from the cavity back to the laser head.

A Faraday rotator works because there is a birefringence (difference in index of refraction) between light that is left handed circularly polarized relative to the Faraday rotator's magnetic field, and light that is right handed circularly polarized relative to the same field. The light from the laser and entrance polarizer is vertically linearly polarized, which can be decomposed into equal left handed and right handed polarized light. The length of the Faraday rotator is chosen so that the effect of the birefringence on the relative phases of the left handed vs. right-handed light is a 45° counterclockwise rotation in the linear polarization of the beam when it exits the Faraday rotator. This diagonally polarized light then leaves through the exit polarizer set up to match this diagonal polarization. Light coming back from optical elements will be diagonally polarized and pass through the exit polarizer. However when it enters the Faraday rotator, which helicity of polarization experiences a higher index of refraction is switched because the direction of propagation is reversed while the magnetic field direction hasn't. This leads to a rotation of the polarization 45° in the opposite direction, leading to horizontally polarized light, which is blocked by the vertically polarized entrance polarizer.

The optical isolator is manufactured by Innovation Photonics. The Faraday rotator is composed of a patented material that works at our wavelength. The polarizers consist of Ge wedges placed at Brewster's angle. Due to the high index of refraction of Ge (≈ 4), the wedges are at a high angle and therefore negligible light of p-polarization is lost due to Fresnel reflection.

Internally coupled Fabry-Pérot interferometer (ic-FPI)

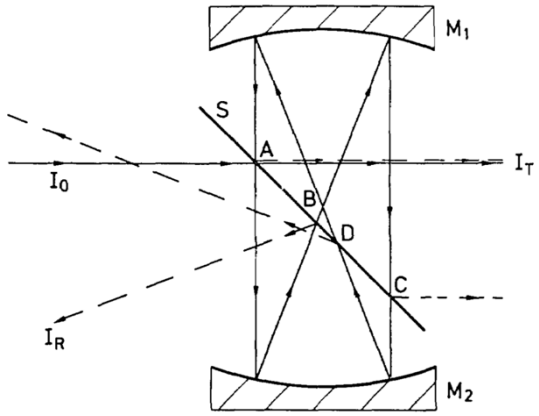

Figure 18: Schematic of an ic-FPI[14] with the input beam I_0, output beam I_R, and transmitted beam (not used) I_T

A Fabry-Pérot interferometer is an optical cavity used to measure the linewidth and frequency jitter of a laser. At frequencies separated by the free spectral range of the etalon, a peak in transmission occurs, whose width is inversely proportional to the finesse of the etalon. In a conventional etalon, light travels through the etalon along a single axis to the detector. However, in order to minimize reflections of laser light from the etalon back to the laser head, a modified setup devised by Reich et al.[14] was used. Light enters the cavity through a beamsplitter and exits at a slightly different angle. In this case, the FSR is c/4L instead of c/2L as in Equation 10 because it takes two round trips for the light to return to its starting position.

Attached to one of the two etalon mirrors are a set of PZTs which adjust the length of the cavity. A shift in cavity length leads to a change in the free spectral range of the etalon, and therefore its resonant frequencies. Given a cavity length of L, and a wavelength of light of ≈ 5.2 μm, a shift in the cavity length of ΔL causes the resonant frequency of light to change by

$\Delta\nu = -\frac{c\,\Delta L}{\lambda\ L}$. By applying a periodic voltage ramp to the PZT that corresponds to ≈ 1 FSR, and noting at which voltage the laser light at the detector peaks in resonance, the laser's drift in frequency can be measured. Our setup uses a circuit box that samples and holds the voltage at which light intensity peaks at the detector, after every ramp period.

Reference cell

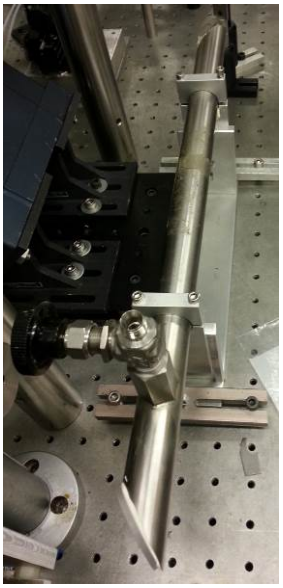

Figure 19: Image of ^{14}NO reference cell. There is a separate cell filled with ^{15}NO

A part of the beam to the cavity is diverted with a beamsplitter through a reference cell of known NO concentration and then a detector. The input and output windows of the reference cell are at Brewster's angle for the horizontally-polarized light to minimize Fresnel losses. Whereas the etalon allows one to measure the drift of the laser's frequency relative to the etalon, the reference cell allows for absolute frequency measurement around NO absorption lines. The position of the center of mid-IR NO ro-vibrational absorption lines as well as their self- (NO) pressure broadening coefficients are known from the HITRAN 2004 database[13]. By

measuring the ref cell and cavity ring-down simultaneously during a scan of the laser frequency, the absorption line can be located even when the concentration of NO in the cavity is lower than the limit of detection. Using an electronic feedback system to be described below, the laser frequency may be locked to the side of an absorption line, or if the laser frequency is modulated, the laser frequency can be locked to the top of the absorption line.

Characterization of System

Laser PZT

The ec-QCL laser's fine frequency adjustment is through a PZT. Applying a voltage to the PZT contracts the length of the laser's external cavity. There is an approximate linear relationship between the PZT voltage and laser frequency, of approximately 1 V = 0.01 cm^{-1} (≈ 300 MHz). One method we used to measure non-linearity was by measuring the distance between the two peaks of the resolved R (13/2), Ω = 1/2 doublet in terms of PZT voltage. From the HITRAN database, it is known that the peaks are 0.0110(3) cm^{-1} apart. Scans were performed at different PZT voltages, where 200 mTorr of a 1.5% mixture of NO in He was placed in the Herriot cell and the laser's PZT ramped revealing dips in transmission of light to the InSb detectors.

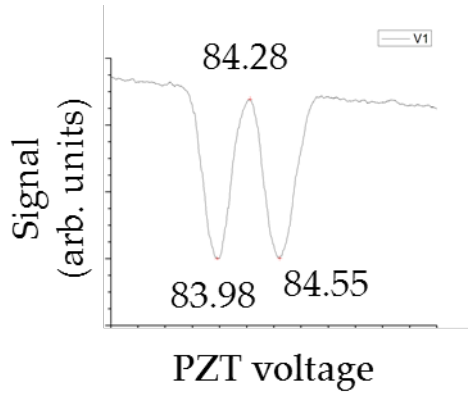

Figure 20: Numbers show laser PZT voltages of the two peaks and trough of the R(13/2) Ω = ½ doublet. The voltage of the second peak of the doublet vs. the first (here ΔV = 0.574 = 84.553 V – 83.979 V) were measured at different PZT voltage positions of the first peak

By adjusting the temperature of the laser, the voltage at which the doublet peak occurred is changed. The PZT voltage offset of the second peak relative to the first peak is graphed with respect to the PZT voltage of the first peak to obtain a non-linear relationship between the PZT voltage and the frequency shift per volt:

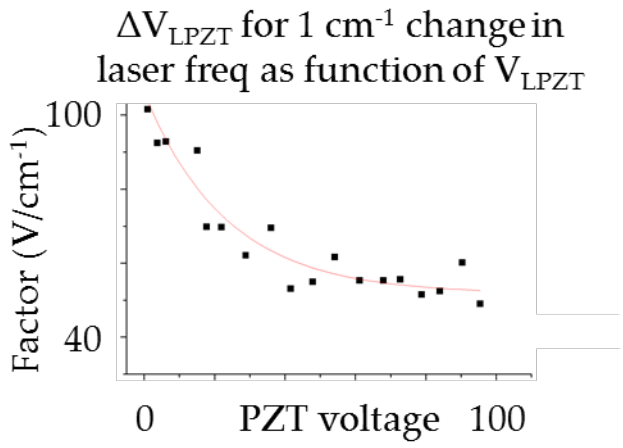

Figure 21: Laser PZT Voltage change to cause 1 cm^{-1} shift in Laser Frequency

From this function, we can convert PZT voltage to laser frequency. The fitting function was

$F(V) = (54.4 \pm 4.8\ V/cm^{-1}) \times \exp[-V/(23.4 \pm 5.3\ V)] + 51.7 \pm 3.0\ V/cm^{-1}$.

Laser noise / jitter

The effects of feedback of light back to the laser's cavity is treated in the "Feedback and Etaloning" section. An estimate for the linewidth of the 21052-MHF laser was obtained by locking the laser to the side of an NO absorption line by feeding back the signal from the reference cell to the laser PZT, allowing for slow frequency corrections (< 100 Hz) to control for laser drift.

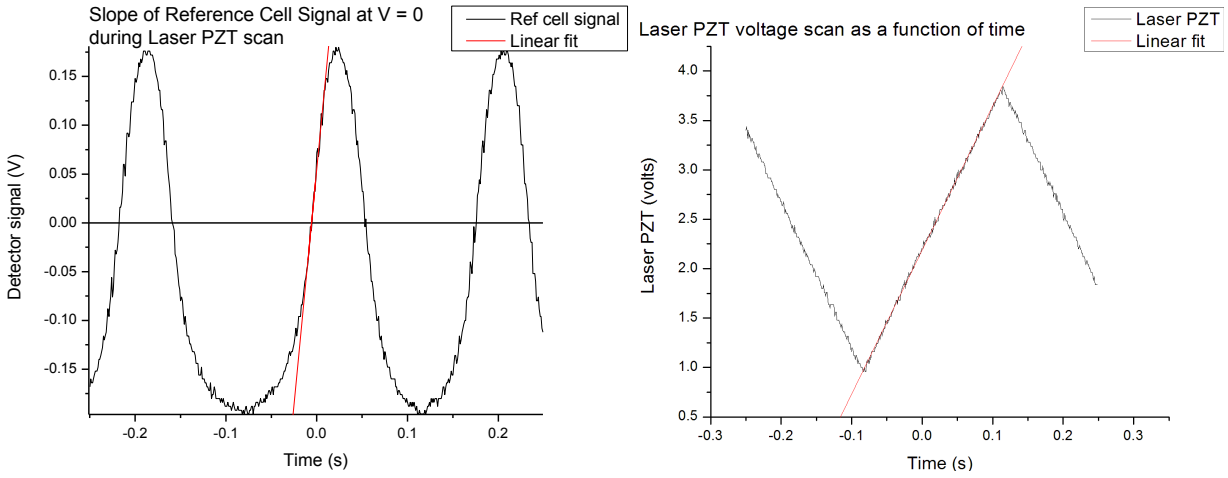

Figure 22: Finding the change in laser frequency Δv equivalent to a measured ΔV in the reference cell signal at the side of an absorption line. Left is slope of ref cell signal, right is laser PZT voltage ramp

With the laser locked to a point on the side of the absorption line with slope 9.40 V/s while the laser PZT was ramped at a rate of 14.60 V_{LPZT}/s (≈ 4380 MHz/s with the approximation from above that 1 V_{LPZT} ≈ 300 MHz), a 16 mV peak-to-peak noise level was measured on the oscilloscope, which is equivalent to 7.45 MHz on a time scale of 1.70 ms. Locked to the side of the reference cell line, a noise spectrum analyzer (SignalHound USB-SA44B) was used to quantify the frequency components of the noise in the detector signal.

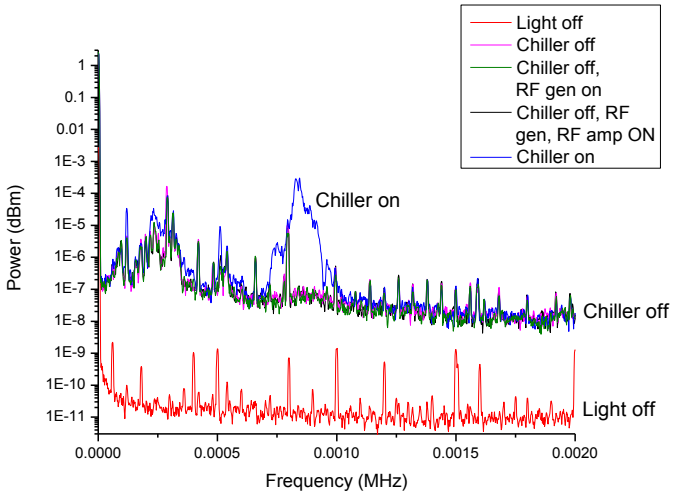

Figure 23: Noise levels at the side of an absorption line, with various external conditions

It was discovered that there were regular oscillations in frequency of the laser, which turned out to be caused by the pump system of the Lytron RC011 chiller (≈ 18 L /min), which was replaced with a home-made chiller and pump that used a much smaller water flow (< 0.5 L / min). The oscillations disappeared after this replacement was made.

Acousto-Optic Modulator

The acousto-optic modulator originally used was an Isomet 1207-B-6 Germanium AOM, originally coated for 10.2 µm. The AOM needed 35 W of 40 MHz RF power, provided by a NeOS N64025-45-3ASDFS RF driver amplified by a RFA-1150/4 high power amplifier. The high power requirement and etaloning from within the AOM necessitated the acquisition of a Gooch and Housego R37040-3-5.4 AOM, coated for 5.4 µm to reduce internal etaloning and requiring only 10 W of power for 80% diffraction efficiency (DE) of the IR beam into the 1st order beam. It was

found that even without an amplifier, the NeOS oscillator was able to produce 5.61 W of RF power that led to up to 75% DE into the 1st order.

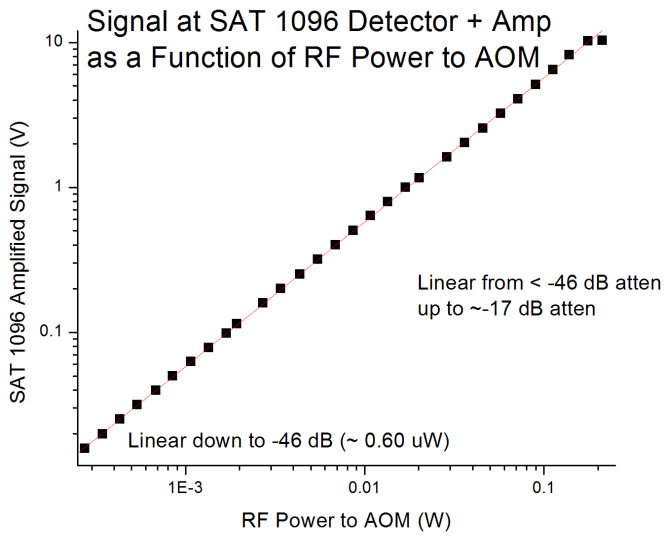

Figure 24: Voltage measured by detector as a function of RF attenuation

It was found that applying attenuators to the RF output before the AOM would decrease the signal on the SAT 1096 detector in an approximately linear fashion. From a linear fit to the log-log graph, we obtained the relationship:

$$V(P) = 57.54\,\mathrm{V\ W^{-1}} \cdot P^{1.00002} \tag{83}$$

where P is in watts.

Herriot cell

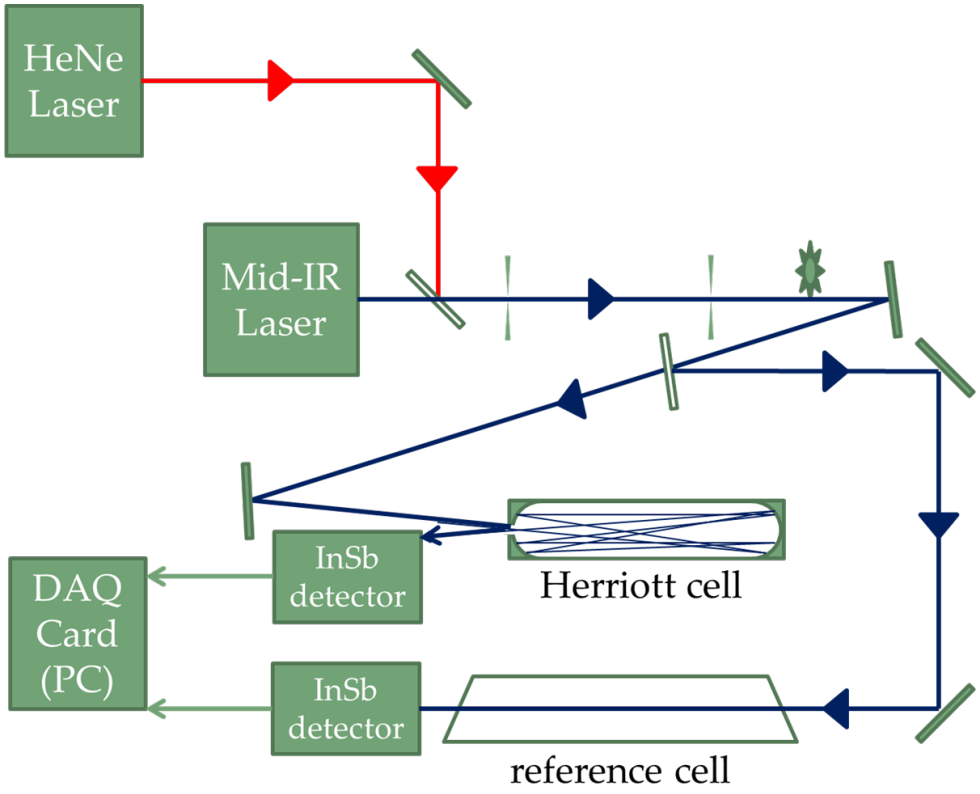

Figure 25: Schematic of apparatus used for NO detection with Herriot cell

The Herriot cell measurements were set up with three InSb detector signals: the main Herriot cell signal, a background signal, and a reference cell signal. The IR beam would be chopped by a mechanical chopper and split into three beams that would be detected by the separate detectors, whose output would be fed into SRS 510 Lock-in amplifiers and read by a PCI-DAS1402/12 DAQ card. The path length in air of the background signal was chosen to be approximately the same as that of the Herriot cell signal (57 in ± 0.5 in), so that absorption of atmospheric gases (e.g. water, CO_2) could be subtracted from the Herriot cell signal.

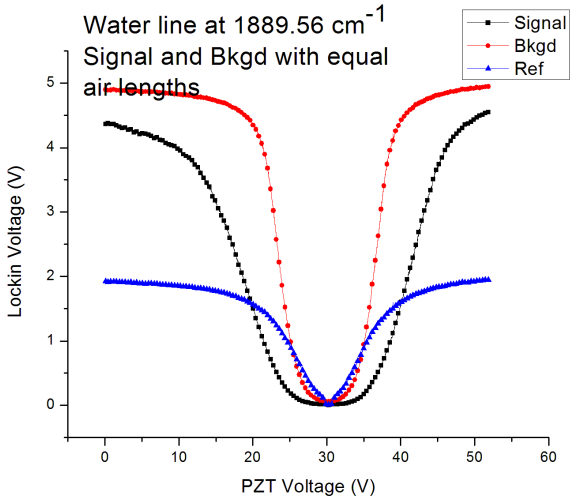

Figure 26: Measurement of water line with Herriot cell signal, background signal, and ref cell

Since the detectors for the background and the Herriot cell signal were the same model, the linear regime of the detector signals with respect to light intensity could be measured by using a smaller light level for one of the two signals, and plotting the two signals together on an X-Y plot as the laser is scanned over a water line with close to 100% absorption:

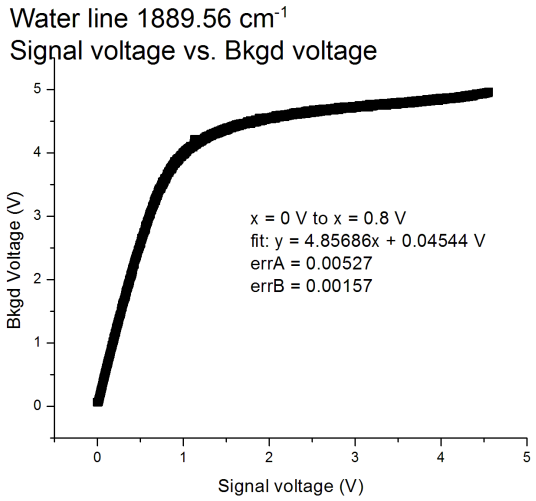

Figure 27: Comparison of Background detector voltage with Signal detector voltage to search for voltage / intensity saturation limit

From the graph we can see that the detector signal remains linear to ≈ 3.5 V.

Construction of Cavity

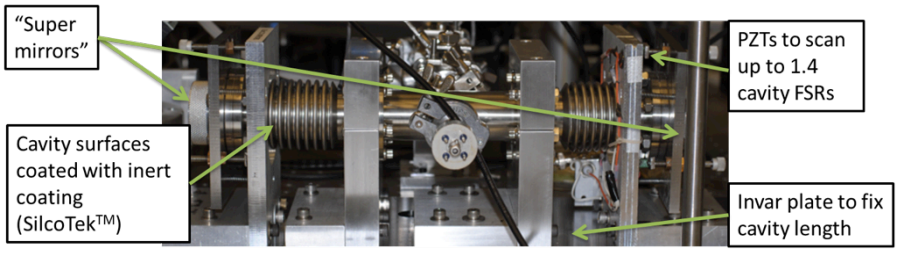

Figure 28: Photo of actual cavity

The optical cavity consists of two 1/2"-diameter mirrors from LohnStar Optics, one with radius of curvature R = ∞ (planar) and the other of R = 100 cm (concave). The mirrors are composed of a ZnSe substrate with an anti-reflective coating on the outsides of the cavity, and a high

reflectivity coating (R = 0.99975) on the inside of the cavity. The mirrors are placed in a stainless steel mount (blueprints below), which is in turn connected via a conflat to stainless steel bellows and a 1/2” KF tee to the other side of the cavity. The cavity length is 30 cm, and has a volume of ≈ 417 mL, and an internal diameter of 3 cm. The current cavity has its interior coated with SilcoNert 2000 (SilcoTek), a proprietary coating used to minimize gas adhesion to the walls of the cell.

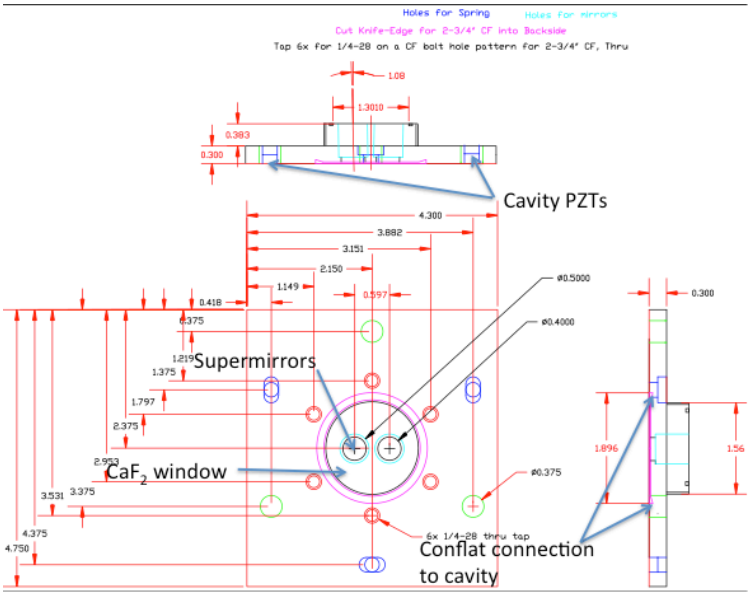

Figure 29: CAD drawing of cavity mounts

Light enters the cavity through two CaF2 windows, secured with O-rings and held in place by atmospheric pressure, or the screw lid when at atmosphere. The 1/2 ‘’ diameter supermirrors are held in place by retaining rings and O-rings. The length of the optical cavity is modulated with a set of three PZTs attached to one of the mirror mounts. Coarse alignment of the angle of the mirrors is done with the use of three adjustment screws on each mirror mount.

To estimate the power intensity within the cavity, the transmission and reflectivity of these mirrors were measured.

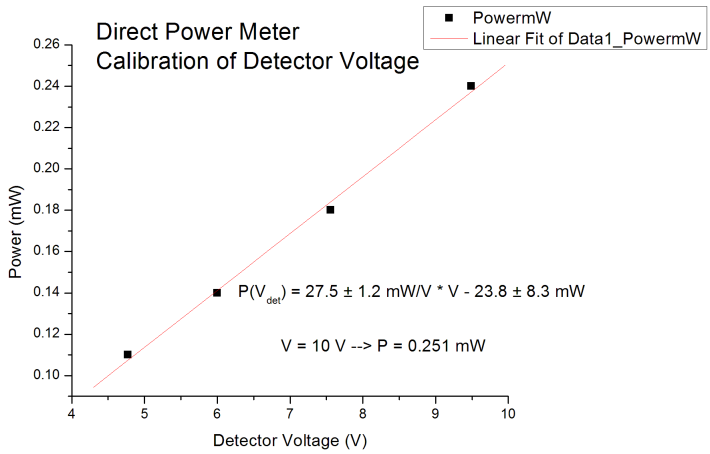

Figure 30: Power meter signal as a function of voltage at detector

To calibrate the use of the SAT 1096 InSb detector as a power meter, the output voltage from the detector was plotted against the size of the signal on a Scientech 372 thermal power meter. The laser power reaching the detector was changed by adjusting the RF attenuation to the AOM and a linear fit established:

$$P(V_{det}) = (27.5 \pm 1.2\,\mathrm{mW/V}) \cdot V_{det} - 23.8 \pm 8.3\,\mathrm{mW} \tag{84}$$

The full laser power was measured on the Scientech 372 power meter to be 25.4 mW, and when the supermirror was placed between the laser / AOM and the power meter, a signal of 0.241 V was observed on the SAT 1096 detector, corresponding to 6.07 µW according to the above equation. This indicates a transmission of 0.0239% .

With the cavity aligned, a ring-down time τ_0 of up to 4.2 μs, or equivalently a decay rate of 2.38×10^5 s^{-1} was observed, corresponding to a mirror reflectivity of 99.9723%, or a 277 ppm loss. The numbers reported by the manufacturer was 99.975% at 5.26 μm.

When scanning the cavity's PZT, the signal on the detector would spike to typical values of 5 V which is equivalent to $I_{transmitted}$ = 120 μW. Given the transmission of the mirrors (see section on "Calculations"), the intracavity light intensity is estimated to be:

$$I_{intracavity} = \frac{I_{transmit}}{T} \approx \frac{0.120\,\mathrm{mW}}{0.000239} = 0.50\,\mathrm{W} \tag{85}$$

This number of ≈ 0.5 W is used to estimate saturation.

The displacement of the PZTs as a function of voltage applied was measured by looking at the positions of the peaks of transmission of a HeNe laser after passing through the cavity, while the cavity PZTs are scanned with a voltage ramp from 0 V to 100 V (with a 10x voltage amplifier, or 0 to 10 V before the amplifier). With an approximate intermirror separation of L = 0.35 m, and with a HeNe wavelength of λ = 632.8 nm, one fringe is observed every $\Delta L = \frac{\lambda}{2}$.

With the observation that ≈ 15 fringes are observed per 10 V (before 10x amplifier), we can conclude that the PZT moves ≈ ΔL = 0.49 μm / V.

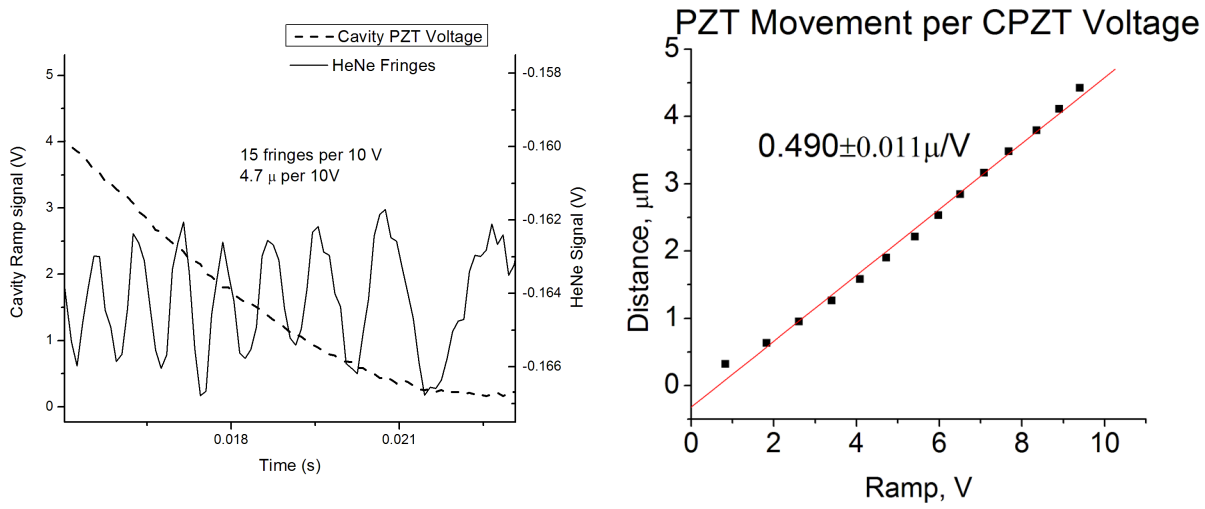

Figure 31: Counting of fringes per change in cavity PZT voltage ΔV_{CPZT}. Left is actual photodiode signal of HeNe laser through cavity, superimposed with simultaneous sinusoidal cavity PZT ramp. Right is calculated change in length of cavity ΔL as a function of V_{CPZT} / 10.

A more detailed fit of the positions of each HeNe peak as a function of cavity PZT voltage allows us to determine that there is a PZT voltage-dependent relationship between the change in frequency as a function of change in voltage.

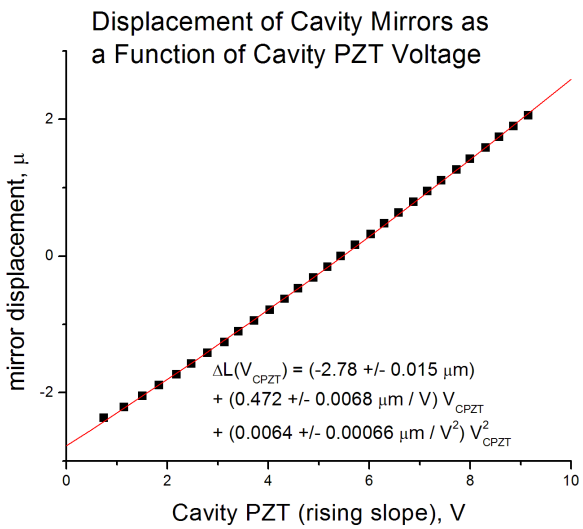

Figure 32: Position change of Cavity Mirrors as a function of Cavity PZT voltage

Using the fact that a change in the length of the cavity of λ/2 is equivalent to one cavity FSR, we can express one IR cavity FSR in terms of cavity PZT voltage:

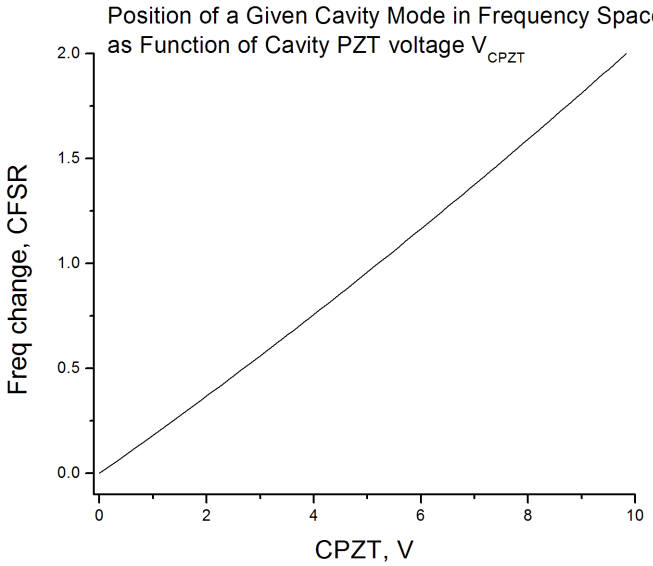

Figure 33: Non-linear fit of Figure 32, scaled to cavity FSR units

To measure the cavity FSR as a as a frequency, the following scheme was used:

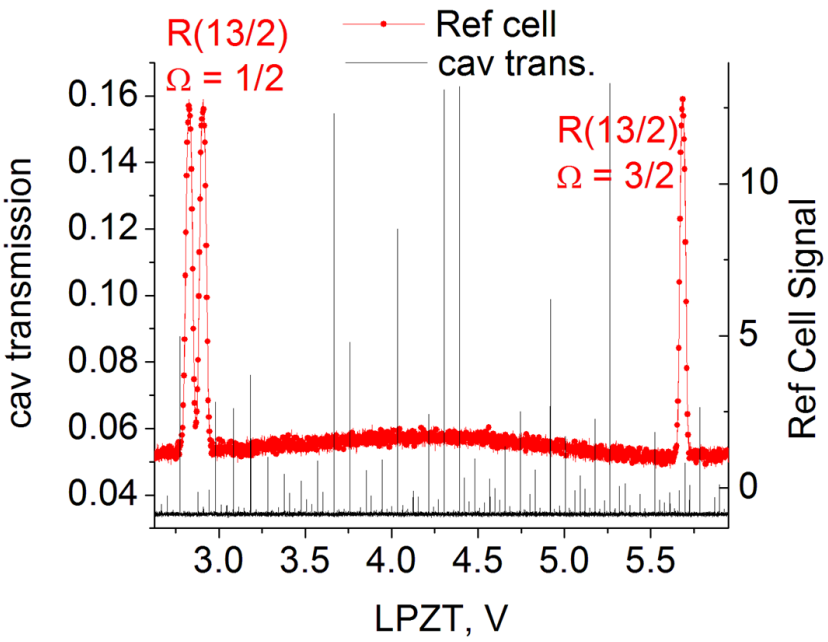

Figure 34: Cavity fringes detected, superimposed with simultaneous ref cell signal, during laser PZT voltage scan

The laser PZT was scanned continuously between two absorption lines, detectable using the reference cell. From the HITRAN database, the positions and therefore separation of the two peaks are well-known. As the laser's frequency changes, light from the TEM_{00} mode will only couple through the cavity when an integral number of half wavelengths fit in the cavity, and this happens every time the laser frequency increases by one cavity FSR. By looking at spikes in the light level of the cavity detector, we counted the number of tall peaks observed scanning from one absorption line to the next as seen with the reference cell, ignoring the transverse mode peaks. The tall peaks, or "fringes", correspond to cavity FSRs. Between two lines spaced 2.391 cm^{-1} apart, 167.64 "fringes" were observed, the fractional fringes estimated by considering the laser PZT voltage separation between the last cavity transmission peak and the

absorption line as a fraction of the laser PZT voltage separation between the previous two cavity transmission peaks. The cavity FSR in frequency is thus given by:

$$\Delta\nu_{CFSR} = \frac{\nu_{AbsPeak1} - \nu_{AbsPeak2}}{\#offringes} \tag{86}$$

The FWHM of the cavity modes can be calculated as a function of the FSR and the reflectivity R of the mirrors, which is determined by the empty cavity decay time τ_0:

$$\Delta\nu_{cavmode} = \frac{FSR_{cav}}{2\pi} \cdot \frac{(1-R)}{\sqrt{R}} = \frac{FSR_{cav}}{2\pi} \cdot \frac{L}{c\tau_0(1-\frac{L}{c\tau_0})} \tag{87}$$

or τ_0 = 2.5 µs, L = 0.35 m, and FSR = 428 MHz, we obtain a cavity FWHM of 60 kHz.

Etalon

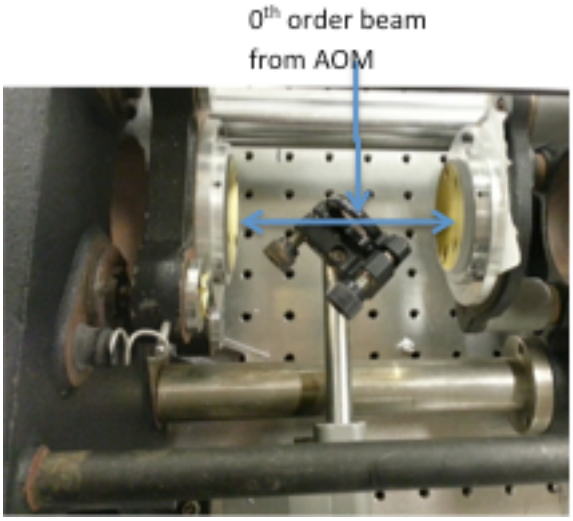

Figure 35: Photo and scheme of etalon

The etalon is a modified Tropel Fabry-Perot 350 Interferometer. This interferometer has three PZTs on one mirror, and three coarse adjustment knobs on the other mirror. Two f = 50 mm

curved mirrors are placed in a near confocal configuration, (see Figure 7). In this configuration, transverse modes are either close to the longitudinal modes in frequency, or approximately halfway between the longitudinal modes[8]. This makes mode-matching of the entering laser beam less critical because sharp peaks are obtained even if the entering beam must be decomposed into a number of non-TEM_{00} transverse modes. The etalon was aligned with the help of a co-propagating red (visible) HeNe laser.

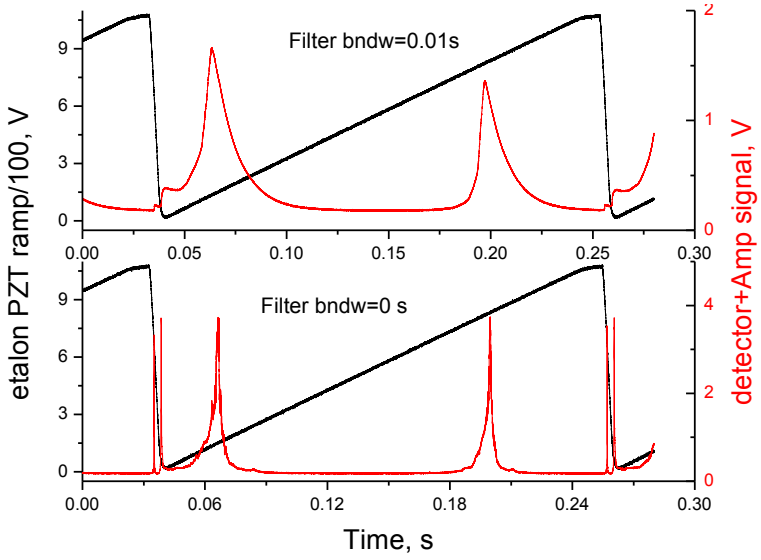

Figure 36: Etalon signal with simultaneous etalon PZT voltage ramp. The top graph is the signal with a low pass filter of time constant 0.01 s applied to the voltage signal.

To optimize alignment, a high voltage (1000 V) 20 ms saw-tooth ramp was applied to the cavity PZTs with a Burleigh RC-43 Ramp Generator, and the oscilloscope trace of the signal exiting the etalon to the detector was recorded. The coarse adjustment knobs were adjusted to maximize the height of the peaks. An optional low pass filter on the homemade op-amp circuit attached to the detector could be adjusted to better visualize the peaks without high frequency noise (> 100 Hz).

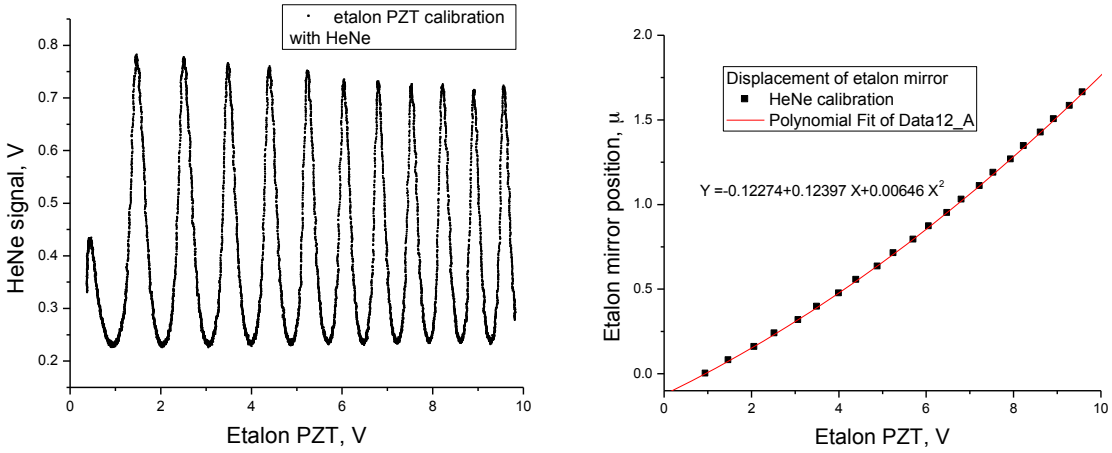

Figure 37: Etalon mirror position as a function of Etalon PZT voltage, done by counting fringes as in Figure 31

The linearity of the etalon PZTs as well as the free spectral range of the etalon in terms of etalon PZT voltage were measured by aligning the etalon for a stabilized HeNe (Coherent 200). Given the fixed frequency of a HeNe laser (632.8 nm), a movement of one etalon fringe after a given etalon voltage shift ΔV is equivalent to a movement of the spacing of the mirrors by $\Delta L = \frac{\lambda}{2}$. To measure the etalon FSR in terms of frequency, the same technique as for measuring the cavity FSR in the previous section was used. As the laser PZT was scanned between two absorption peaks separated by 1.0883 cm^{-1}, 43.59 transmission peaks at the etalon IR detector were observed, corresponding to an FSR of 748.48 MHz.

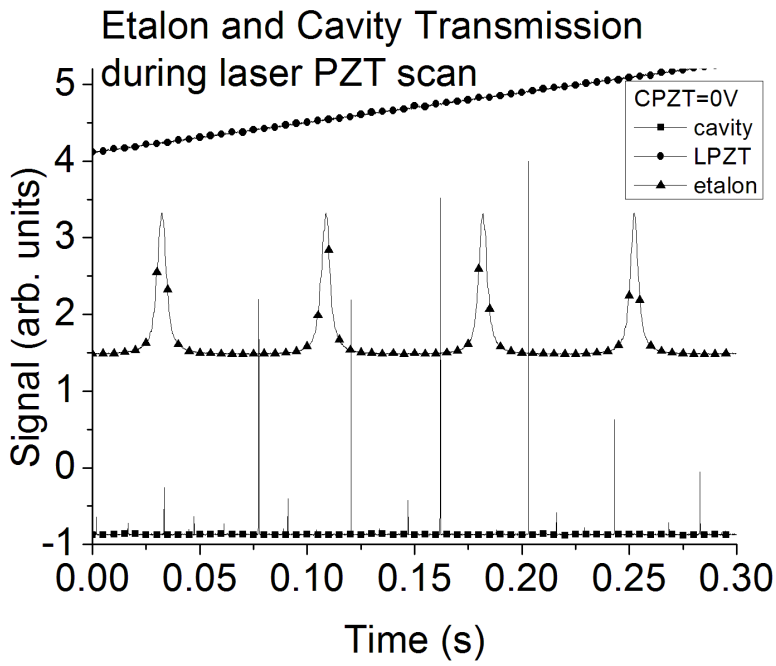

Figure 38: Etalon signal and cavity signal measured simultaneously, showing resonances of both, as laser PZT voltage is scanned

As a sanity check, the etalon signal and cavity signal were observed simultaneously as the laser PZT was scanned. It was seen that the spread in voltages between cavity modes was 0.571 times the voltage spread of the etalon, which is consistent with our measurements of CFSR = 427.6 MHz and etalon FSR = 748.48 MHz.

A Wavelength Monitor, designed by W. S. Woodward for the group of R. E. Miller, took the inputs of the etalon PZT voltage and the etalon detector signal, and outputs a (rescalable) etalon PZT voltage value where the etalon peak occurs. After every period of the etalon PZT ramp, the peak position voltage (referred to in our group as the “Miller box” voltage) is updated. This allows the monitoring of the laser’s frequency shift and jitter in relative to the

etalon. The Miller box was adjusted so that 1 etalon FSR (≈ 750 MHz) is equivalent to 10 V on the Miller box voltage output

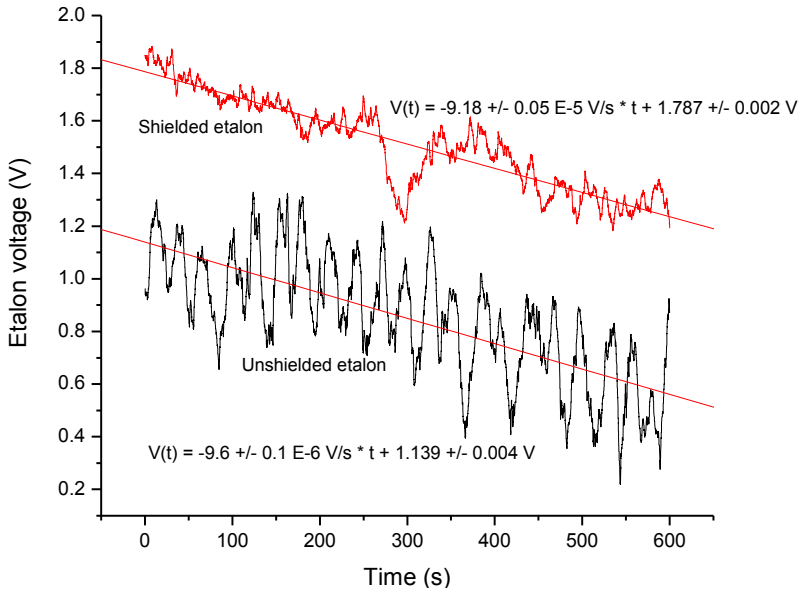

Figure 39: Etalon voltage drift and fluctuations with and without protective cover

After running the laser for ≈ 2.5 minutes to stabilize, the Miller box voltage was recorded as a function of time. It was observed that physically shielding the etalon reduced the standard deviation of the Miller box voltage (after the linear fit was subtracted) from 11 MHz to 5.4 MHz.

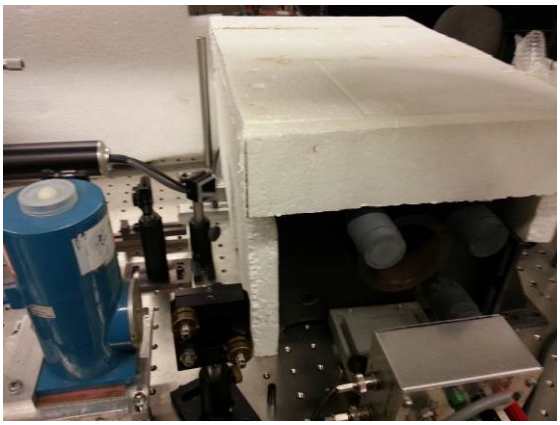

Figure 40: Picture of shielded etalon

Gas system

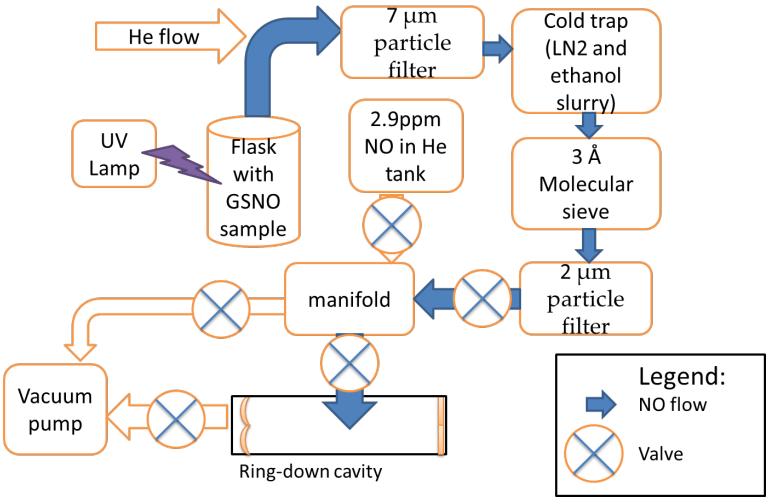

Figure 41: Schematic of gas / sample intake and flow system

The ring-down cavity is supplied with gas by a manifold that controls whether NO is being taken from a tank or from photolysis of a S-nitrosothiol sample. The cavity is evacuated by a Pfeiffer TCP 040 turbomolecular pump. The entrance and exit valves of the cavity are solenoid-actuated bellows valves (Edwards IPV16PKS). A capacitance monometer of full scale 100 Torr is located before the valve at the entrance of the cavity to measure the pressure of entering gas in the system outside of the cavity. Another of full scale 10 Torr is located outside of the exit to the cavity. After this gauge, there is a needle valve used to adjust gas flow when operating the system in a continuous flow mode. The manifold can be cleared by the turbomolecular pump between samples or when switching between the NO/He gas cylinder and GSNO samples.

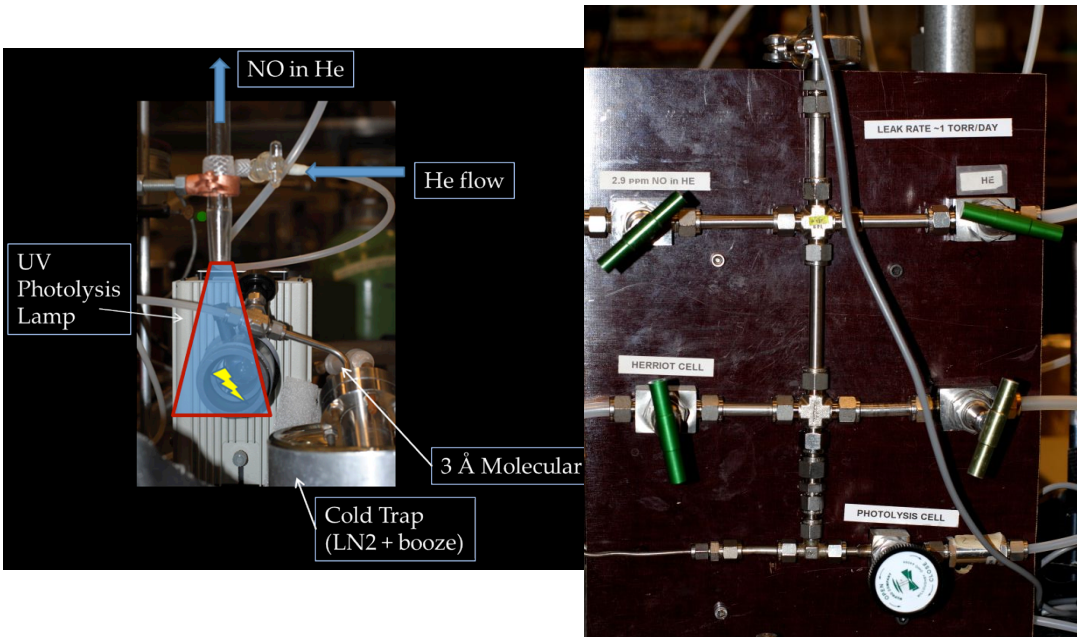

Figure 42: Photos of gas exchange manifold and UV photolysis system

To operate the GSNO biological NO system, a biological sample would be injected through a septum into a flask that would be subjected to UV light from an Oriel Xenon lamp. The released NO would be carried by helium through a mass flow controller (Brooks 5850E) into the manifold.

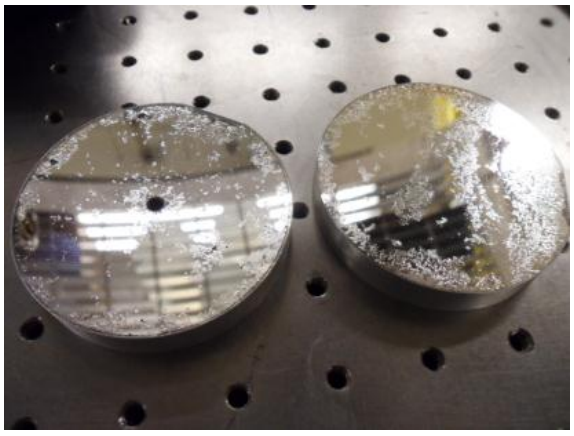

Figure 43: Herriot cell mirrors damaged by water / NO

After it was discovered that the mirrors in the Herriot cell setup were degraded due to water damage, it became necessary to filter out water from the GSNO intake system to avoid the same fate with the more expensive LohnStar supermirrors, which have a specialized coating for 5.2 μm. The system uses a bath of liquid nitrogen and ethanol at -116°C to lower the temperature of the gas flow to a point where water had negligible vapor pressure but above the boiling point of NO, which even at atmospheric pressure, is -152°C[15].

A molecular sieve also served to filter out water. Impurities in the sample were then passed through a 2 μm particle filter before entering the manifold.

For measuring theoretical limits of detection and Lamb dips of NO, there is a system separate from the GSNO collection system that is also connected to the manifold. A tank of 2.9ppm NO in Helium is connected via a variable leak valve (Granville-Phillips 203) to the manifold.

The gas system is designed to operate in two modes: closed cavity and continuous flow. In closed cavity mode, the cavity is filled to a fixed pressure with either a mixture of NO and He, or NO from biological sources. The cavity's entrance and exit valves are then closed and measurements taken. The advantage of this mode is the lower amount of gas consumed during the measurement and an intra-cavity gas composition that is relatively constant over time. The disadvantage of this method is that the experimental measurements must be conducted in a period of time that is short relative to the time it takes for air to leak into the cavity and NO to desorb from the cavity walls to partial pressures comparable in magnitude to the desired pressure. This is a problem at lower pressures, e.g. at 0.1 Torr where the pressure within the cavity can be doubled in the course of a scan lasting 15 min. With a cavity leak rate of only ≈

0.24 Torr / day, the dominant effect is the desorption of NO (see section “Difficulties: NO Sticking”).

The second mode is continuous flow mode. Gas flows from either an NO tank or the GSNO collection system, metered by the variable leak valve or the mass flow controller respectively, through the cavity, and metered by a needle valve at the exit to the turbomolecular pump. The advantages of this method are smaller, more constant pressures in the cavity due to the continuous evacuating action of the turbomolecular pump, and limiting the partial pressure of leaked-in gas and desorbed NO, especially when flow rates are high. With a leak-in rate of J_{leak} , an NO desorption rate of J_{desorb}, a pump evacuation rate of J_{pump} and a deposition rate of NO onto the walls of J_{depos} we can calculate the gas flow rate of J_{gas} necessary to maintain a given ratio of the partial pressure P_{unwant} to the total pressure P_{total} :

$$J_{\text{flow}} = \frac{J_{leak}}{1-\%\ \text{purity}} + J_{depos} - J_{outgassing} \qquad (88)$$
$$\%\ \text{purity} = \frac{P_{NO}}{P_{total}}$$

A disadvantage of using the flow mode is that the effective volume of the measurement is increased to 710 mL from 417 mL due to the inclusion of the volume of the gas sampling system in Figure 42.

Data Acquisition

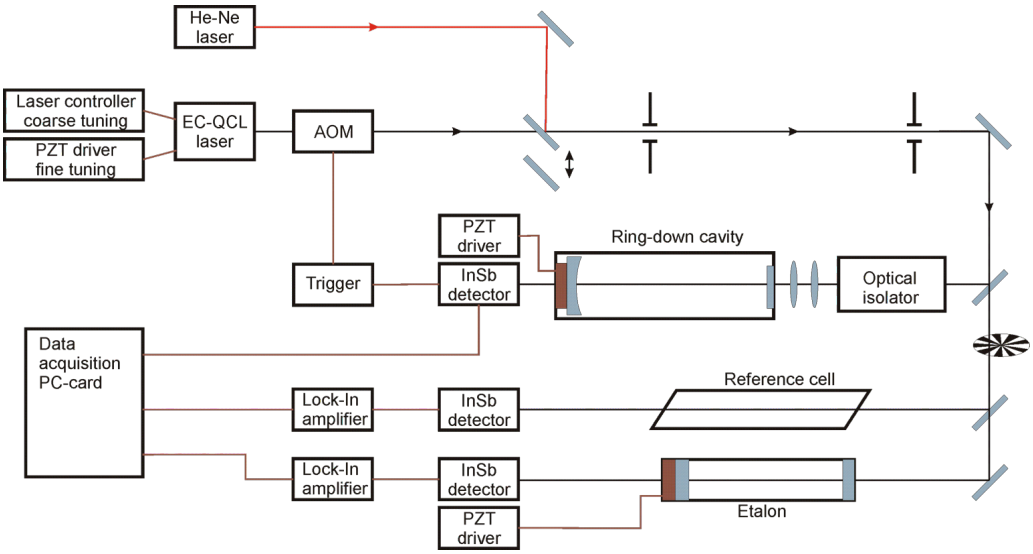

Figure 44: Schematic of Cavity Apparatus, showing optical and electrical paths

A software program written in Delphi Pascal collected data and scanned the laser over an absorption line. A ring-down is recorded as follows:

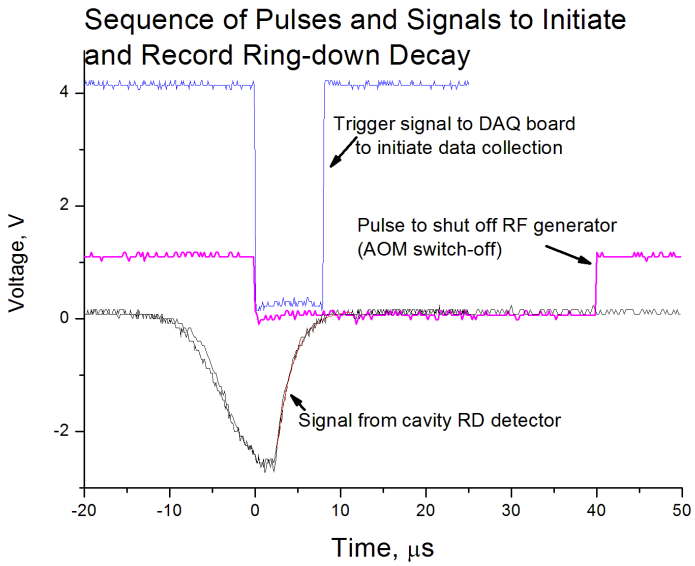

Figure 45: Ring-down signal, DAQ trigger signal, and AOM output signal at the time of a detected ring-down event

When laser light is resonant with a cavity mode, the light intensity within the cavity will build. The high speed SAT 1096 InSb detector after the cavity records an increasing voltage. When this voltage reaches a user-set threshold, a pulse from the SRS DG535 pulse generator is sent to the NeOS RF generator which switches off the RF sent to the AOM for a set time interval, usually 40 μs, or approximately ten times the decay time of the light signal. After a measured time of ≈ 2.6 μs after the pulse is initiated, the light level as measured from the detector begins decaying. This signal is then recorded with the high-speed detector. After 40 μs the pulse shutting down the RF is terminated and the AOM again begins transmitting the laser to the cavity until the next buildup of light intensity for a ring-down.

In order for light in the cavity to build in intensity, the laser must be in resonance with one of the cavity modes. To record a spectrum over an absorption line, the cavity mode and laser frequency must be simultaneously scanned and kept in resonance with each other.

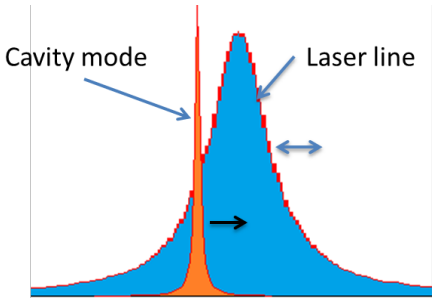

Figure 46: Relative widths of cavity mode an laser line width. The cavity mode is scanned in one direction while the laser frequency is dithered around it to allow it to follow the cavity in frequency

The laser's linewidth of ≈ 8 MHz is comparatively wider than the cavity mode width of ≈ 60 kHz. Due to jitter of the laser frequency, the laser and cavity mode cannot be simultaneously linearly scanned and remain in resonance without feedback correction. To do this, the laser frequency was dithered by applying a sinusoidal voltage offset to the laser PZT. The software program changes the cavity's resonant mode by linearly changing the cavity PZT voltage, and at the same time it applies a shift in the DC level of the laser's PZT voltage that is equivalent in frequency shift to that of the cavity mode. The program records the voltages on the sinusoidal modulation where the ring-downs occurred and takes the mean value. The deviation of this value from the DC offset is an indication of the divergence of the laser's frequency from the cavity mode. The program then adjusts the laser PZT's voltage by a proportionality constant times this error to

keep the laser locked to the cavity mode as the cavity's length, and thus frequency of its modes, continues to be scanned. At the same time, the signal from the etalon is recorded.

To calculate the voltage adjustment ΔV_{LPZT} required for the laser PZT as the cavity PZT voltage V_{CPZT} is changed, we used from our measurements in the previous section that the cavity modes move one FSR of 428 MHz upward when the cavity PZT voltage is decreased by 49 V. A 428 MHz upward shift in the laser frequency is effectuated by increasing the laser's PZT voltage by 1.43 V. Therefore the program scans over an absorption line from low frequency to high by scanning the cavity PZT downward and the laser PZT upward, with the ratio of laser PZT change to cavity PZT change given by:

$$\Delta V_{LPZT} = -\frac{1.43}{49}\Delta V_{CPZT} \tag{89}$$

The software program's general scanning algorithm when recording a spectrum is as follows:

1.) Laser stepping motor stepped to a position just away from a peak

2.) Laser power turned on

3.) Cavity voltage (V_{CPZT}) set to highest value (4.9 V before 10x amplifier)

4.) Wait 120 s to stabilize laser's frequency from thermal effects

5.) Laser PZT (V_{LPZT}) initialized to 0 V + approximate laser line width (6 MHz ≈ 20 mV on laser PZT)

6.) V_{LPZT} dithered with triangle wave of amplitude V_{amp} = 20 mV

7.) V_{LPZT} scanned one full FSR (1.43 V) up, voltages when ring-downs occur recorded

8.) V_{LPZT} set to voltage in search with the longest τ.

9.) Begin V_{CPZT} sweep downward at a steady pace (# of steps of ΔV_{CPZT} per minute)

10.) At every step of ΔV_{CPZT}, V_{LPZT} ramped up by equivalent step

$$\Delta V_{LPZT} = -\frac{1.43}{49}\Delta V_{CPZT}$$

11.) Feedback applied to V_{LPZT} to keep DC offset voltage in dithering wave where ring down occurs to be approximately zero, or if there's a big standard deviation, to where the RDs have the longest τ (center of cavity excitation).

12.) When V_{CPZT} gets down to 0 V then it is quickly brought back up to 49 V.

13.) V_{LPZT} adjusted until we get to same etalon position as before (number of peaks passed and approximate location of etalon peak when V_{CPZT} reached 0 V). The adjustment might be due to laser following V_{CPZT} when it is reset to 49 V. There may need to be a little overlap with end of last cavity sweep in order to get V_{LPZT} to center of cavity excitation at 49 V. Laser PZT might need to do another search from – FSR/2 to +FSR/2 (-0.72 V to +0.72 V) and go to closest TEM_{00} peak that overlaps the previous scan based on etalon data.

14.) Go back to step 9 and repeat until desired frequency range covered as measured by etalon counter.

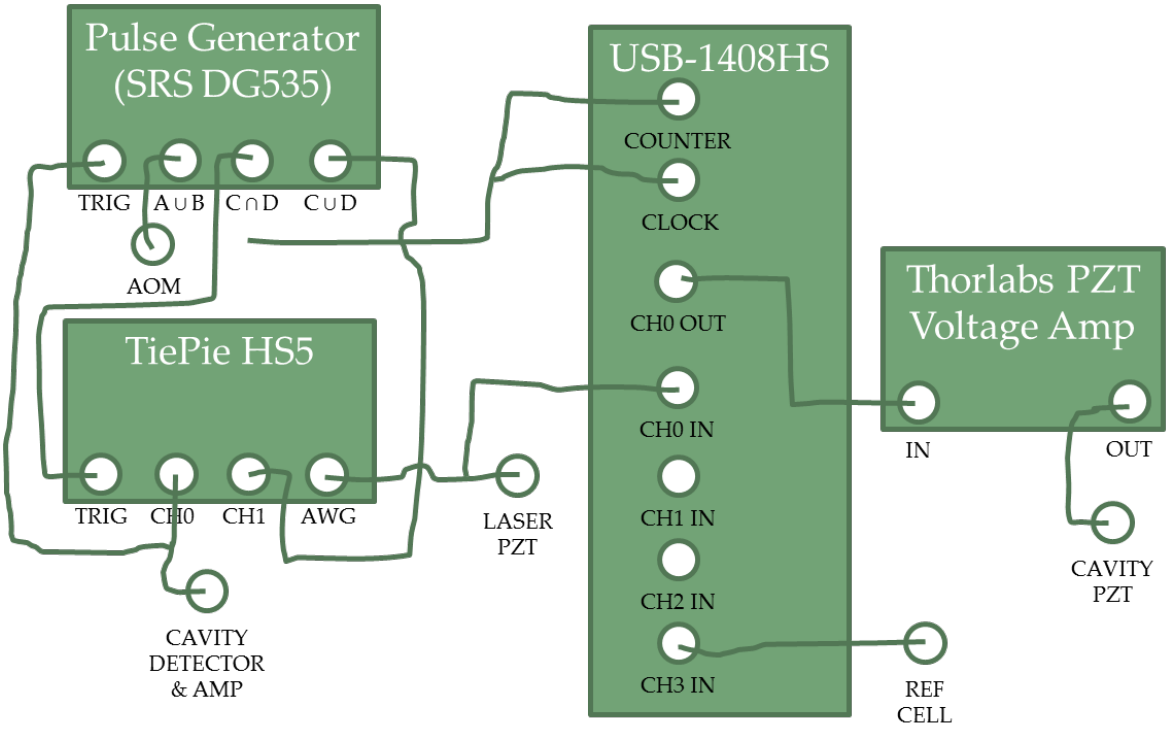

Figure 47: Scheme of Electronics of Ring-Down Triggering and Data Acquisition

The laser PZT was controlled by a TiePie HS5 Digital Oscilloscope's Arbitrary Waveform Generator (AWG) output, which outputs a sine wave with a DC offset. The cavity PZT voltage, ring-down cavity detector signal, and Miller box voltage were read by a Measurement Computing USB-1408HS DAQ device. For the purposes of calibrating the laser frequency at the moment of ring-downs, the laser PZT voltage output by the HS5 AWG was also input into the USB-1408HS device. This device recorded data at 50 kSamples/s with 14-bit resolution from -4 V to 4 V, or a digitization error of 0.98 mV. This device also had an analog to digital output from 0 V to 4.096 V in 1 mV increments which was fed to a 15x voltage amplifier to control the cavity PZT during a scan.

Feedback and Etaloning

Theory

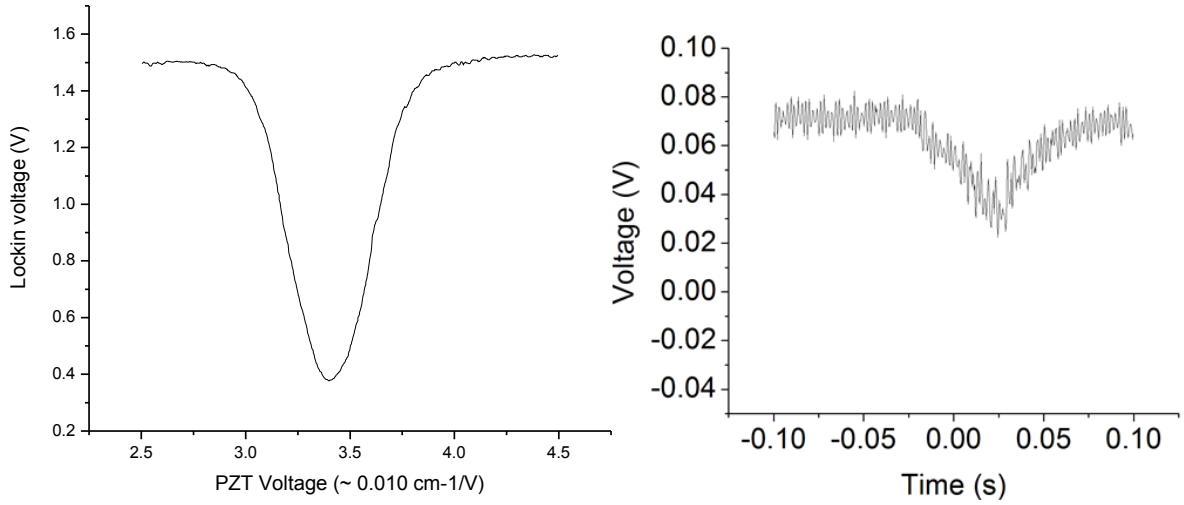

Figure 48: Absorption signal with (right) and without (left) undesirable feedback to the laser's external cavity.

"Etaloning" results from internal reflections within an optical element that alternatingly constructively and destructively interfere with each other, creating an unintentional and unwanted etalon. The graph on the left shows minimal etaloning. The graph on the right is due to internal etaloning within the Ge crystal comprising the previous AOM model, the ISOMET 1207-B-6. The etaloning is due to the anti-reflective coating being for the wrong wavelength (10.2 μm vs. 5.2 μm). This was one of the reasons for replacing the AOM.

Laser feedback occurs when laser light is either directly reflected or scattered off the surfaces of optical elements and reenters the laser's resonant cavity. This destabilizes the laser's output frequency because the returning light, upon entering the cavity, is decomposed into several

resonant modes of the laser's cavity, which are not perfectly degenerate. These modes may be pumped by the quantum cascade and cause the laser to jump in frequency and fluctuate in intensity as the level of light in each resonant mode changes due to the feedback.

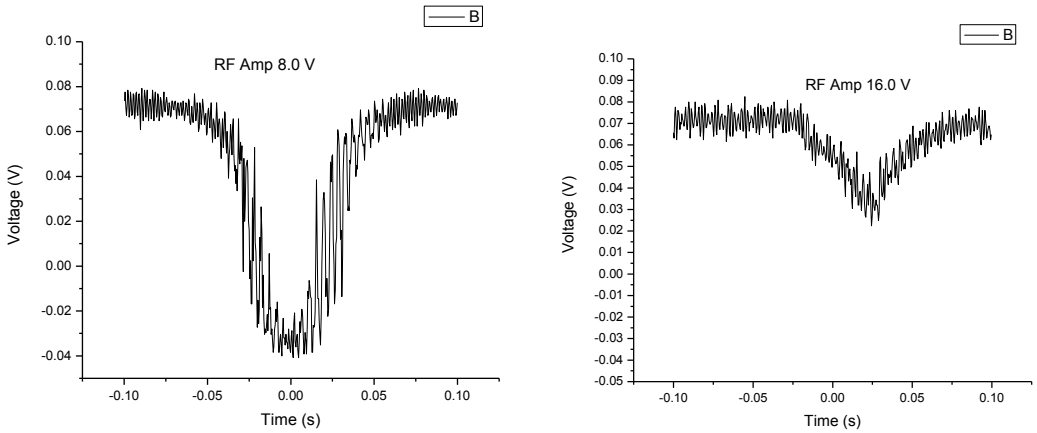

Figure 49: Low (left) vs. high (right) level of feedback to the laser cavity.

Rapid frequency jitter induced by feedback can effectively "wash out" an absorption line when the line is scanned over at a relatively slow rate (e.g. 0.20 s) compared to laser jitter below the millisecond time scale , due to the laser jumping on and off the absorption line. The graph on the left shows a low level of laser feedback (along with unintentional etaloning) due to the 1st order beam intensity propagating through the system being reduced by lowering the power to the RF Amplifier. The graph on the right shows a high level of laser feedback due to a stronger 1st order beam intensity.

Unintentional and Intentional Laser locking

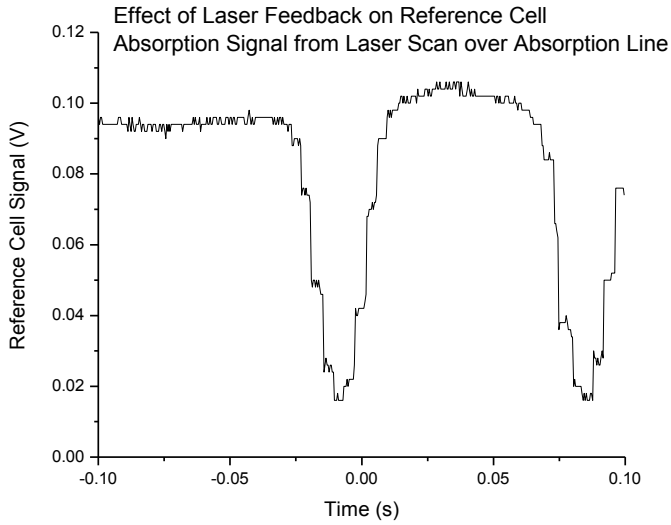

Figure 50: Laser locking in frequency even when laser PZT is scanned continuously

The graph shows the effect of feedback on the reference cell signal of an absorption line. The jagged pattern occurs when the laser frequency is "stuck" even while the laser PZT is being ramped. The laser PZT changes the length of the laser's cavity, but the much longer effective "cavity" formed by the laser head and the back reflection of an optical element somewhere else in the CRD setup does not significantly change due to the laser PZT, which acts to keep the old frequency lasing.

Isolator methods

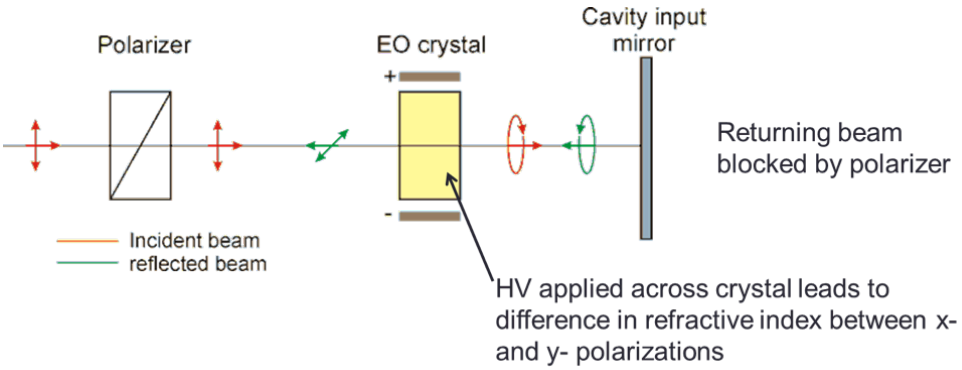

Figure 51: Diagram of EOM + polarizer isolation

The first method to reduce feedback was the use of a diagonally-set MgF_2 polarizer combined with a CdTe crystal. The CdTe crystal is susceptible to the electro-optic or Pockels effect. When a large voltage (for our crystal, ≈ 2.6 kV) is applied across the crystal, the index of refraction for light passing through the crystal will change depending on the polarization of light. The voltage across the CdTe was increased so that a $\pi/2$ phase shift occurs between the horizontal and vertical polarizations of light. This causes diagonally polarized light to exit the crystal circularly polarized. Upon reflection from the cavity entrance mirror, the circular light's helicity (left-handed vs. right-handed) is flipped. When this circularly-polarized light again goes through the CdTe crystal, the light becomes linear polarized, but this time orthogonal to the original light, and thus blocked by the polarizer.

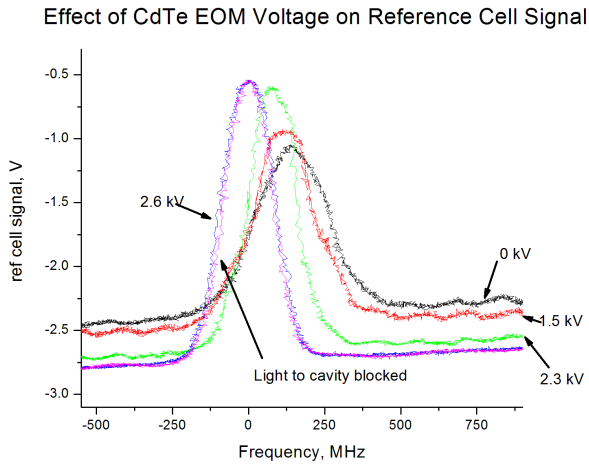

Figure 52: Scan of reference cell absorption line at various EOM voltages. Compare with absorption line when cavity is blocked, eliminating direct feedback from cavity mirrors

It can be seen from the graph above, measuring the reference cell signal during a laser frequency scan with light entering the CRDS cavity, that the "washing out" of the peak decreases as the voltage is increased toward 2.6 kV, at which point the absorption peak signal is similar to when the light to the cavity is blocked.

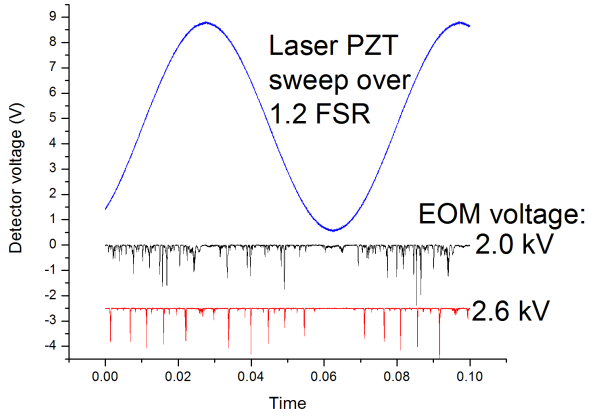

Figure 53: Cavity modes at EOM voltage below optimum (2.0 kV) and at optimum (2.6 kV)

Indeed, one can see that setting the CdTe voltage to 2.6 kV improves the signal from the cavity detector during a laser PZT sweep, reducing the jumping of the laser to various higher-order cavity modes.

The disadvantage of the polarizer-EOM setup is that the light leaves circularly polarized. If there are mirrors between the polarizer-EOM system and the cavity, they will change the relative intensities of the s- and p- polarizations of light, and therefore light bouncing back from the cavity and through the EOM in the reverse direction will not be polarized at 45° and thus not completely blocked by the polarizer. By blocking and unblocking the etalon and reference cell, it was found that light was reflecting back from these elements and causing feedback because the laser's frequency jitter was reduced when these elements were blocked.

A Faraday isolator was later purchased from Innovation Photonics. Its input and output polarizers are Ge plates set at Brewster's angle. The isolator was rated to transmit 90% of the light, but power meter measurements with the Scientech 372 revealed that only 53% of the laser power was transmitted through the isolator (60 mW in, 34 mW out). The angle of the two polarizers were optimized so that less than 0.5 % of light would be able to pass through in the opposite direction (< 0.1 mW out, 34 mW in), or an isolation of > 23 dB.

Calculations

Determining Concentration from cavity decay rate

The integrated line strength S is reported in HITRAN[13] and is:

$$S = \int_{-\infty}^{+\infty} \sigma(\tilde{\nu})\, d\tilde{\nu} \tag{90}$$

In the low pressure limit, the line shape is approximately Gaussian, which when normalized, takes the form:

$$\sigma(\tilde{\nu}) = S\sqrt{\frac{4\ln 2}{\pi \Delta\widetilde{\nu_D}}}\exp\left(-\frac{4\ln 2 \cdot \tilde{\nu}^2}{\Delta\widetilde{\nu_D}^2}\right) \tag{91}$$

Given the empty cavity τ_0 and a measured τ as well as the Doppler width of 128 MHz, we can calculate the concentration n at any point on the absorption curve:

$$cN\sigma(\tilde{\nu}) = c\frac{cnN_A}{V}\sigma(\tilde{\nu}) = \frac{1}{\tau(\tilde{\nu})} - \frac{1}{\tau_0} = k(\tilde{\nu}) - k_0 \tag{92a.}$$

$$n = \frac{\frac{1}{\tau(\tilde{\nu})} - \frac{1}{\tau_0}}{c\sigma(\tilde{\nu})N_A} \tag{92b.}$$

For $\tau = 3.0\times10^{-6}\,\mathrm{s}; \tau_0 = 4.0\times10^{-6}\,\mathrm{s}$
$V = 3.17\times10^{-4}\,\mathrm{m}^3; \sigma = 1.25\times10^{-21}\,\mathrm{m}^2$ we obtain n = 14 nmol.

Whiting approximation to Voigt profile

The Voigt profile cannot be calculated analytically. However we used the following approximation for σ(v), which incorporates a Lorentzian and Gaussian width, from Whiting et al.[16]:

$$\Gamma_L = \gamma_{self} \cdot P_{gas} + \gamma_{He} \cdot P_{He} + \frac{A^{1/2}}{c}$$

Lorentzian width from self- and He-broadening and spontaneous lifetime

$$\Gamma_D = \sqrt{\frac{8k \ln 2}{c^2}} \sqrt{\frac{T}{m}} f_0$$

Doppler/Gaussian width

$$\Gamma_V = 0.5346\delta_L + \sqrt{0.2166\Gamma_L^{\ 2} + \Gamma_D^{\ 2}}$$

Approx. Voigt "width"

$$x = \frac{\Gamma_L}{\Gamma_V}$$

$$\Sigma_0 = \frac{S}{2\Gamma_V(1.065 + 0.447x + 0.058x^{2)}}$$

Line strength S

$$y = \frac{|f - f_0|}{\Gamma_V}$$

$$\sigma = \Sigma_0[(1-x)\exp(-0.693y^2) + \frac{x}{1+y^2} + 0.016(1-x)x(\exp(-0.0841y^{9/4}) - \frac{1}{1+0.021y^{9/4}}))]$$

Absorption cross-section with Whiting approx.

The approximation's values for the intensity, Gaussian width, and Doppler width have their maximum deviation from the analytic Voigt result when the Lorentzian width is approximately half that of the Gaussian width. With NO self- and He- pressure broadening coefficient of ≅ 2.5 MHz/Torr, this occurs when the pressure is ≅ 28 Torr. At this region, the deviation is still less than 1%.

Transverse mode spacing

The spacing between transverse modes of a cavity is:

$$\Delta\nu_{transv} = \frac{c}{2\pi L}[\arctan(\frac{z_{M1}}{z_R}) - \arctan(\frac{z_{M2}}{z_R})] \quad (93)$$

where z_{M1} and z_{M2} represent the respective distances of the two mirrors of the cavity from the waist. Since the first mirror is planar, z_{M1} = 0 m. Then z_{M2} = L = 0.35 m.

From Equation 36:

$$z_R{}^2 = \frac{L(-R_1-L)(R_2-L)(R_2-R_1-L)}{(R_2-R_1-2L)^2}$$

where R_1 is the radius of curvature of the first mirror and R_2 the radius of the second, we use the fact that for a planar mirror $R_1 = \infty$ and take the limit:

$$\lim_{R_1\to\infty} z_R^2 = \frac{L(-R_1)(R_2-L)(-R_1)}{R_1^2} = L(R_2-L) \tag{94}$$

Since R_2 = 0.5 m, we find that z_R = 0.229 m.

Inserting this value into the transverse mode-spacing equation, we get that $\Delta\nu_{transv}$ = 135.2 MHz, compared to the longitudinal separation, which is the cavity's FSR = 428 MHz.

Mode-matching

Using a Spiricon Pyrocam II pyroelectric camera, the beam profile was measured at different distances z to characterize the beam.

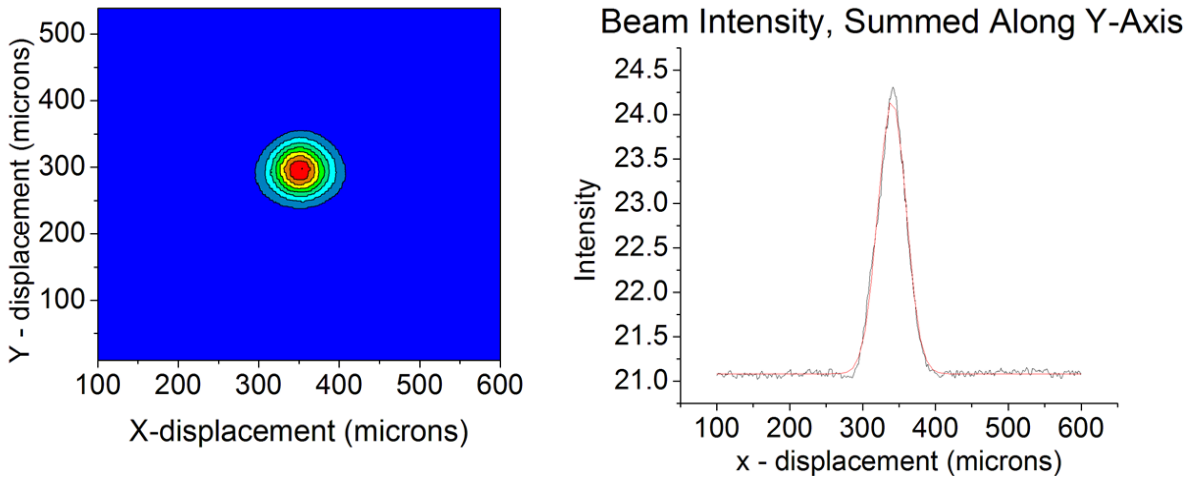

Figure 54: Example beam profile measured with Pyrocam, with cross-section in x-direction

The Pyrocam can be set to output a bitmap whose pixels correspond to a rate of change in light intensity, requiring the laser to be chopped at 48 Hz. Intensities of the pixels along the x- axis and the y-axis were separately summed and fitted to Gaussian distributions to determine the beam width at a given z. The data for $w_x(z)$ and $w_y(z)$ were then fitted to the equation for the width of a Gaussian beam:

$$w(z)^2 = w_0^2 + \frac{(z - z_w)^2 \cdot \lambda}{\pi} \tag{95}$$

where w_0 is the beam waist, the minimum width of the beam, and z_w the z-position of this waist, and lambda the wavelength. Although the laser's wavelength is ≈ 5.3 μm, because the laser is not a perfect Gaussian beam, the "effective" wavelength according to the fit differed. Using the effective wavelength found by the fit allows us to better model the complex beam parameter than if we had coerced the fit to use λ = 5.3 μm.

Once w_0 is known, $q(z = z_w)$ can be determined, because the radius of curvature R(z) is infinite at the waist. This means that:

$$q(z_w) = \left[\frac{1}{R(z_w)} - i\frac{\lambda}{\pi \cdot w(z_w)^2}\right]^{-1} = i\frac{\pi \cdot w_0^2}{\lambda} = iz_R \tag{96}$$

From our measured data, the best fit value for the x-waist size was w_{0x} = 0.88 mm and the y-waist size was w_{0y} = 1.06 mm. For our program, we took the geometric mean, w_0 = 0.966 mm. The arithmetic mean of the two effective wavelengths fitted was 5.82 μm.

It was found that the 1st order beam's shape after the AOM was not easily modelable as a beam simply passing through a 5.0 cm thick "window" made of n = 4.0 material (Ge), and thus the

beam profile was measured after the isolator and AOM, and z = 0 was defined to be the position of the AOM's "center" of diffraction (where the 1st order beam and 0th order beam intersect). The x- waist was found to be -0.232 m before the AOM and the y- waist position was 0.232 m in front of the AOM, so that the arithmetic mean is almost exactly at z = 0.

We can use the equation to calculate the Rayleigh range:

$$z_R = \frac{\pi \cdot w_0^2}{\lambda_{eff}} \tag{97}$$

to find that z_R = 0.5037. Thus the complex beam parameter leaving the AOM is:

$q_{AOM}(z) = z - z_W + i\, z_R = z + 0.5037i$.

From the cavity side:

The cavity is composed of a planar entrance mirror ($R_1 = \infty$), a free space segment of $z_{cav} = L$ = 0.35 m, and a back mirror of R_2 = 0.5 m. The resonant TEM_{00} mode of the cavity will duplicate itself after making a round trip of these optical elements, or equivalently, going through the following ABCD matrix:

$$\begin{aligned} M_{cav} &= M_M(R=\infty) \cdot M_D(d=L) \cdot M_M(R=0.5) \cdot M_D(d=L) \\ &= \begin{pmatrix} 1 & 0 \\ 0 & 1 \end{pmatrix} \cdot \begin{pmatrix} 1 & 0.35 \\ 0 & 1 \end{pmatrix} \cdot \begin{pmatrix} 1 & 0 \\ -\frac{2}{0.5} & 1 \end{pmatrix} \cdot \begin{pmatrix} 1 & 0.35 \\ 0 & 1 \end{pmatrix} \\ &= \begin{pmatrix} -0.4 & 0.21 \\ -4 & -0.4 \end{pmatrix} \end{aligned} \tag{98}$$

From setting $q_{in} = q_{out}$ in the equation:

$$q_{out} = \frac{Aq_{in} + B}{Cq_{in} + D}$$

we obtain that:

$$q_{cavity} = \left[\frac{D-A}{2 \cdot B} - i \frac{\sqrt{1-\left(\frac{A+D}{2}\right)^2}}{|B|} \right]^{-1} \tag{99}$$

and find that qcav = 0.229 i

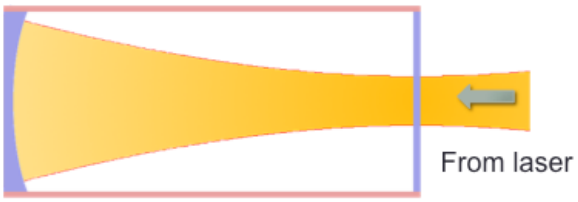

Figure 55: Schematic ideal profile of beam within cavity

Because our cavity's entrance mirror is a planar mirror (R = ∞), this q represents the complex beam parameter at the entrance of the cavity: $q(z = z_{total}) = q_{cav}$. Using the equation for beam width:

$$w(q) = \sqrt{\frac{\lambda_{eff} \cdot |q|^2}{\pi \cdot Im(q)}} \tag{100}$$

we can see that the beam width at the entrance of the cavity is $w(z_{total}) = 0.693$ mm.

The goal of our mode-matching calculation is to find where to put two lenses of focal lengths f_1 and f_2 so that, when the laser beam is propagated to the cavity, it will match the q of the cavity. Different lenses resulted in different placements of the two lenses, sometimes being put in an impossible position, such as being too close to a mirror. Two Thorlabs CaF_2 lenses of nominal focal lengths 7.5 cm and 10 cm, were found to result in the easiest placement.

The focal length specified for the two lenses on the Thorlabs website was measured for 0.588 µm light. Due to dispersion, or equivalently, a different index of refraction, the focal length at 5.26 µm is different from at 0.588 µm. Using the radii of curvature and thicknesses data from Thorlabs, the focal length of the two lenses can be calculated using the lensmaker equation:

$$\frac{1}{f} = (n-1)\left[\frac{1}{R_1} - \frac{1}{R_2} + \frac{(n-1)d}{nR_1R_2}\right] \tag{101}$$

with R_1 , R_2, and d defined as in the diagram below:

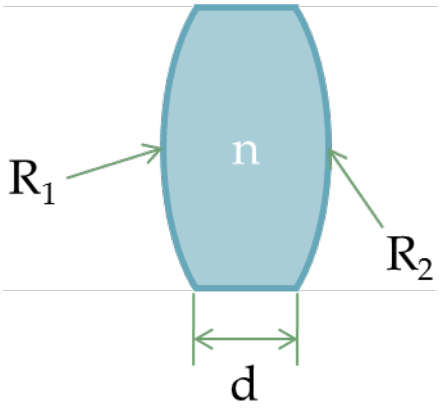

Figure 56: Diagram of a thick lens

Using this, the first lens's focal length was calculated to be f_1 = 8.22 cm. And the second lens's was f_2 = 10.96 cm. We can propagate the complex beam parameter of the laser from the AOM which is:

$q_{AOM}(z) = z - z_W + i\, z_R = z + 0.5037i$

using the ABCD matrix in the example of Equation 32:

$$M_{propag} = \begin{pmatrix} 1 & z_3 \\ 0 & 1 \end{pmatrix} \begin{pmatrix} 1 & 0 \\ -\frac{1}{f_2} & 1 \end{pmatrix} \begin{pmatrix} 1 & d \\ 0 & 1 \end{pmatrix} \begin{pmatrix} 1 & 0 \\ -\frac{1}{f_1} & 1 \end{pmatrix} \begin{pmatrix} 1 & z_1 \\ 0 & 1 \end{pmatrix} = \begin{pmatrix} A_{propag} & B_{propag} \\ C_{propag} & D_{propag} \end{pmatrix}$$

substituting in our values for $f_1 = 0.0822$, $f_2 = 0.1096$, and $z_3 = 0.8185$, we can propagate this all the way to the front of the cavity.

$$q_{out}(z = z_{total}) = \frac{A_{propag} q_{AOM} + B_{propag}}{C_{propag} q_{AOM} + D_{propag}} \tag{102}$$

Using Mathematica (Wolfram), the problem of finding the appropriate d (interlens distance) and z_1 (distance to the first lens) becomes that of minimizing the difference between the above expression and the complex beam parameter of the cavity: to $q_{out} = q_{cavity} = 0.229\ i$

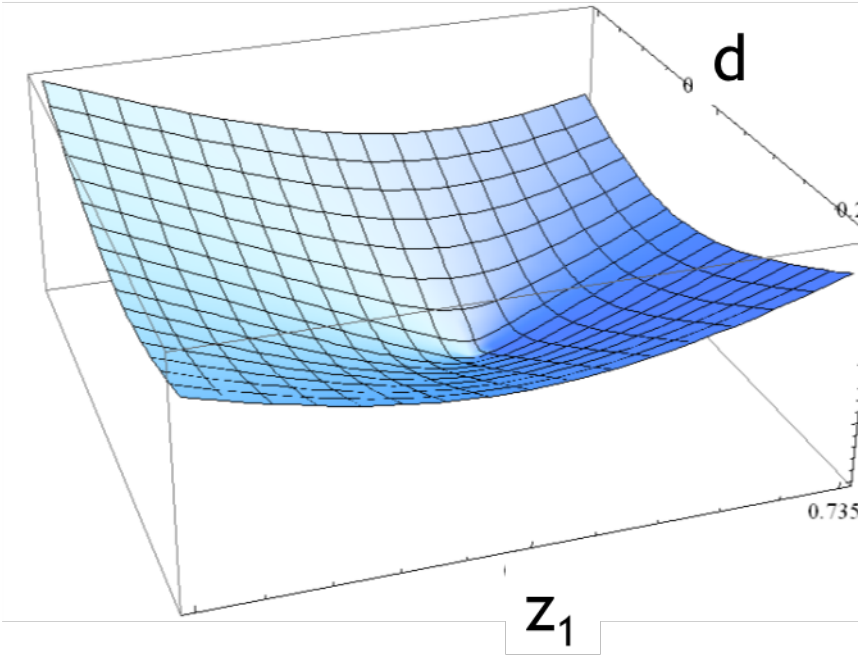

Figure 57: 2-D surface plot of deviation of q_{out} from q_{cavity} as a function of z_1 and d

The ideal values obtained were: $z_1 = 0.7388$ and $d = 0.2137$.

From this, we can construct a graph of w(z) as a function of z:

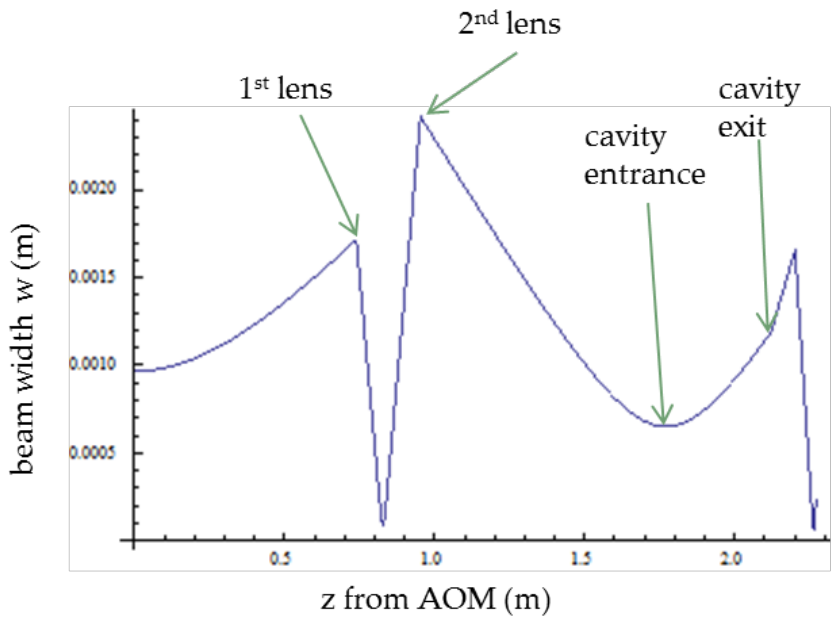

Figure 58: Evolution of beam width from laser head, through optical system + cavity, to detector

Saturated absorption

We were able to observe Lamb dips at low pressures of the 2.9ppm mixture of NO in He. To calculate the saturation parameter at 2 Torr of NO when we have 0.5 W of laser power within the cavity and the cavity approximately mode-matched so that its waist is ≈ 0.7 um, we need to know the natural lifetime, center frequency, and excited state decay time based on homogeneous broadening. From Equation 80:

$$I_S = \frac{2\pi^3 hc\Delta\nu_L^2}{A\lambda^3}$$

From Pope & Wolf[12], $b_{X1/2}$ = 4.02 MHz/Torr. Therefore at 2 Torr of pressure, $\Delta\nu_L$ = 8.03 MHz. And from HITRAN, the Einstein A for this transition is 1.48 s^{-1}. From this, we calculate I_S to be 3.69 × 10^6 W/m^2. The on axis laser intensity $I_\nu = \frac{P}{\frac{1}{2}\pi w^2}$ is 6.49× 10^5 W/m^2. This leads to a

saturation parameter of $G = \frac{I_\nu}{I_S}$ = 0.176. The absorbance α is effectively reduced by 1 + G, or an ≈ 18% dip.

Conversion of different measures of limit of detection

The limit of detection of a spectroscopic apparatus can be quantified in different ways: by lowest number of molecules detectable n_{NO}, the volume concentration of the gas measurable $\phi_{NO} = \frac{P_{NO}}{P}$, in parts per billion/trillion by volume, the minimum absorption coefficient α measurable, and the smallest percent absorption detectable:

$$1 - T = 1 - \exp(-\alpha L) \approx \alpha L \tag{103}$$

where T is the transmission. To be able to compare techniques, we must convert between the various measures. We can convert between the minimum number of molecules and the minimum volume concentration if we know the volume of the cell and the pressure at which the measurement was taken:

$$n_{NO} = \frac{N_{NO}}{N_A} = \frac{P_{NO}V}{N_A kT} = \frac{\phi_{NO}PV}{N_A kT} \tag{104}$$

where P_{NO} is the partial pressure of NO, and P the total pressure in the absorption cell.

We can convert between α_{min}, the minimum absorption coefficient detectable, and the above quantities (n_{NO} and φ_{NO}) if we know the integrated line strength S (~ 6.0×10^{-20} cm/molecule for $R(13/2)^{13}$) and the line shape of the absorption cross section σ(ν) as a function of pressure, which would allow us to determine α = Nσ/V, which is the largest at the center of the

absorption. In the low- and high-pressure limits, we can approximate σ(ν) by a Gaussian and by a Lorentzian respectively.

Since:

$$S = \int_{-\infty}^{\infty} \sigma(\nu) d\nu \tag{105}$$

then in the Gaussian Doppler-broadened limit:

$$\sigma_{max} = \sigma(\nu_0) = S\sqrt{\frac{4ln2}{\pi \Delta {\nu_D}^2}} \tag{106}$$

We can then use:

$$\alpha(\nu_0) = \frac{N_{NO}}{V}\sigma(\nu_0) = \frac{P_{NO}}{kT}\sigma(\nu_0) \tag{107}$$

At high pressures the Lorentzian form dominates, with a FWHM given by $\Gamma = A/c + 2\, b_{self}\, P_{NO} + 2\, b_{gas}\, P_{gas}$, where b_{self} and b_{gas} are the self (NO) and carrier gas pressure broadening coefficients respectively, and A the Einstein A coefficient. In this limit,

$$\sigma(\nu_0) = \frac{2S}{\pi\Gamma} = \frac{kT\alpha(\nu_0)}{P_{NO}} \tag{108}$$

We can calculate the minimum percentage absorption detectable from Equation 103. For cavity ring-down, we must use the effective path length L_{eff}, given by the distance light travels in a ring-down time constant $\tau_0 = 1/k_0$ in which the light decays to 1/e of its intensity at the start of a ring-down. For us, $L_{eff} = c\,\tau_0 = 3 \times 10^{10}$ cm/s $\times$ 4.2×10^{-6} s $= 1.26 \times 10^5$ cm = 1.26 km.

Results

Pressure Broadening

From the Introduction section, the homogeneous Lorentzian part of an absorption profile increases with increased gas pressure. This is because the increased collision rate shortens the time between the excitation of the NO molecule and either a relaxation down to the ground state, or an elastic collision that changes the phase of the molecule's wave function relative to the others in the same energy level. The simplest model is a linear dependence of the homogeneous linewidth with pressure. However there are several mechanisms[17, 18] that predict a deviation from this model at lower pressures. We fit the spectra of NO in He we measured to Voigt functions and recorded the width of the Lorentzian component as a function of pressure, using the PeakFit program:

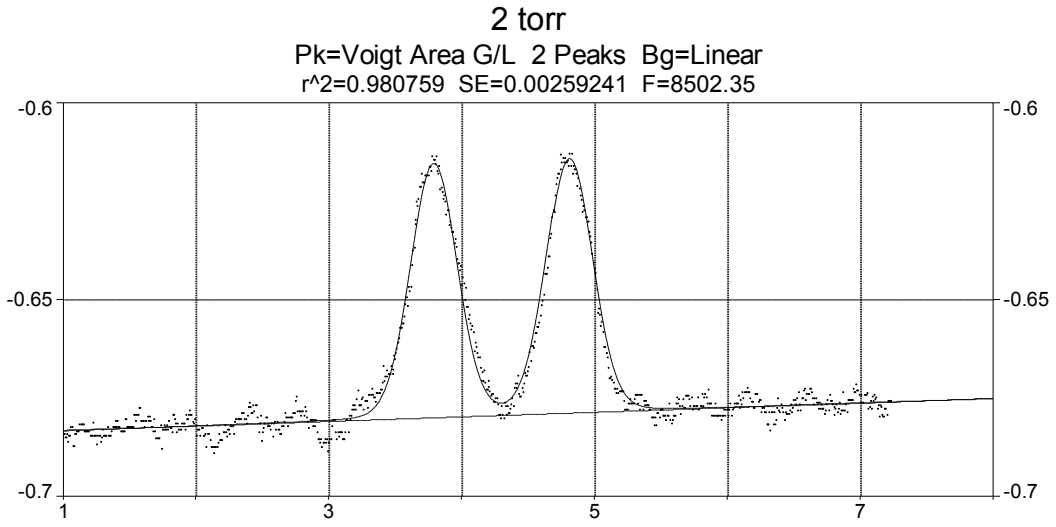

Figure 59: Fit of two Voigt peaks for spectrum from 2 Torr of 2.9ppm NO in He, R(13/2) Ω=1/2

Data was fit using the Gaussian Deconvolution method, and manually cancelling out any residual etaloning leading to a periodic baseline. Peaks were manually selected from a graphical view of the data and initial guesses for the integrated area and Gaussian / Lorentzian widths were input. The program then attempted to fit the data. For the Ω = 1/2 state we obtained the following chart, constraining the widths of the two partially-resolved peaks to be the same:

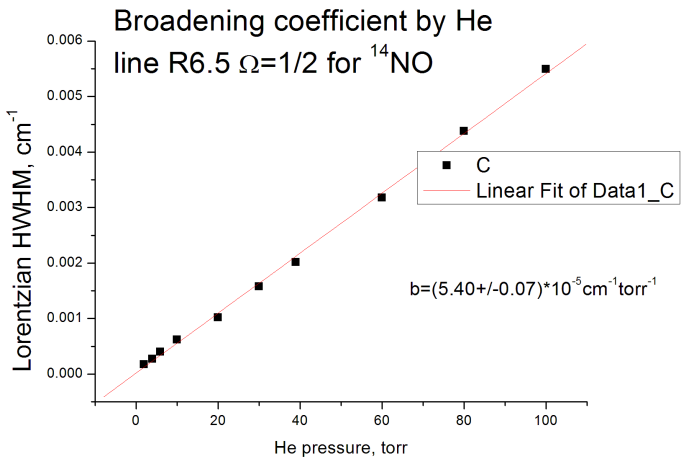

Figure 60: Pressure broadening data from plotting Lorentzian width of Voigt

It was found that the pressure broadening coefficient of He in NO for R(13/2) Ω = ½ was b = $5.40 \pm 0.07 \times 10^{-5} cm^{-1} Torr^{-1}$. We did the same for the Ω = 3/2 state:

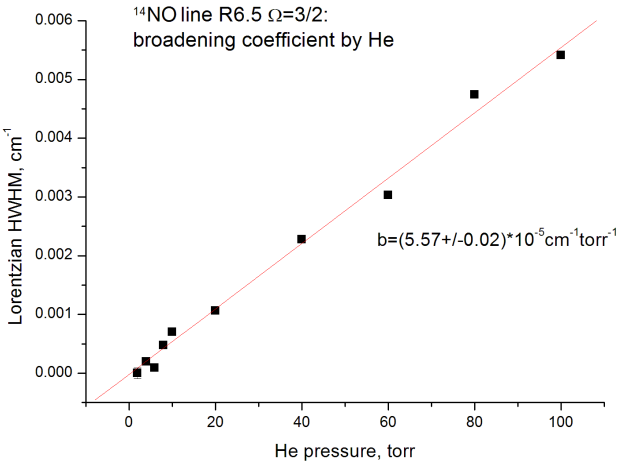

Figure 61: Ω=3/2 pressure broadening fit to data

Here we found that b = 5.57 ± 0.02 × $10^{-5}$$cm^{-1}$$Torr^{-1}$. This can be compared to values measured by Pope and Wolf[12] for the linear pressure broadening coefficient. For the Ω = 3/2 line, they found $b_{X3/2}$ = 7.3 ± 0.2 × 10^{-5} cm^{-1} $Torr^{-1}$, and for Ω = 1/2, they found $b_{X1/2}$ = 6.7 ± 0.1 × 10^{-5} cm^{-1} $Torr^{-1}$ for the HWHM.

Herriot cell limit of detection

We measured the limit of detection of NO in our Herriott cell system by looking at the minimum partial pressure of NO that would produce a SNR of 1:

We chose the transition R(J = 13/2) due to its integrated line shape, being far from the absorption lines of other atmospheric gases such as CO_2 and H_2O, and being near the peak output power of the laser:

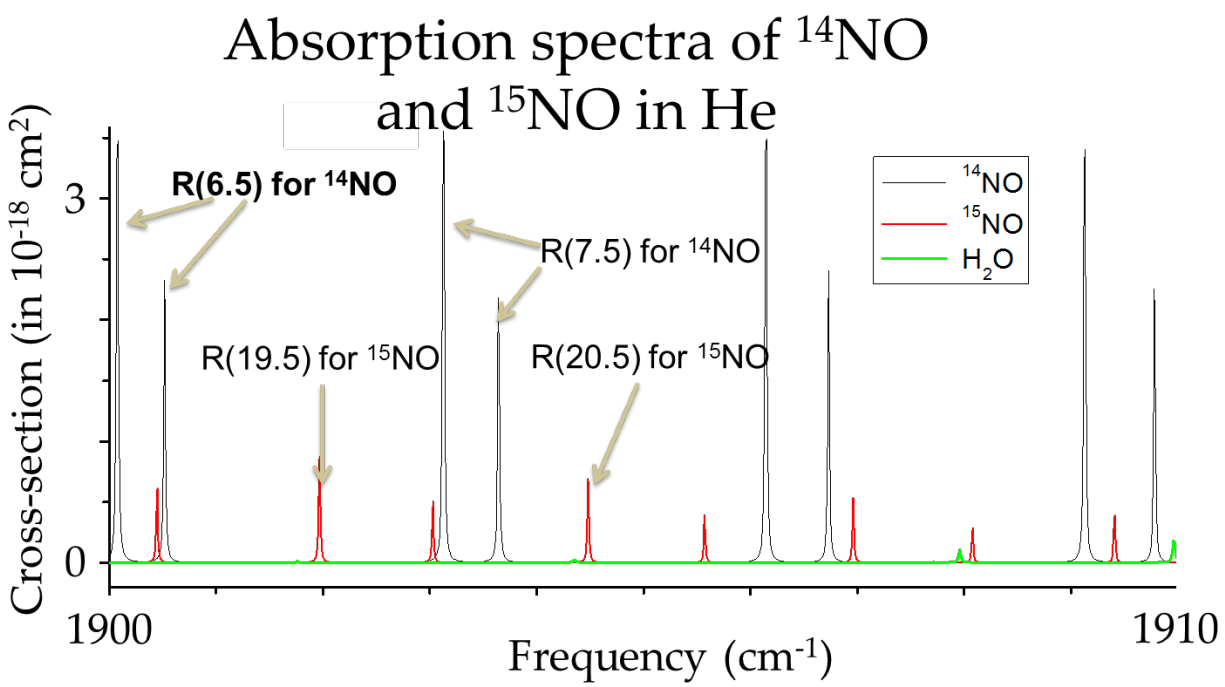

Figure 62: ^{14}NO, ^{15}NO, H_2O, and CO_2 lines in peak laser powe region, with studied lines in bold

The two R(13/2) lines (Ω = 3/2 and Ω = 1/2) are at 1900.07 and 1900.52 cm^{-1} respectively.

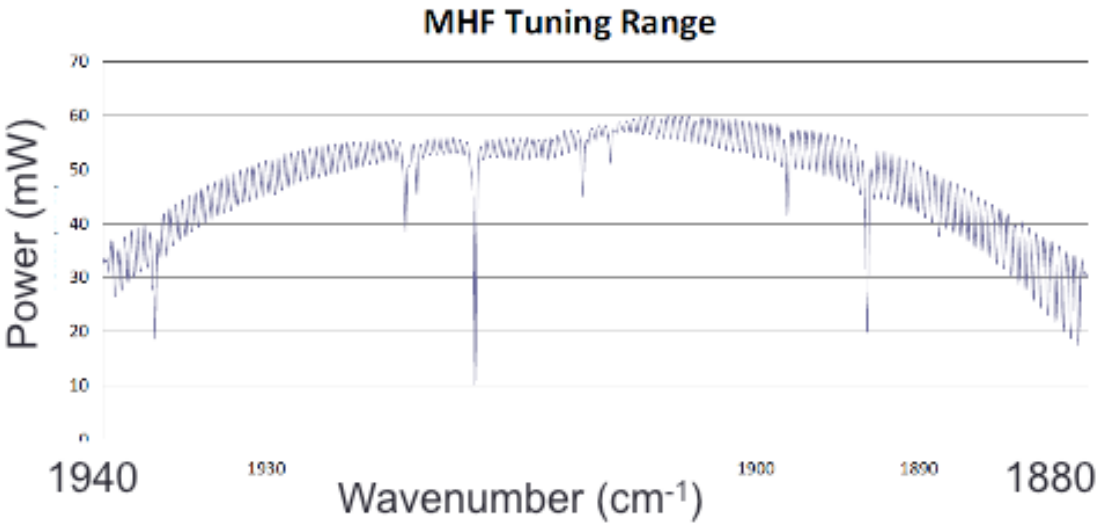

Figure 63: Output power of 21052-MHF laser, covering R branch of NO.

Above is the output power spectrum of the 21052-MHF laser. The strong dips correspond to water absorption lines, which we purposely avoided when looking for the NO ro-vibrational transition to use for detection.

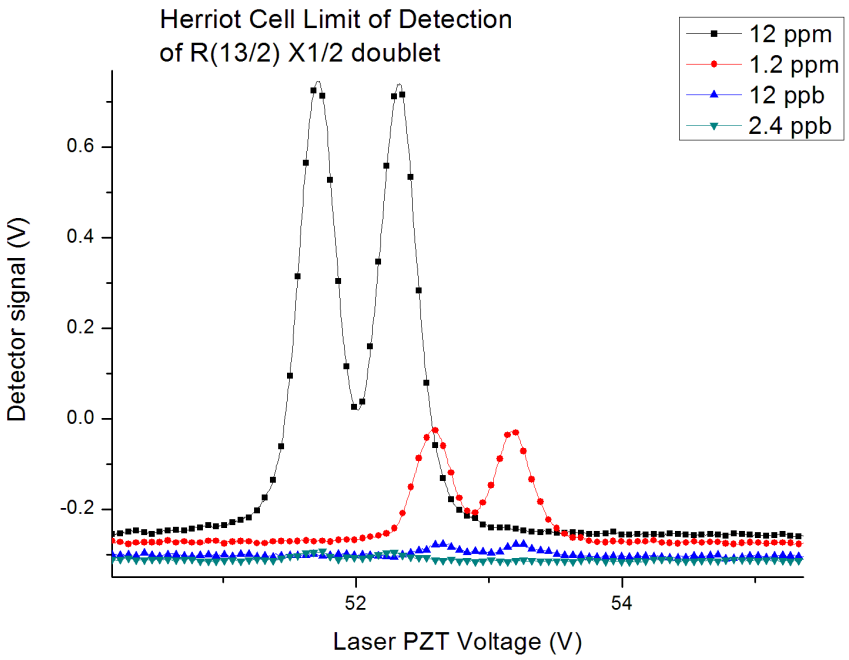

Figure 64: Limit of detection measurements with Herriot cell at 20 Torr, down to 2.4 ppb.

The preceding graph was taken at 20 Torr of the 2.9ppm mixture. We found that we could reliably measure down to a limit of detection (LOD) of 12 ppb.

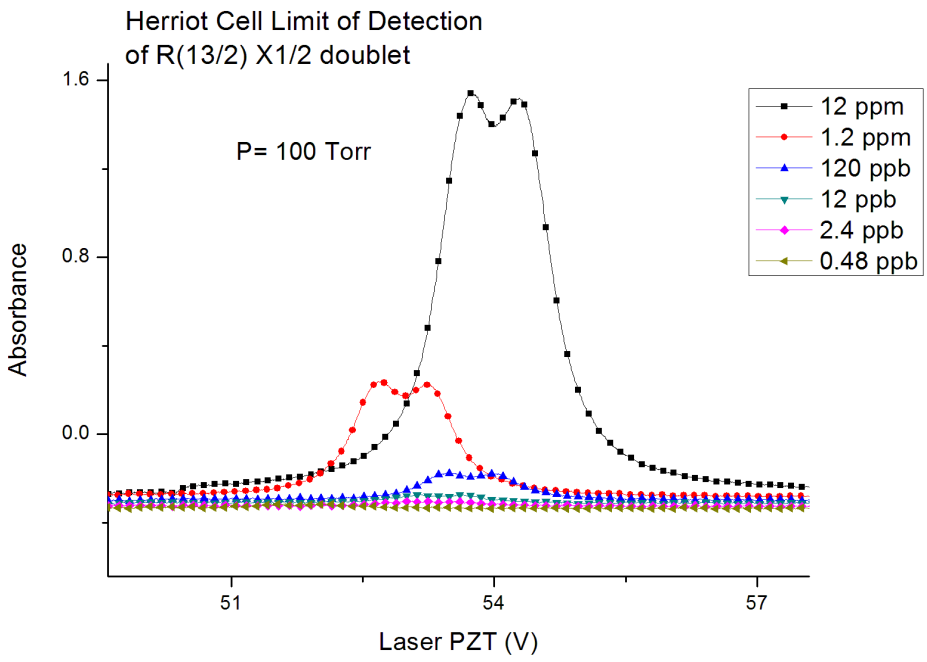

Figure 65: Limit of detection of Herriot cell at 100 Torr, down to 0.48 ppb

At 100 Torr of the mixture, we can measure down to 2.4 ppb.

Preliminary cavity results

Upon build up of the cavity signal reaching a user-set voltage threshold, the AOM is shut off, and the decay process begins. Our data acquisition program uses a non-linear least squares fit to fit in real time, either one decay at a time, or an average batch of decays. The program is set to fit after the voltage signal dips below a threshold value. Here's an example of a manually fit decay:

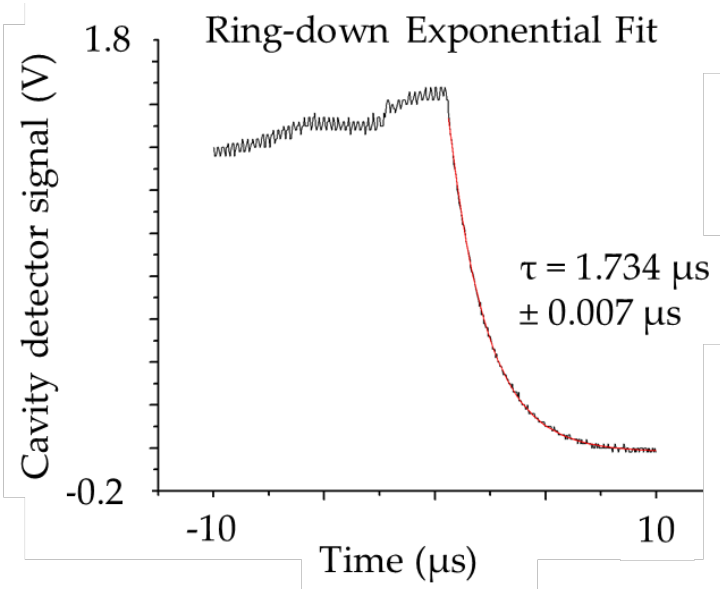

Figure 66: Cavity ring-down signal over course of 10 μs, showing buildup before decay and fit to an exponential of time constant 1.734 ± 0.007 μs.

Our earliest results involved stepping the laser PZT once a certain number of decays per step were counted:

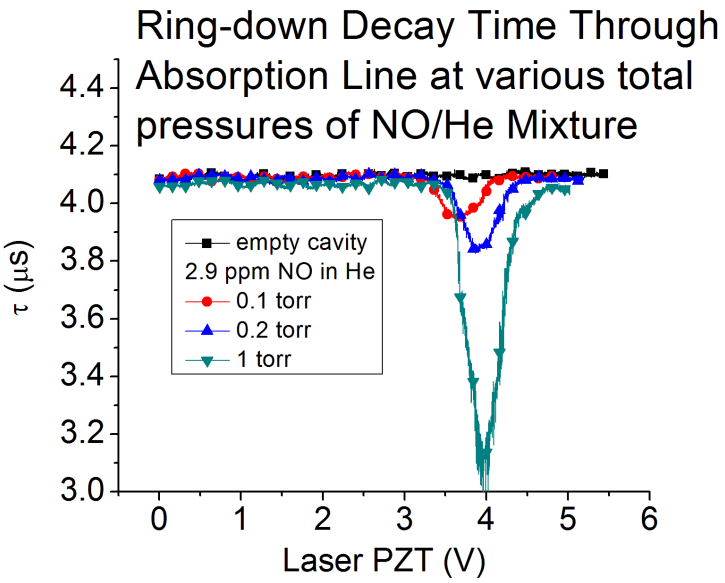

Figure 67: Dip in τ (ring-down time) due to IR absorption by NO

It was found that, when there was non-negligible absorption ($k \geq 2k_0$), the cavity would very seldomly be sufficiently excited to reach the set threshold. It was decided to lower the threshold from ≈ 3.0 V to 1.8 V for this reason.

Cavity system limit of detection

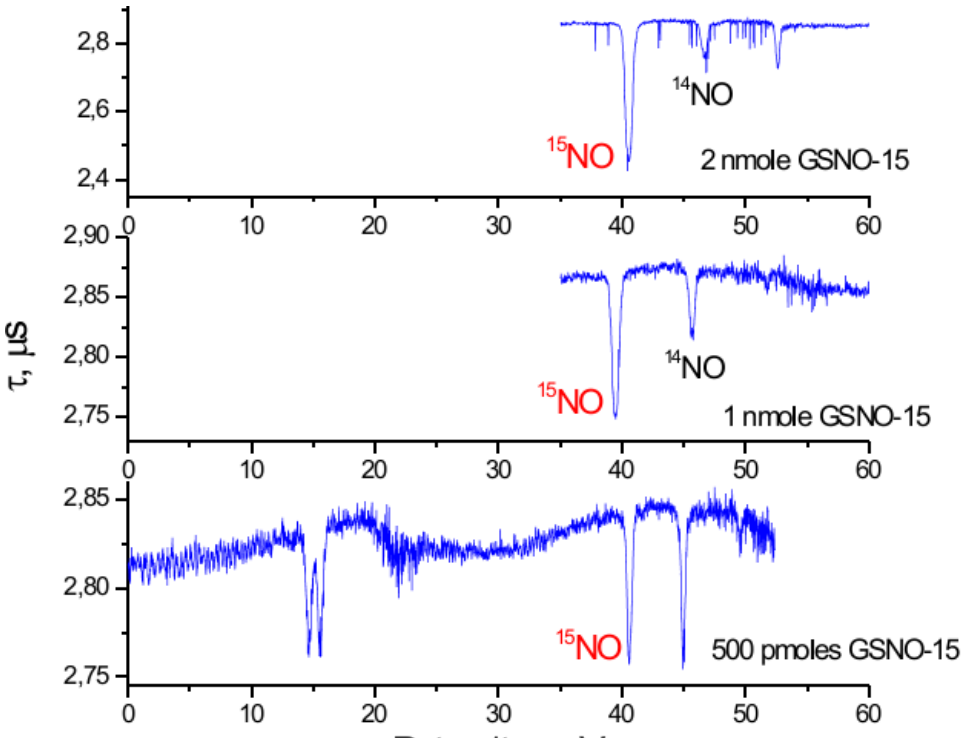

Figure 68: Limit of detection measurements of biological NO samples (GSNO)

In the graph above, GSNO samples containing both of the two major isotopes of NO (^{15}NO and ^{14}NO) were measured at increasing dilutions ratios, and it was found that we could detect sub-pmol levels of GSNO.

A more scientific estimate of the theoretical limit of detection was obtained by measuring the Allan variance of the ringdown rate k with an empty cavity, so as to avoid absorption lines affecting the measurement.

The Allan variance is a measure of the stability of a frequency measurement, such as that of an oscillator, or in our case, the decay rate k. It is defined by calculating the statistical variance of the difference between consecutive fractional deviations of measured frequency values from a reference frequency[19, 20]:

$$\sigma_y^2(\tau) = \frac{1}{2M} \sum_{i=0}^{M-1} (y(i) - y(i-1))^2 \tag{109}$$

where τ represents the time interval between points, and M represents the total number of points. y_i is the fractional deviation of frequency measurement i:

$$y(i) = \frac{\nu_i - \nu_0}{\nu_0} \tag{110}$$

where v_0 is a reference frequency, or rate, for our case, which can be the empty cavity rate k_0. We can plot the value for the Allan variance $\sigma_y^2(\tau)$ or its square root $\sigma_y(\tau)$ for different lengths of total recording time T = Mτ, and look for a time T that minimizes the Allan variance. Past this point, drift of the frequency / rate, in our case due to either cavity mode or laser frequency drift, will not allow us to decrease the statistical error in k by averaging. This tells us the ideal averaging time.

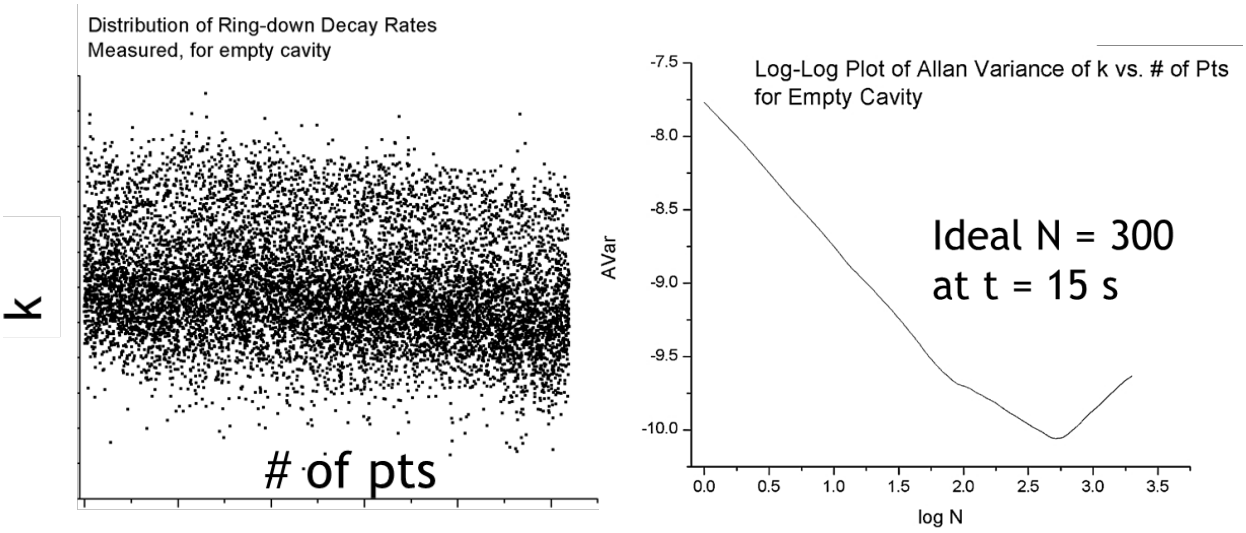

Figure 69: (Left) Raw data from measurement of k of the empty cavity. (Right) Allan variance plot of this raw data

The minimum Allan variance is ≈ 10^{-10}, which occurs after ≈ 500 points. In time, this corresponds to ≈ 15 seconds. What is more useful in terms of limit of detection is converting the Allan variance of k into the Allan variance of σ_α:

$$c\alpha(\tilde{\nu}) = k(\tilde{\nu}) - k_0 \qquad (111)$$
$$\sigma_\alpha = \frac{\sigma_k}{c}$$

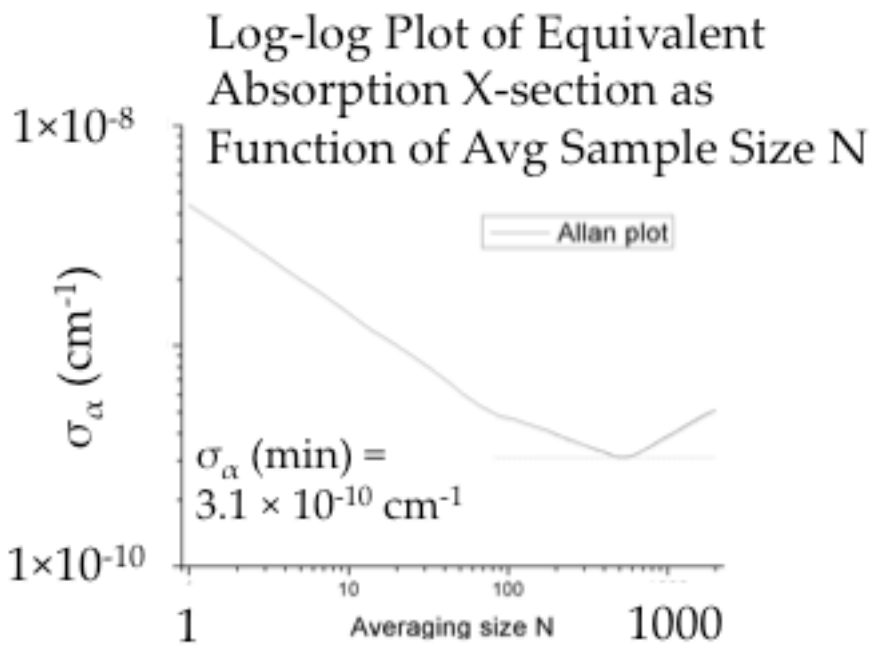

Figure 70: Allan variance plot, converted to units for σ_α (error in absorption coefficient α)

Given a volume of 710 mL, a $\sigma_\alpha = 3.1\times10^{-10}$ cm^{-1}, corresponds to 0.028 pmol or the equivalent of 73 pptv of NO in He with a total pressure of 10 torr.

^{15}NO measurements

Our setup is also capable of measuring the isotopologue of NO with nitrogen-15. The physics, with the exception of nuclear spin effects, is generally the same, but with a different reduced mass μ.

The reduced mass of ^{14}NO is:

$$\mu = \frac{m_N \cdot m_O}{m_N + m_O} \tag{112}$$

with $m_N \approx 14.00$ $m_O \approx 15.99$, $\mu \approx 7.467$ amu.

The reduced mass of ^{15}NO has $m_N \approx 15$ amu, which causes $\mu \approx 7.742$ amu, or 3.6% larger.

Because the fundamental vibrational frequency ω_0 is proportional to $\sqrt{\frac{k}{\mu}}$, the vibrational frequency of ^{15}NO is roughly 3.6%/2 = 1.8% smaller and thus shifted to the red, as seen in the its fundamental ro-vibrational spectrum below:

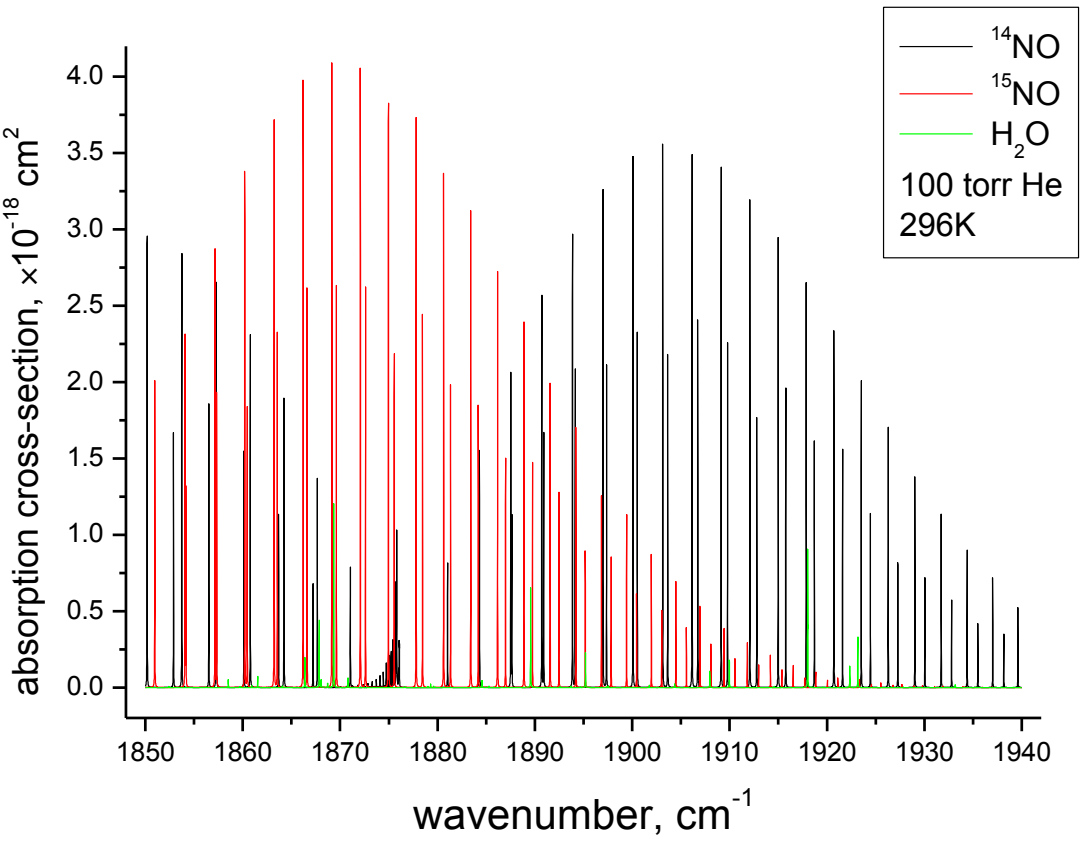

Figure 71: ^{15}NO spectrum superimposed on ^{14}NO [13]

With the Herriot cell, we were able to measure absorption of ^{15}NO down to 0.68 ppm, looking at the R(37/2) Ω = ½ transition:

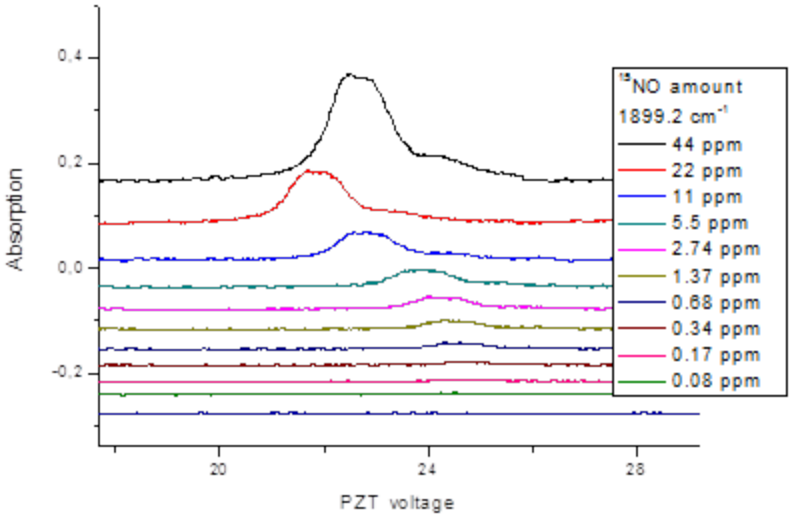

Figure 72: Measurement of quantities of ^{15}NO in the reference cell.

With the cavity, we could measure down to the ≈ 100 pmol level of GSNO-15.

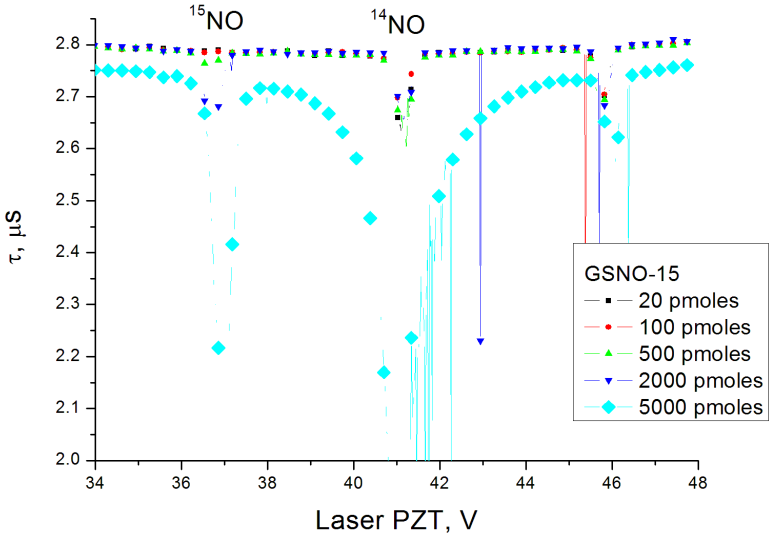

Figure 73: Limit of detection measurements of ^{15}NO with CRDS.

In addition, we measured ^{15}NO's pressure broadening coefficient for R(37/2) Ω=1/2 by using the same method for ^{14}NO:

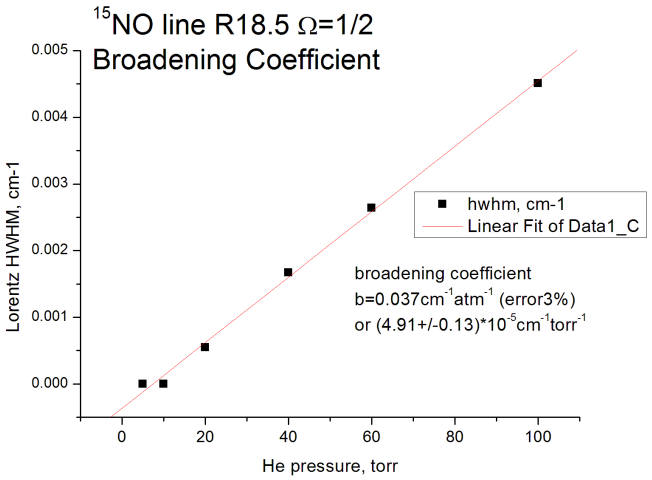

Figure 74: Pressure broadening measurement for ^{15}NO transition

The value obtained for the pressure broadening measurement was b = 4.91 ± 0.15 × 10^{-5} cm^{-1} $Torr^{-1}$.

Lamb dip observations

We observed Lamb dips in the partially-resolved R(13/2), Ω = 1/2 doublet, but not in the R(13/2), Ω = 3/2 unresolved doublet, possibly because of the large number of cross-over sub-

Doppler resonances obscuring the Lamb dip.

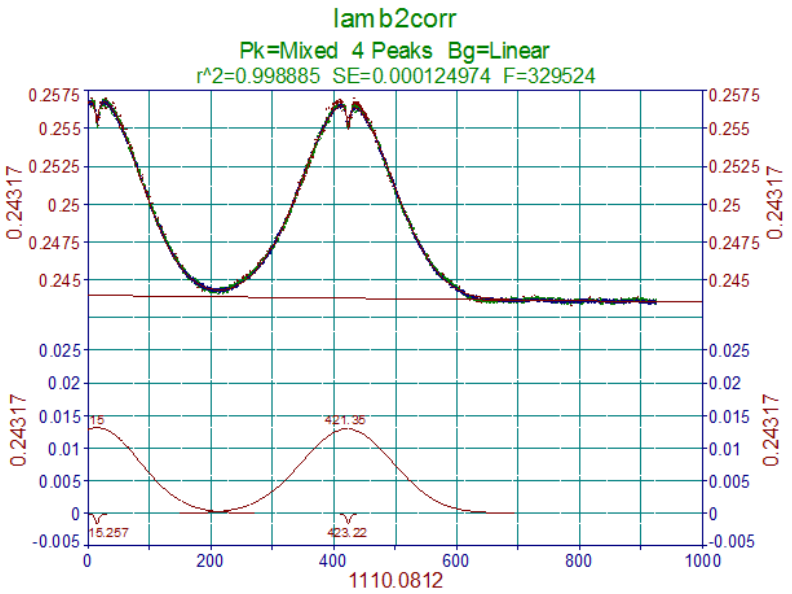

Figure 75: Fitting of absorption with a Lamb dip. Lower graph shows both the Voigt/Gaussian envelope and the Lorentzian Lamb dip

Like with the unsaturated pressure-broadening measurements, the position, width, and amplitude Doppler-broadened peaks were placed manually and fit by the program. This time, however, Lorentzians were also placed at the center of the two peaks and fit. The above graph was taken at P = 0.268 Torr. However, the expected linear relation between the pressure and the fitted Lorentzian width was not observed. We theorize that this may be due to the increased standard deviation of decay rates near the top of the Doppler-broadened peak:

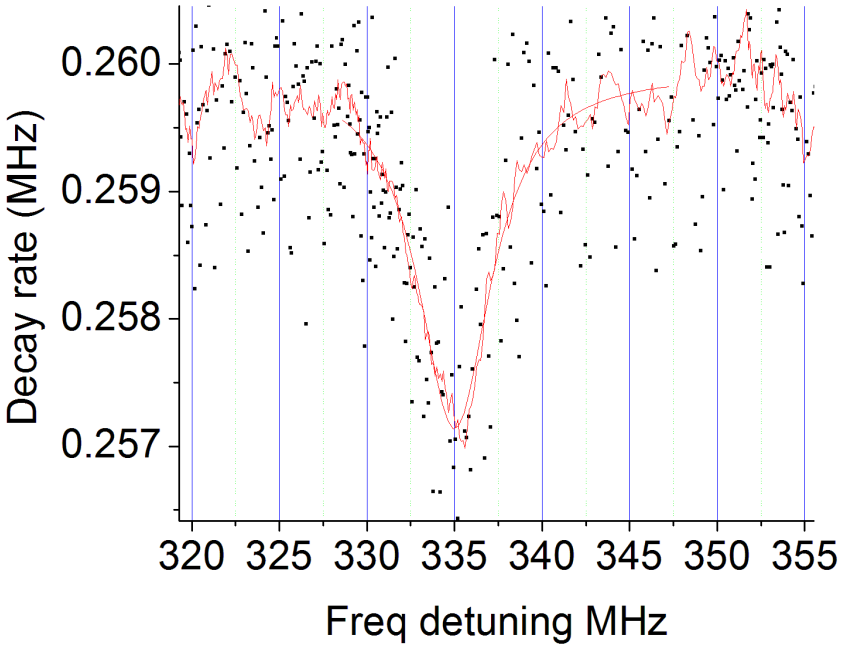

Figure 76: Fit of Lamb dip to Lorentzian, showing large statistical deviations in k.

This occurs because saturated absorption at the center of the Doppler-broadened line causes the decay rate of light in the cavity to be smaller the concentration of NO would suggest, until the light intensity in the cavity drops to much below the saturation parameter G, when the decay of the signal approaches the exponential decay model[21].

Evidence for this comes from the residuals of the non-linear least squares fit of the ringdown decay signal as a function of time:

a.) at the center of the peak

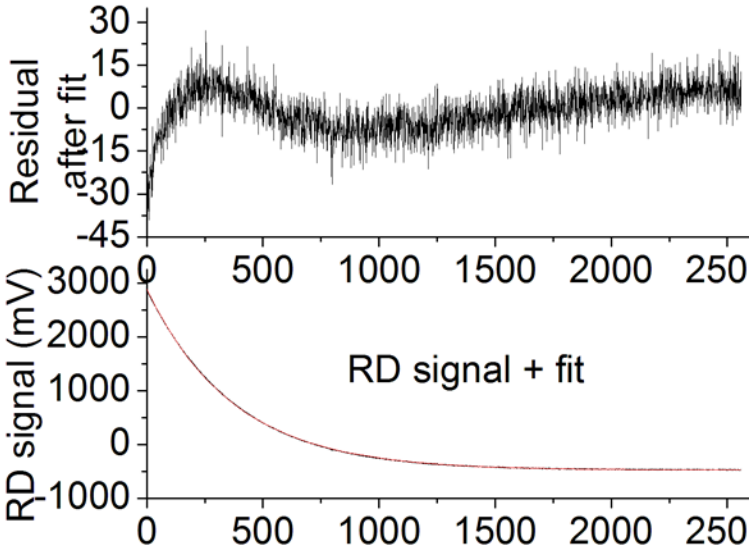

Figure 77: Residuals of an exponential fit to the ring-down decay signal, within a Lamb dip

and b.) off the peak:

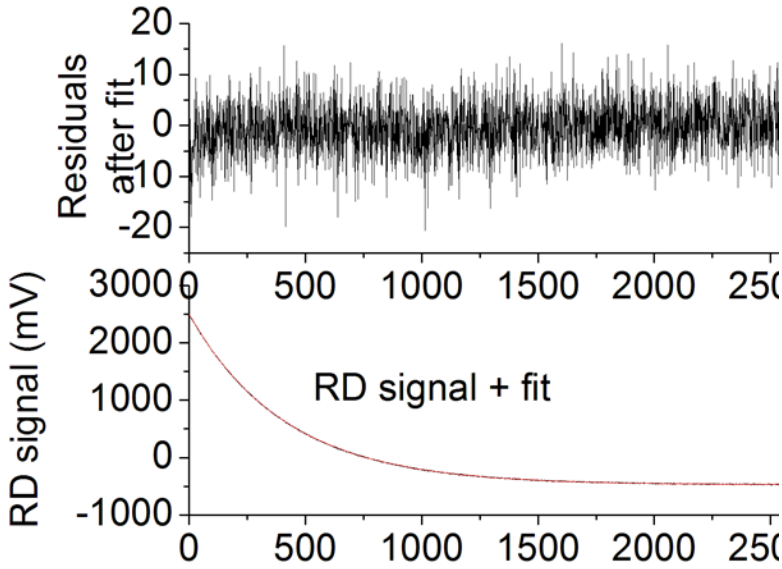

Figure 78: Residual of exponential fit to ring-down decay signal off resonance

where the residuals show deviation from the exponential fit. Note that the vertical scale for the residuals in Figure 76 is ≈ 55% larger than that for Figure 77.

Epilogue

Difficulties: NO "sticking"

A very significant problem we had was the desorption of NO from the walls of its containing cell.

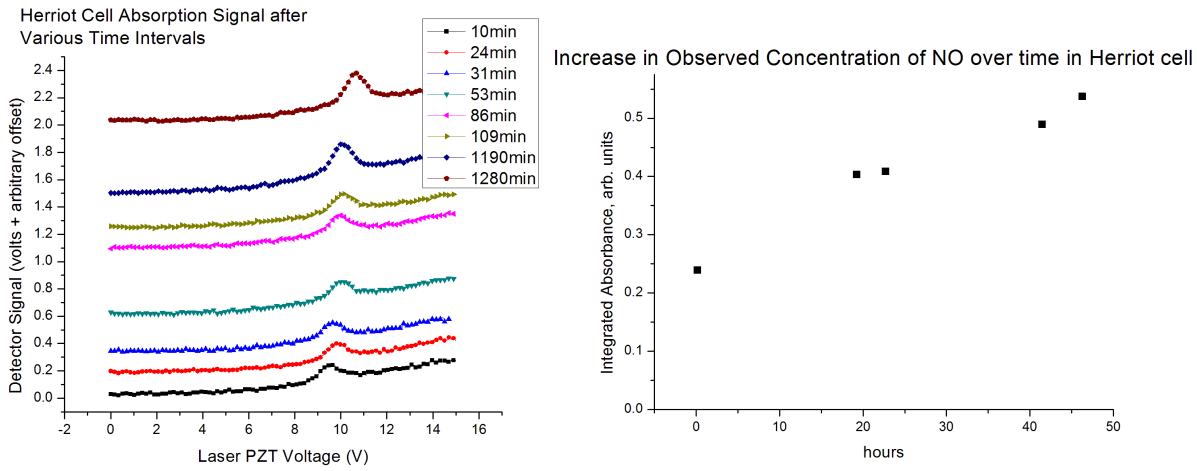

Figure 79: Increase in absorption of NO over time within Herriot cell

The continued presence of desorption led us to install the flow system so that we could control the concentration of NO as a function of time.

Difficulties: Mid-IR optics

The frequency region in which most diatomic fundamental vibrational transitions are located is the mid-infrared region between 3 µm and 10 µm. The fundamental ro-vibrational spectrum of NO for J < 10 lies between ≈ 1880 to 1920 cm^{-1}. There are a number of difficulties in this region:

a.) Common glasses such as BK7 and fused silica are opaque. This requires using less common, and more expensive optics such as CaF_2, BaF_2, MgF_2. Aluminum oxide glass (sapphire) begins absorbing in this region, and many optics materials for the mid-IR, such as Si, Ge, and CdTe, are opaque in the visible light region, making it more difficult to align optics with a co-propagating visible beam such as a HeNe laser.

b.) Certain photodiodes do not work in this region, such as InGaAs, PbS. The two most commonly used detectors are HgCdTe (MCT) and InSb.

c.) $LiNbO_3$ (lithium niobate), one of the most valuable non-linear crystals in the mid-IR, does not work past 5 um, making it more difficult to create doubling, difference, and sum frequencies, waveguides, acousto-optical switching / modulation and OPOs.

Conclusions

We determined that it is indeed possible to measure sub-picomole levels of NO, and were successful in detecting both isotopologues. We attempted to duplicate and improve on the work of Pope and Wolf but did not get results congruent with theirs, i.e. within errors of measurement. We were able to detect Lamb dips but they were difficult to characterize and fit due to the non-exponential nature of ring-down decays at the Lamb dips. Feedback to the laser was a greater problem than we expected and we had to try several methods to limit them, including using a combination of an EOM and a polarizer, and then a Faraday isolator. Nitric oxide sticking to the walls of the cavity forced us to introduce a flow system to handle low pressures of small NO samples. It was also found that water needed to be purged from the

cavity to prevent damage to coatings, requiring us to adopt a cold trap and molecular sieve. The cavity's alignment was difficult due to the cavity's low finesse for the copropagating HeNe light.

Comparison of limit of detection with other spectroscopic methods

From Allan variance analysis, we can theoretically measure a minimum α of 3.1×10^{-10} cm^{-1} after 30 s of averaging, or equivalently, 1.7×10^{-9} cm^{-1} after 1 s. We can compare these numbers to other spectroscopic methods using the calculations from the Conversion of different methods of Limit of Detections section.

Using a volume of 710 mL, the integrated line strength of $S = 6.0 \times 10^{-20}$ cm / molecule, and a Doppler width of 128 MHz = 0.0043 cm^{-1} we can calculate that our theoretical limit of detection is 0.15 pmol. This corresponds to 730 pptv of NO in He at a total pressure of 1 Torr.

For conventional laser spectroscopy, McManus, et al.[22] measured a theoretical minimum of 30 pptv in 30 s with a physical length of 0.315 m and total optical path length of L = 69 m Herriot cell of volume 0.5 L, with a minimum α of 2×10^{-10} cm^{-1} using the same transition R(13/2) as us. This is equivalent to 164 pptv in 1 s. This was measured at 40 Torr of NO in air. At 1 Torr, 164 pptv is equivalent to a minimum amount of 7.0 pmol.

For quartz enhanced photo acoustic spectroscopy, 4.9 ppbv was achieved in 1 s by Dong, et al.[23] With a laser power of 66 mW, measuring at a pressure of 210 Torr, and a cell composed of two tubes of diameter 0.084 cm and length, 0.39 cm (i.e. a volume of 17.3 µL) we obtain a value of 2.4×10^{-4} pmol, or at 1 Torr, 0.050 pmol.

For Faraday Modulation spectroscopy, Lewicki et al.[24], using a cell length of 50 cm and diameter 0.8 cm, an integration time of 1 s, obtained a limit of 0.38 ppbv at 40 Torr. This corresponds to 0.083 pmol, or equivalently at 1 Torr, 3.32 pmol.

Future experiments

A model for saturated cavity ringdown (SCAR) decay rates was developed by the Giusfredi group.[21] It should be used to measure absorbance at the center of the Gaussian peak, and to measure the dependence of the width of the homogeneous sub-Doppler peak on the pressure of the gas. A new cavity made of glass or other material that limits the sticking of NO to the cavity walls would help reduce error at low concentrations of sample in the cavity. The fact that feedback from the cavity and other optical elements back through the AOM destabilizes the laser can be investigated to determine what can minimize or control such instability.

Appendix A: Detection of S-Nitroso compounds using mid-IR cavity ringdown spectroscopy

The research conducted by our group led to the following publication[25]:

Detection of S-nitrosocompounds using mid-IR cavity ringdown spectroscopy

*Vitali I. Stsiapura,[1] Vincent K. Shuali,[1,2] Benjamin M. Gaston,[3] Kevin K. Lehmann[1]**

[1]Chemistry Department, University of Virginia, Charlottesville, VA 22904; [2]Physics Department, University of Virginia, Charlottesville, VA 22904; [3]Department of Pediatrics, Case Western Reserve University School of Medicine, Cleveland, OH 44106

AUTHOR EMAIL ADDRESS lehmann@virginia.edu

Corresponding author: Kevin K. Lehmann, Chemistry Department, University of Virginia, Charlottesville, VA 22904. phone: 434-243-2130, fax: 434-924-3710, email: lehmann@virginia.edu

ABSTRACT. S-nitrosocompounds have received much attention in biological research. In addition to their role as nitric oxide donors, there is a growing evidence that these compounds are involved in signaling processes in biological systems. Determination of S-nitrosylated proteins is of great importance for fundamental biological research and medical applications. The most common method to assay biological S-nitrosocompounds is to chemically or photochemically reduce SNO- functional groups to release nitric oxide that is then entrained in an inert gas stream and detected, usually through chemiluminescence. We report a method of S-nitrosocompounds detection using cavity ring-down measurements of gaseous NO absorbance at 5.2μ. The proposed method, in contrast to the chemiluminescence-based approach, can be used to

distinguish isotopic forms of NO. We demonstrated sensitivity down to ~2 pmole of S-^{14}NO groups and ~5 pmole of S-^{15}NO groups for S-nitrosocompounds in aqueous solutions. The wide dynamic range of cavity ring-down detection allows the measurement of S-nitrosocompounds levels from pico- to nanomole amounts.

The biological role of nitric oxide (NO) addition to heme groups in soluble guanylyl cyclase (sGC) and in hemoglobin has been well-understood for nearly two decades.[1,2] Addition of NO to thiols is now appreciated to be an important signaling reaction – termed S-Nitrosylation – that is analogous to phosphorylation, glutathionylation, palmitoylation, acetylation and other physiological protein modifications.[1-6] There are many examples demonstrating that this type of signaling occurs in a broad range of biological systems.[7-14] Moreover, disorders of protein S-nitrosylation are relevant to the pathophysiology of many diseases,[1,3-5,14-22] and S-nitrosylation is emerging as a field relevant to many biological disciplines.[23]

In cell and organ systems, S-nitrosoproteins level is normally in the range of ~2 pmole/mg protein[24], and unfortunately these levels are very close to the limit of sensitivity for most assay systems.[25] Moreover, even indirect methods of S-nitrosoproteins detection relying on measurements of nitric oxide liberated after chemical or photochemical cleavage of S-NO bond have insufficient sensitivities restricting researcher to work mainly with cell lysates.

The most sensitive assays for S-nitrosylated proteins are based mainly on chemiluminescent detection of NO[26,27] formed after the reduction of S-nitrosocompounds.[25,28-33] Current state-of-the-art chemiluminescence instruments (for instance, Eco Physics CLD 88) can detect nitric oxide down to a 0.05 ppb level This technique is based on gas-phase reaction of NO with O_3 giving rise to NO_2* in the excited state, which is responsible for luminescence.[34,35] However, chemiluminescence intensity is changed in the presence of other gases (for example, water, O_2,

CO_2, etc.) that quench luminescence of NO_2* [36] and therefore this approach has strict requirements for gas mixture content and purity which may be difficult to satisfy during measurements of biological samples. Chemiluminescence cannot be used to distinguish isotopic forms of NO and thus cannot be used in isotopic labeling experiments. Poor stability of S-nitrosocompounds and difficulties with selective reduction of SNO-groups lead to typical assay sensitivity of ~ 1-5 pmole[4,25,31,37] while the limit of NO_2^- detection was reported to be ~0.12 pmole.[38] Similar sensitivity for nitrite detection was demonstrated recently[39] using GC/MS method. However, studies of S-nitrosylation signaling in biological systems require better sensitivity; the absence of reliable and sensitive methods of S-nitrosocompounds detection in biological samples hampers research progress in this field.[25]

Nitric oxide has strong ro-vibrational spectrum absorbance lines in the mid-IR range near 5.2 μm (Fig. 1) and we believe that optical techniques based on absorbance measurements of NO in the gas phase have the potential to achieve improved sensitivity and accuracy in S-nitrosocompounds detection. A number of approaches for the optical sensing of trace NO – absorption spectroscopy using multipass cells,[40] cavity-enhanced methods,[38,41-43] photoacoustic, Faraday rotation[44] spectroscopies – have been reviewed recently.[45]

It is important to note that sensitive detection of the absolute amount of NO (but not the NO concentration) is what we are interested in.

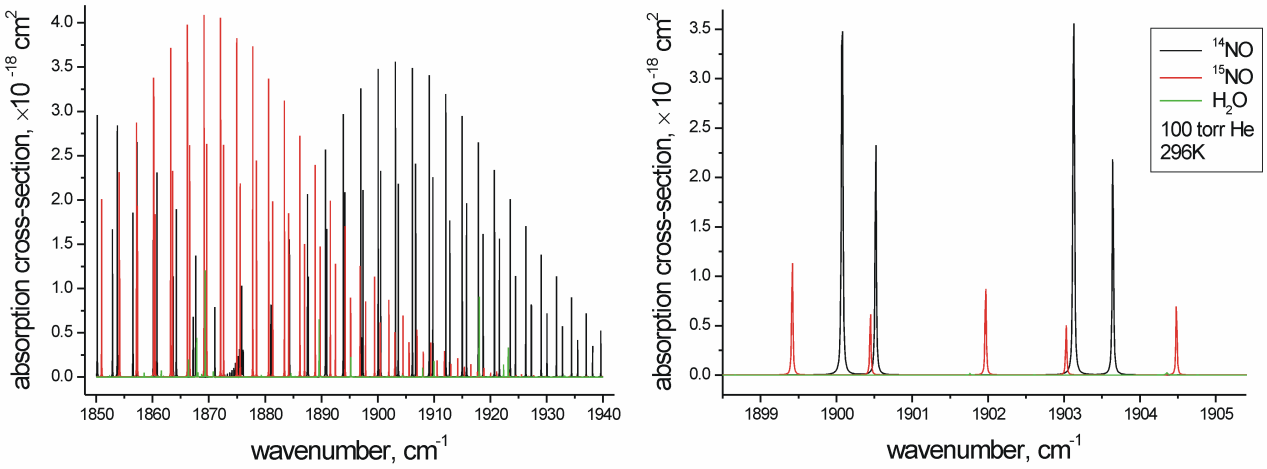

Figure 1. Simulation of absorption spectra for NO isotopologues and H_2O in helium (100 torr) using the data from the HITRAN-database.[46] Different wavenumber ranges are shown

Cavity ring-down spectroscopy (CRDS) has been demonstrated to be a powerful method of trace gas detection with ultra high sensitivity and specificity.[47] The CRDS technique determines the optical absorption of a sample contained inside a low-loss optical cavity from an increase in the decay ("ringdown") rate of light leaking through the cavity as it travels between highly reflective mirrors (reflectivity R > 99.9%). Use of low loss and thus high finesse cavities allows an increase in the effective pathlength of light in the sample to up to several kilometers. Additionally, intensity fluctuations of the light source do not influence measurement accuracy since changes in the decay lifetime of light in the ring-down cavity (rather than changes in light intensity) are detected. Likewise, analyte absorption outside of the sample volume does not contribute to the observed concentration. The first CRDS measurements used pulsed light sources with broad spectral width,[48,49] but another version that utilizes tunable continuous-wave (cw) lasers – cw-CRDS – allows one to realize greater stability in the shot-to-shot fluctuations of

the cavity decay rate and this translates into improved sensitivity.[50,51] In favorable cases, parts per trillion by volume (pptv) level[52,53] sensitivity has been demonstrated.

Use of cw-CRDS to detect nitric oxide in the mid-IR range were reported previously. Kosterev et al. [41] demonstrated NO detection at parts per billion by volume (ppbv) concentrations with a 0.7-ppbv standard error for 8 s integration time using a cw distributed feedback quantum cascade (QC-DFB) laser. Murtz et al. [42,54] reported use of a CO sideband laser for ultrasensitive detection of NO isotopologues with sensitivity down to 2×10^{-10} $cm^{-1}Hz^{1/2}$ and demonstrated its application in human breath analysis,[43] with a reported noise equivalent detection limit of 7 pptv of ^{15}NO with 70 sec of integration time. In this work, we report similar detection limits but using a laser system that is more robust and portable. The developed method allows the detection of isotopologues of S-nitrosocompounds with sensitivities (3σ) ~1.5 pmole $S^{14}NO$ and ~5 pmole $S^{15}NO$ groups.

Methods and instrumentation

Figure 2 shows a schematic of our cw-CRD spectrometer that is used to detect trace NO gas released after reduction of SNO- functional groups. A cw, water-cooled, external cavity quantum cascade laser (Daylight Solutions, 21052-MHF) operating at 5.2 μm is used as the excitation source. It has a specified mode hop free tuning range of 1880-1940 cm^{-1} with output power higher than 30 mW throughout this range (~60 mW at 1905 cm^{-1}). The laser can be scanned and coarse-tuned over the entire spectral range using the supplied laser controller, which drives a stepping motor that controls the intracavity grating. Fine-tuning of the laser frequency (~1 cm^{-1}) was implemented by applying voltage (up to 100 V) to a piezoelectric transducer (PZT) that moves the same grating.

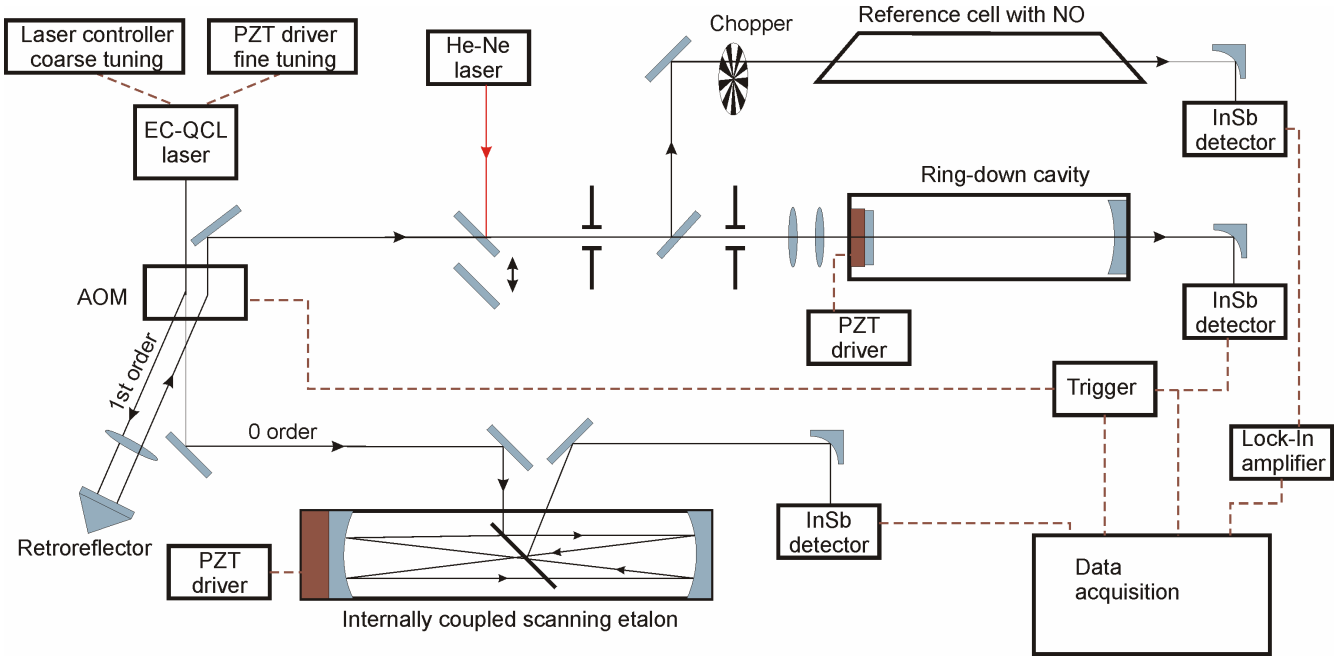

Figure 2. Principal scheme of cw-CRDS instrument for ultrasensitive detection of S-nitrosocompounds. EC-QCL – external cavity quantum cascade laser, PZT- piezoelectric transducer, AOM- acousto-optical modulator

The laser beam is sent to an acousto-optic modulator (AOM) (Gooch&Housego, R37040-3-5.4) in a double-pass configuration which is used to shut off the laser light on a trigger pulse generated after sufficient intensity builds up inside the ring-down cavity. The pulse also initiates each measurement of the cavity loss rate. The AOM is driven by a 40 MHz RF oscillator (NeOS / Gooch & Housego) and the first order diffracted beam (diffraction efficiency d_{eff} = 0.69) after two passes through the AOM is sent to the ring-down cavity. We have measured that the first order beam diffracted through the AOM is attenuated with 1/e decay time of ~150 ns when the control voltage to the RF driver is switched off. One challenge in cw-CRDS with a linear cavity is that light reflected from the front mirror of the cavity (which is usually most of the incident light) can travel back to the laser, leading to frequency instabilities due to optical feedback. The

AOM imposes a frequency shift (80 MHz in double pass configuration) on the first order diffracted beam that is doubled for the light that returns from the cavity to the laser, making the returned beam effectively incoherent compared to light in the laser. In addition, the reflected beam intensity was attenuated by a factor of d_{eff}^4 by the AOM on one round trip. Despite this, we observed evidence of the back reflection of the cavity pulling the laser frequency if RF power corresponding to maximum diffraction efficiency is applied to the AOM, but this can be effectively eliminated by attenuation of RF power going to the AOM by 4-5 dB which decreases d_{eff}. Two uncoated CaF_2 lenses with focal lengths 10 and 7.5 cm were used as a telescope for matching the transverse beam profile of the input laser to the fundamental transverse mode (TEM_{00}) of the ringdown cavity.

A HeNe laser and a pyroelectric beam profiling camera Pyrocam (Spiricon) were used to facilitate aligning of the spectrometer optical components.

The cavity is mounted inside a vacuum-tight cell with CaF_2 windows. The ringdown cell is home-made (Fig. S1) and consists of two stainless steel kinematic mirror mounts attached to flexible hoses (275×275-R-MH4, LDS Vacuum shopper) and reducing cross (275×NW16-RWX, LDS Vacuum shopper) using 2.75″ Conflat connections. NW16 flanges of the reducing cross were used as inlet and outlet gas ports of the ringdown cavity. The mirror mounts are mounted on a super-invar plate to reduce thermal drift of the cavity. The high-finesse (F~10000) linear optical cavity is formed by a pair of wedged ZnSe supermirrors, one flat and the other concave with a 0.5 m radius of curvature. The mirrors were custom coated by LohnStar with a specified R=99.975% at 5.2 μm on one side and an AR coating on the backside. Measurements of a ringdown time for an evacuated cavity showed that actual reflectivity of the mirrors at 1900.50 cm^{-1} is equal to 99.972% and mirror transmission T= 0.020% was also measured. The mirrors are

separated by ~35 cm. Scanning the NO absorption spectrum while monitoring the cavity transmission allowed us to determine a cavity free spectral range (FSR) of 427.6 MHz with 0.2% accuracy. The transverse mode spacing was calculated as 135 MHz and the TEM_{00} mode has a calculated beam waist radius of ω_0 = 0.69 mm at 1900 cm^{-1}. The internal diameter of the cell is ~3 cm and was designed to allow switching from a linear cavity to a 3 mirror "V" shaped cavity or a 4 mirror ring cavity for the purpose of reducing destabilizing feedback to the laser head (Fig. S1). In order to minimize adsorption of nitric oxide onto the cavity cell walls, metal surfaces were coated with an inert layer of SilcoNert 2000 (SilcoTek).

To ensure laser light would couple into the TEM_{00} cavity mode, the position of the plane mirror and therefore cavity length were changed by applying a sine-wave voltage in parallel to three PZTs (AE0505D08F, Thorlabs) attached to the mirror mount using function generator (HP3312A, Agilent) and piezo driver (P-863, Physik Instrumente). The amplitude of the mirror motion was selected to scan slightly over FSR of the ringdown cavity, ensuring that at least one TEM_{00} mode will pass through resonance with the laser on each half cycle of the modulation. The frequency of the cavity length modulation was in the range 20-40 Hz, well below mechanical resonance conditions seen above 80 Hz. This is also sufficiently slow to ensure the cavity excitation reaches steady-state.

The IR radiation transmitted through the cavity was focused, using an off axis parabolic mirror, and detected with a fast (rise time < 100 ns) liquid nitrogen-cooled InSb detector (KISDP-0.5-FJ/GE, Kolmar) with photosensitive area S= 0.5 mm^2. The detector signal was amplified by a matched DC to 20 MHz transimpedance preamplifier (Kolmar).

When the detector signal exceeds a specific threshold level (typically +1.5 V) a trigger pulse is generated by a pulse generator (DG535, Stanford Research Systems) and this is used to switch-

off the AOM for 40 μs (approx. 10 times the ringdown time) and to initiate acquisition of the ringdown signal by a 100MHz 14-bit USB oscilloscope (HS5-530XM, Tiepie, Netherlands). A 12-bit digitizer board (PCI-DAS4020/12, Measurement Computing) was used to monitor pressure and record signals from etalon and reference cell detectors. Software for instrument control, data processing and analysis is developed using Delphi 7.0 programming language. Levenberg-Marquardt algorithm[55,56] was used for non-linear least squares fitting of experimental data to exponential model.[57,58]

It was found that the fine-tuning system of the laser frequency using the PZT attached to external cavity grating has a non-linear dependence of detuning vs. applied voltage (Fig. S2, see Support Information) and absolute value calibration of wavenumber scale is needed.

A scanning internally-coupled Fabry-Perot etalon with finesse F~21, similar to one described earlier,[59] was developed for this purpose using 2 spherical gold mirrors (radius of curvature 50 mm) in a confocal configuration for ease of alignment and mode spacing. One of its mirrors was attached to PZT and ramped by a Burleigh PZT driver (model #RC-43) at 50 Hz. A special circuit box (Wavelength Monitor, designed by W.S. Woodward for the group of R.E. Miller) was used to track the PZT voltage where the maximum etalon transmission signal occurred which was used to monitor the laser frequency position within one etalon FSR at millisecond timescale. Non-linearity of the mirror displacement on PZT voltage of the etalon was corrected by calibration with a HeNe laser. The etalon FSR of 749.3 MHz was measured using the frequencies of ^{14}NO Q-branch lines from HITRAN database.[46,60]

In addition, a reference gas cell filled with ~200 mTorr ^{14}NO (or ^{15}NO) was used for calibration of the spectrometer frequency scale and for locking of laser frequency to an absorption line of nitric oxide. To increase accuracy of gas cell transmission measurements, the

light intensity was modulated by a chopper with f=200 Hz and a lock-in amplifier (SR-510, Stanford Research Systems) was used to demodulate the signal.

Locking of the laser frequency to the ^{14}NO $R_{3/2}(6.5)$ transition line at 1900.5 cm^{-1} and the ^{15}NO $R_{3/2}(18.5)$ line at 1900.4 cm^{-1} was achieved using a 1f modulation technique. Laser frequency was modulated by 14 MHz peak-to-peak by applying a 100 Hz sinusoidal voltage to the laser PZT. The lock-in output signal was read by a 12-bit digitizer and used for stabilization of the laser frequency on the absorbance line by changing the DC voltage offset on the laser PZT. We found that laser frequency was reliably locked to NO line transition within ±2 MHz at millisecond time scale.

Figure 3 shows a schematic of the gas sampling system for S-nitrosocompound detection. S-nitrosocompounds solution is injected through the septum port into the sample chamber and UV irradiation or chemical reaction with Cu(I)/Cys are used to cleave S-NO bond and release nitric oxide gas, whose concentration is measured by the CRDS-instrument. Carrier gas with a constant flow controlled by a mass-flow controller (5850E, MKS) is bubbled through the sample solution and facilitated NO diffusion to the ringdown cavity. Temperature of the glass cold trap was maintained at ~195K (with a cryogenic bath of dry ice and ethanol) to remove water vapor. The ringdown cell pressure was regulated by a needle valve between the cell and pump and was monitored using a 100 torr capacitance pressure gauge (MKS). The total volume of the sample chamber, connecting tubings, cold trap, and the cavity was determined to be ~730 ml. Residency time for a molecule is proportional to pressure inside the cavity. For a 116 sccm (standard cm^3 per minute) He flow and 20 torr cavity pressure, a residence time τ_{res}~ 9.2 s was determined. Higher flow rates of the carrier gas did not provide good mixing with NO and uniform distribution of gas mixture in the cavity.

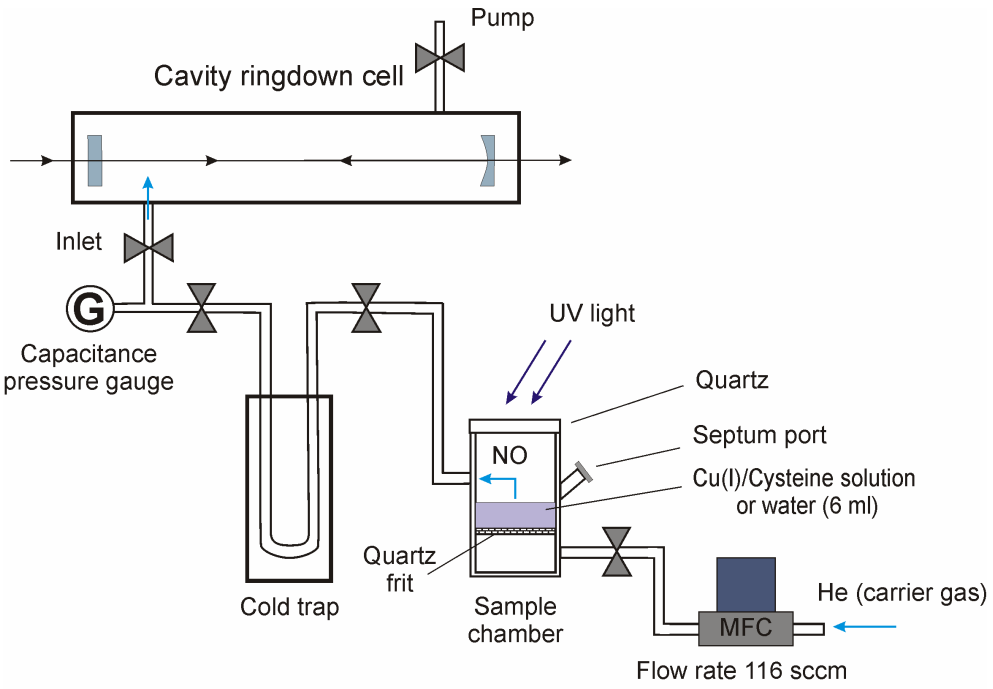

Figure 3. Schematic of gas sampling system. MFC – mass flow controller

Samples preparation

Glutathione (GSH), L-cysteine, copper (I) chloride, $NaNO_2$, $Na^{15}NO_2$, N-(1-naphthyl)ethylenediamine dihydrochloride (NED), sulfanilamide, $HgCl_2$, KI, bovine serum albumin (BSA) were purchased from Sigma-Aldrich. Sulfuric acid was from Mallinckrodt Chemicals (USA). Nitric oxide (>99.5%) was purchased from GTS-Welco (USA). Aqueous solutions were freshly prepared using milliQ water.

^{14}N, ^{15}N- labeled S-nitrosoglutatione (GSNO) were prepared by acid-catalyzed nitrosation of GSH according to the method described previously.[61] GSNO concentration were measured spectrophotometrically using molar extinction coefficient 922 $M^{-1}cm^{-1}$ at 335 nm.[61,62]

S-nitrosoalbumin was synthesized according to the method reported earlier[63] without preliminary reduction of disulfide bonds. SNO-groups content in the protein was determined using the Saville assay.[64] The copper/cysteine solution for SNO-groups reduction was prepared as described earlier.[65]

^{15}NO was synthesized by reduction of $Na^{15}NO_2$ in acidic conditions. Briefly, a 120 ml screw-cap septum bottle (23230-U, Supelco) was connected to two cold traps in series maintained at 196 K and 77 K respectively and evacuated using a mechanical pump. 0.4 ml 0.2 M $Na^{15}NO_2$, 1 ml 0.2 M KI, and 1 ml of concentrated H_2SO_4 were injected through the septum to the glass bottle under evacuation. Water vapor and residual NO_2 were intercepted by the first cold trap, while ^{15}NO was condensed in the trap maintained at 77K.

Results and discussion

We examined measurement statistics of the CRDS-spectrometer and estimated experimentally achievable limit of detection for NO concentration based on noise level and temporal stability of ringdown times for the empty cavity. Allan deviation (a criterion first developed to quantify stability of clocks and oscillators[66]) of absorption coefficient (σ_α) was used to identify the optimal measurement time that can be utilized for data averaging, i.e. integration over this period leads to increase of signal-to-noise ratio. Figure 4a shows that for an optimum averaging time of 200 s the minimum detectable absorption coefficient (1σ) was 3.7×10^{-10} cm^{-1}. This corresponds to a minimal detectable concentration 5×10^{7} cm^{-3} of ^{14}NO molecules in helium at 20 torr (77 pptv) or ~0.06 pmole ^{14}NO inside the cavity with 730 ml volume. Ringdown time τ_0~ 4.2 μs (Fig.4b) in absence of NO indicates that the effective pathlength of light travelling between the cavity mirrors is ~1.2 km.

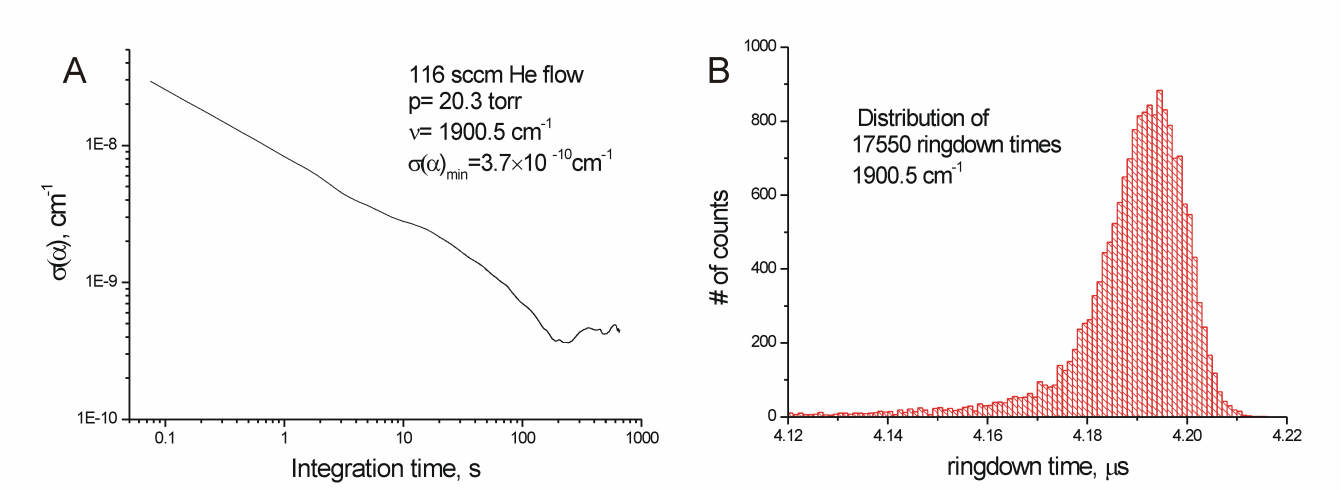

Figure 4. A) Allan deviation plot of absorbance coefficient at 1900.5cm^{-1} vs time in absence of NO. Flow of He (116 sccm) was established through the ringdown cavity at 20.3 torr pressure. Minimum detectable absorption coefficient of 3.7×10^{-10} cm^{-1} can be reached in ~200 s integration time. B) Distribution of the ringdown times is shown.

We considered two approaches to quantify the amount of NO released from S-nitrosothiols.

Our initial approach was to evacuate the ring-down cavity and sample chamber, isolate them from pump, and initiate NO release from the sample by chemical or photochemical reaction and to fill the ring-down cavity. To ensure uniform distribution of NO in the cavity, cold trap, and sample chamber a short pulse of He carrier gas was injected which facilitated transport of NO and increased total pressure (normally up to 2-5 torr). Then measurements of NO in gas phase were carried out using the cavity ring-down technique. This approach potentially allows simultaneous measurement of absolute concentration of ^{14}NO and ^{15}NO from the same sample and, from the known volume of gas sampling system (730 ml), one can determine the absolute amount of reduced SNO-groups. It also would minimize the dilution of the generated NO in the

carrier gas and also allow measurements to be averaged to achieve whatever signal to noise ratio is required, down to a minimum determined by long term drift in the instrument baseline.

Unfortunately, we have found that this technique does not provide reproducible results of S-nitrosothiols concentration due to significant (~3 times) and non-controlled losses of NO (Fig.5). We believe that the losses are mainly related to sticking of NO to the surfaces of the cavity and gas sampling system. Extensive literature on nitric oxide absorption on metal surfaces can be found elsewhere [67-69]. Slow desorption of NO isotopologues adsorbed onto the cavity walls were observed in the isolated and preliminary evacuated ringdown cavity (Fig. S3). Passivation of the cavity metal parts with a chemically inert SilcoNert coating did not eliminate the problem with the losses.

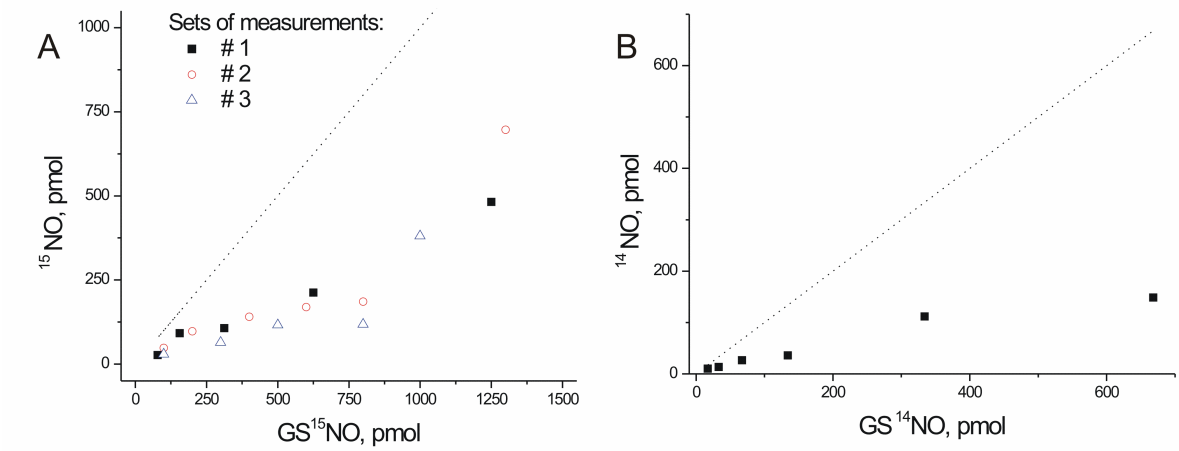

Figure 5. Detected amount of ^{15}NO (A) and ^{14}NO (B) released from corresponding N-labeled GSNO in reaction with chemical reducer (Cu(I)/Cys assay). Dotted line shows predicted amount of NO isotopologues based on GSNO concentration.

More encouragingly, we found that we can reproducibly measure NO concentration when a constant flow of calibrated gas mixture (0.725 ppm ^{14}NO in He) was established through the cavity (Fig.6). The limit of detection obtained by monitoring the ^{14}NO $R_{1/2}(6.5)$ transition at 1900.5 cm^{-1} was determined to be 4×10^{9} cm^{-3} (at ~0.2 s integration time), that corresponded to ~ 5 pmoles of nitric oxide in 0.73 L volume (Fig.6). The negative value of linear fit intercept shifted from zero by more than 3σ may indicate manifestation of saturation effects of optical transition at low pressures.

Therefore, we found that only measurements in flow mode could provide reliable quantitative information of NO concentration and this approach was implemented for S-nitrosothiols detection.

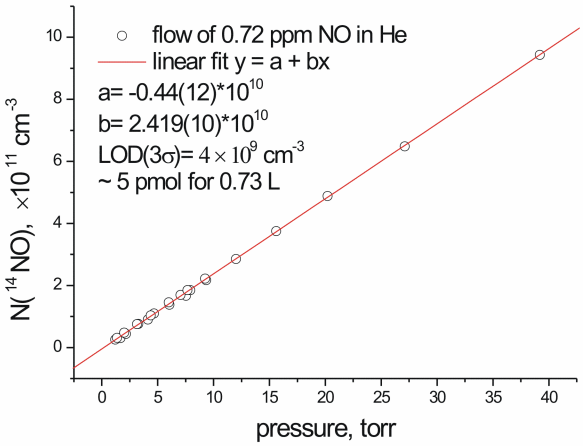

Figure 6. Plot of experimental concentration of ^{14}NO for different pressures of 0.72 ppm NO in He measured in a flow mode. Constant flow of 17 sccm was established through the cavity. Limit of detection is 4×10^{9} cm^{-3} or ~5 pmole of ^{14}NO for 0.73 L volume.

Detection of NO and S-nitrosothiols in flow mode

For these measurements, a constant flow of carrier gas was established through the sample chamber and the optical cavity; steady-state pressure inside the cavity was adjusted using the needle valve (Fig. 3). Laser frequency was locked to the maximum of NO absorbance line. For ^{14}N-labeled NO and SNO-group containing compounds detection the $R_{3/2}(6.5)$ transition of ^{14}NO located at 1900.5 cm^{-1} was used. Changes of the cavity ring-down time were monitored in time after sample injection through the septum into the sample chamber.

Change in ringdown decay rate $k=1/\tau$ is proportional to concentration N(t) of NO molecules in the cavity

$$k(t) = 1/\tau(t) = cN(t)\sigma_p + k_0, \quad (1)$$

where c- speed of light, σ_p – absorption cross-section of NO in helium at center of the transition at pressure p, and k_0 – the empty cavity loss rate which is determined before NO measurement. The pressure broadening coefficient of NO line by helium is needed for σ_p calculation when pressure broadening makes a significant contribution to the lineshape. The measured pressure broadening coefficient of lorentzian half-width at half-medium for ^{14}NO $R_{3/2}(6.5)$ transition $b=6.9\times10^{-5}$ $cm^{-1}torr^{-1}$ was in good agreement with the data reported earlier.[70]

One can estimate optimal pressure of carrier gas to maximize sensitivity of CRDS measurements in the flow mode. Signal-to-noise ratio is proportional to $\sigma_p\sqrt{N_m}$, where N_m – number of measurements to be averaged. N_m is proportional to the residence time τ_{res} of a molecule inside the ringdown cavity, which for constant gas flow has a linear dependence on pressure (Fig. S4). Therefore, the signal-to-noise ratio will have the following dependence

$$S/N \sim \sigma_p \cdot \sqrt{p} \quad (2)$$

Taking into account that the pressure broadening coefficient for ^{14}NO $R_{3/2}(6.5)$ transition one can find that optimal pressure for the flow mode measurements will be ~20 torr (Fig. S5).

Reproducibility of repeated injections (100 μl) of ^{14}NO using a gas-tight syringe is shown in Fig.7. Peaks were fitted using Exponentially Modified Gaussians (convolution of Gaussian with exponential)

$$EMG(t) = \frac{Area}{\sigma\sqrt{2\pi}} \exp\left(-\frac{(t-t_0)^2}{2\sigma^2} \right) \otimes \tau^0 \exp(-t/\tau^0), \quad (3)$$

where τ^0 corresponded to the residence time of NO molecules inside the cavity (Fig. S6). We found that for the constant flow of 116 sccm through the gas sampling system of 0.73 L at 20 torr pressure the residence time was ~9.2 s.

A relative error of 2% in the determination of the peak area was observed and indicated that measurement-related uncertainty was comparable to precision of sample volume injection using the syringe (specified as ~1%).

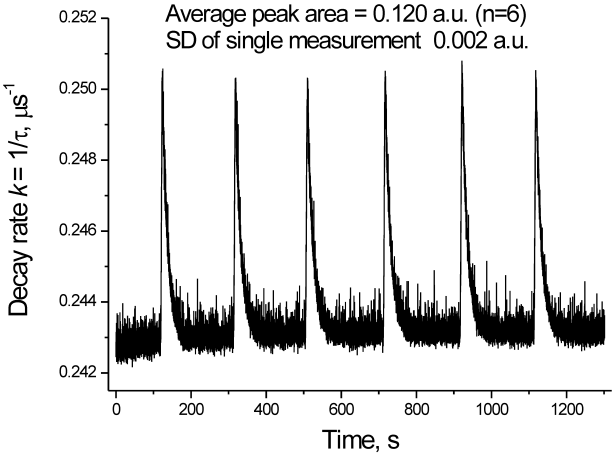

Figure 7. Reproducibility of 100 μl injections of the same ^{14}NO amount measured using the flow mode. Variability in areas of the peaks does not exceed 2 %. Carrier gas flow 116 sccm, pressure 30 torr. SD- standard deviation.

Measurements of S-nitrosothiols were carried out in a similar way but with the SNO-group reducing solution of Cu(I)/Cys (~5 ml) placed in the sample chamber before the injections. After injecting small amounts of GSNO, where the timescale of the NO release reaction was less than ~1 s, the shape of the peaks observed could be fairly described using EMG function (3) with residence time ~9-10 s. For higher amounts of injected S-nitrosocompounds the shape was distorted due to finite time of SNO-groups reduction and it was fitted to a linear combination of EMG functions.

Calibration curves for ^{14}N-labeled S-nitrosocompounds detection using Cu(I)/Cysteine assay are shown in Fig.8. We estimated an uncertainty in the concentration of prepared standards to be $\varepsilon \leq 5\%$ and corresponding weight factors were assigned to data points. Figure 8a shows good linearity for a wide dynamic range (more than 2 orders of magnitude) of $GS^{14}NO$ amounts with the limit of detection (3σ) ~1.5 pmoles. A similar limit of detection ~2 pmole was found for BSA-$S^{14}NO$ (Fig. 8b). The presence of protein introduced some problems during the measurements due to foaming of the solution in the sample chamber as carrier gas bubbled through it. However addition of antifoam compound to the solution helped to minimize this effect.

Analogous dependence for $GS^{15}NO$ (Fig.9) shows a slightly worse sensitivity of ~5.4 pmole which is explained by ~4 times difference in line strengths of ^{14}NO and ^{15}NO transitions in this range.

We demonstrated that cavity ring-down spectroscopy method of S-nitrosocompounds detection in aqueous solutions has similar sensitivity as state-of-the-art reduction-chemiluminescence technique and, additionally, allows to distinguish $^{14}N/^{15}N$-labeled S-nitrosocompounds. It is noteworthy that utmost sensitivity of the proposed method is determined by quality of the supermirrors of the ringdown cavity. Because of the importance of this emerging field to medicine and experimental biology, assays with imporved sensitivity can be predicted to be important for diagnosis and monitoring of a wide range of biological fluids, including blood, urine, cerebrospinal fluid, bronchoalveolar lavage fluid.

In distinction to chemiluminescent method the developed technique relies on absorbance measurements of nitric oxide within its rovibrational spectrum. In order to ensure specificity of NO detection the absorbance line used for laser frequency locking and detection should not overlap with absorption lines of any volatile impurities that may be present in biological mixtures (mostly water and CO_2). This condition can be easily implemented because of narrow widths of molecular absorption lines in gas phase at low pressures, and the ^{14}NO $R_{3/2}(6.5)$ transition line at 1900.5 cm^{-1} and the ^{15}NO $R_{3/2}(18.5)$ line at 1900.4 cm^{-1} have been selected for detection that are located far from water or CO_2 absorbance lines.

Other possible sources of artefacts that may affect reliability and performance of CRDS technique are: 1) pressure instability in the ringdown cavity during the sample injection (however, these cases can be easily identified by monitoring pressure during the measurements) and 2) presence of volatile compounds (for example ethanol) in high amounts (more than 1 mL) in the sample chamber. In the latter case the volatile compound vapor entrained by carrier gas may not be completely intercepted by the cold trap at -80°C and can condense and produce aerosole in the cavity resulting in broad-band optical losses due to scattering. Effect of broad-

band optical losses can be mitigated by periodic measurements of ringdown time "on" and "off" the absorbance peak at some cost in sensitivity, however occurrence of this situation is very unlikely since sample injection volume normally does not exceed 100 μl.

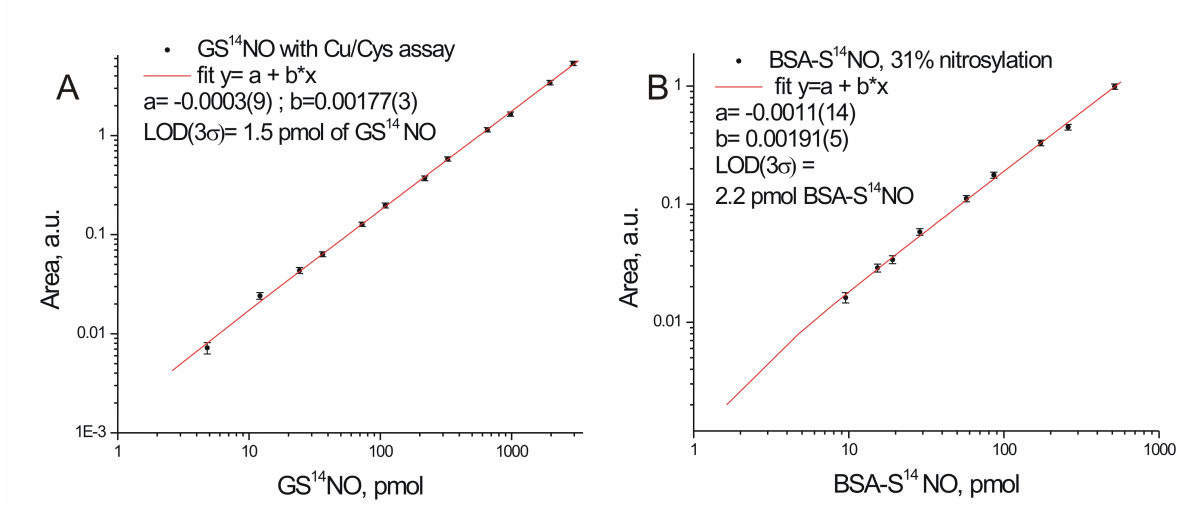

Figure 8. Limit of $GS^{14}NO$ (A) and BSA-$S^{14}NO$ (B) detection using CRDS-technique. Carrier gas flow 116 sccm, pressure – 20 torr.

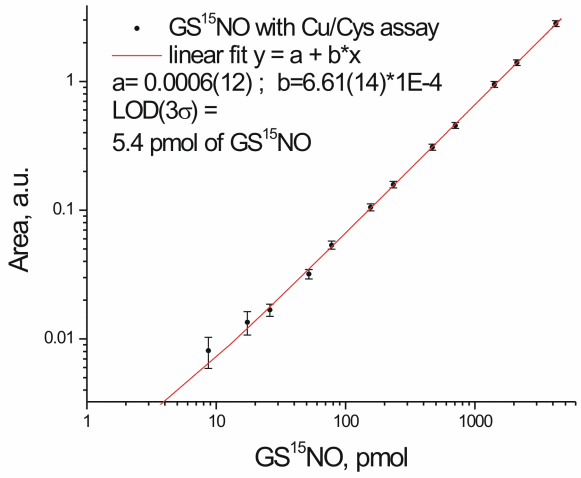

Figure 9. Limit of $GS^{15}NO$ detection using CRDS technique. Carrier gas flow 116 sccm, pressure – 20 torr. Laser was locked to the ^{15}NO transition at 1899.4 cm^{-1}.

Conclusions

Here we report a cw-CRD spectrometer for S-nitrosocompounds detection with limits of detection ~2 pmole for S-^{14}NO and ~5 pmole for S-^{15}NO groups of proteins. We have found that quantitative measurements are possible only in a flow mode. The dynamic range of S-nitrosothiols measurements reaches 3 orders of magnitude and extends from pico- to nanomoles. The advantages of the proposed method to assay S-nitrosylated proteins are: 1) high sensitivity and large dynamic range; 2) ability to detect and metabolically track ^{15}N-labeled S-nitrosothiols in cells and organisms.

We believe that making use of long integration time available for averaging and increasing data acquisition rate will result in sensitivity improvement of the CRDS-spectrometer.

ACKNOWLEDGMENTS. We would like to thank IDBR program, NSF and NIH for funding this research. VIS would like to acknowledge BRFFI (grant #M13MC-020) for partial support.

Supporting Information Available. Schematics of the ringdown cavity, desorption kinetics of NO from the walls of the isolated cavity, and some characteristics of the spectrometer (dependence of laser frequency on PZT voltage, residence time measurements for constant flow, etc.). This material is available free of charge via the Internet at http://pubs.acs.org.

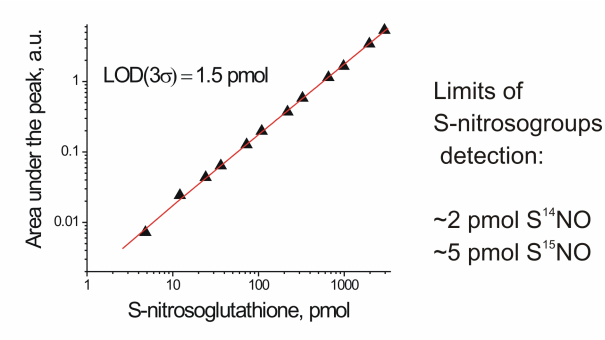

REFERENCES

(1) Marozkina, N. V.; Gaston, B. *Biochim Biophys Acta* **2012**, *1820*, 722-729.
(2) Mayer, B.; Pfeiffer, S.; Schrammel, A.; Koesling, D.; Schmidt, K.; Brunner, F. *J Biol Chem* **1998**, *273*, 3264-3270.
(3) Foster, M. W.; Hess, D. T.; Stamler, J. S. *Trends Mol Med* **2009**, *15*, 391-404.
(4) Gaston, B.; Singel, D.; Doctor, A.; Stamler, J. S. *Am J Respir Crit Care Med* **2006**, *173*, 1186-1193.
(5) Gow, A. J.; Chen, Q.; Hess, D. T.; Day, B. J.; Ischiropoulos, H.; Stamler, J. S. *J Biol Chem* **2002**, *277*, 9637-9640.
(6) Paige, J. S.; Xu, G.; Stancevic, B.; Jaffrey, S. R. *Chem Biol* **2008**, *15*, 1307-1316.
(7) Seth, D.; Hausladen, A.; Wang, Y.-J.; Stamler, J. S. *Science* **2012**, *336*, 470-473.
(8) Husain, M.; Jones-Carson, J.; Song, M.; McCollister, B. D.; Bourret, T. J.; Vazquez-Torres, A. *Proc Natl Acad Sci U S A* **2010**, *107*, 14396-14401.
(9) Yun, B. W.; Feechan, A.; Yin, M.; Saidi, N. B.; Le Bihan, T.; Yu, M.; Moore, J. W.; Kang, J. G.; Kwon, E.; Spoel, S. H.; Pallas, J. A.; Loake, G. J. *Nature* **2011**, *478*, 264-268.
(10) Straub, A. C.; Lohman, A. W.; Billaud, M.; Johnstone, S. R.; Dwyer, S. T.; Lee, M. Y.; Bortz, P. S.; Best, A. K.; Columbus, L.; Gaston, B. *Nature* **2012**, *491*, 473-477.
(11) Nott, A.; Watson, P. M.; Robinson, J. D.; Crepaldi, L.; Riccio, A. *Nature* **2008**, *455*, 411-U467.
(12) Benhar, M.; Forrester, M. T.; Hess, D. T.; Stamler, J. S. *Science* **2008**, *320*, 1050-1054.
(13) Gu, Z. Z.; Kaul, M.; Yan, B. X.; Kridel, S. J.; Cui, J. K.; Strongin, A.; Smith, J. W.; Liddington, R. C.; Lipton, S. A. *Science* **2002**, *297*, 1186-1190.
(14) Whalen, E. J.; Foster, M. W.; Matsumoto, A.; Ozawa, K.; Violin, J. D.; Que, L. G.; Nelson, C. D.; Benhar, M.; Keys, J. R.; Rockman, H. A.; Koch, W. J.; Daaka, Y.; Lefkowitz, R. J.; Stamler, J. S. *Cell* **2007**, *129*, 511-522.
(15) Abrams, A. J.; Farooq, A.; Wang, G. *Biochemistry* **2011**, *50*, 3405-3407.
(16) Colussi, C.; Mozzetta, C.; Gurtner, A.; Illi, B.; Rosati, J.; Straino, S.; Ragone, G.; Pescatori, M.; Zaccagnini, G.; Antonini, A.; Minetti, G.; Martelli, F.; Piaggio, G.; Gallinari, P.; Steinkulher, C.; Clementi, E.; Dell'Aversana, C.; Altucci, L.; Mai, A.; Capogrossi, M. C.; Puri, P. L.; Gaetano, C. *Proc Natl Acad Sci U S A* **2008**, *105*, 19183-19187.
(17) Gonzalez, D. R.; Treuer, A.; Sun, Q. A.; Stamler, J. S.; Hare, J. M. *J Cardiovasc Pharmacol* **2009**, *54*, 188-195.
(18) Ozawa, K.; Whalen, E. J.; Nelson, C. D.; Mu, Y.; Hess, D. T.; Lefkowitz, R. J.; Stamler, J. S. *Mol Cell* **2008**, *31*, 395-405.

(19) Moya, M. P.; Gow, A. J.; Califf, R. M.; Goldberg, R. N.; Stamler, J. S. *The Lancet* **2002**, *360*, 141-143.
(20) Snyder, A. H.; McPherson, M. E.; Hunt, J. F.; Johnson, M.; Stamler, J. S.; Gaston, B. *Am J Respir Crit Care Med* **2002**, *165*, 922-926.
(21) Lim, K. H.; Ancrile, B. B.; Kashatus, D. F.; Counter, C. M. *Nature* **2008**, *452*, 646-U611.
(22) Marozkina, N. V.; Wei, C.; Yemen, S.; Wallrabe, H.; Nagji, A. S.; Liu, L.; Morozkina, T.; Jones, D. R.; Gaston, B. *Am J Respir Cell Mol Biol* **2012**, *46*, 63-70.
(23) Tada, Y.; Spoel, S. H.; Pajerowska-Mukhtar, K.; Mou, Z. L.; Song, J. Q.; Wang, C.; Zuo, J. R.; Dong, X. N. *Science* **2008**, *321*, 952-956.
(24) Bryan, N. S.; Rassaf, T.; Maloney, R. E.; Rodriguez, C. M.; Saijo, F.; Rodriguez, J. R.; Feelisch, M. *Proc Natl Acad Sci U S A* **2004**, *101*, 4308-4313.
(25) Gow, A.; Doctor, A.; Mannick, J.; Gaston, B. *J Chromatogr B* **2007**, *851*, 140-151.
(26) Drummond, J. W.; Volz, A.; Ehhalt, D. H. *J Atmos Chem* **1985**, *2*, 287-306.
(27) Dickerson, R. R.; Delany, A. C.; Wartburg, A. F. *Rev Sci Instrum* **1984**, *55*, 1995-1998.
(28) Wang, X.; Bryan, N. S.; MacArthur, P. H.; Rodriguez, J.; Gladwin, M. T.; Feelisch, M. *J Biol Chem* **2006**, *281*, 26994-27002.
(29) Hess, D. T.; Matsumoto, A.; Kim, S. O.; Marshall, H. E.; Stamler, J. S. *Nat Rev Mol Cell Biol* **2005**, *6*, 150-166.
(30) Hausladen, A.; Rafikov, R.; Angelo, M.; Singel, D. J.; Nudler, E.; Stamler, J. S. *Proc Natl Acad Sci U S A* **2007**, *104*, 2157-2162.
(31) Palmer, L. A.; Gaston, B. *Nitric Oxide, Part F* **2008**, *440*, 157-176.
(32) Feelisch, M.; Rassaf, T.; Mnaimneh, S.; Singh, N.; Bryan, N. S.; Jourd'heuil, D.; Kelm, M. *FASEB J* **2002**, *16*, 1775-1785.
(33) Marley, R.; Feelisch, M.; Holt, S.; Moore, K. *Free radical res* **2000**, *32*, 1-9.
(34) Fontijn, A.; Sabadell, A. J.; Ronco, R. J. *Anal Chem* **1970**, *42*, 575-579.
(35) Clyne, M.; Thrush, B.; Wayne, R. *Trans Faraday Soc* **1964**, *60*, 359-370.
(36) Clough, P. N.; Thrush, B. A. *Trans Faraday Soc* **1967**, *63*, 915-925.
(37) Bateman, R. M.; Ellis, C. G.; Freeman, D. J. *Clin chem* **2002**, *48*, 570-573.
(38) Fritsch, T.; Brouzos, P.; Heinrich, K.; Kelm, M.; Rassaf, T.; Hering, P.; Kleinbongard, P.; Murtz, M. *Nitric Oxide* **2008**, *19*, 50-56.
(39) Yang, X.; Bondonno, C. P.; Indrawan, A.; Hodgson, J. M.; Croft, K. D. *Free Radical Bio Med* **2013**, *56*, 1-8.
(40) Yi, J.; Namjou, K.; Zahran, Z. N.; McCann, P. J.; Richter-Addo, G. B. *Nitric Oxide* **2006**, *15*, 154-162.
(41) Kosterev, A. A.; Malinovsky, A. L.; Tittel, F. K.; Gmachl, C.; Capasso, F.; Sivco, D. L.; Baillargeon, J. N.; Hutchinson, A. L.; Cho, A. Y. *Appl. Opt.* **2001**, *40*, 5522-5529.
(42) Halmer, D.; von Basum, G.; Horstjann, M.; Hering, P.; Murtz, M. *Isotopes Environ Health Stud* **2005**, *41*, 303-311.
(43) Heinrich, K.; Fritsch, T.; Hering, P.; Mürtz, M. *Appl Phys B* **2009**, *95*, 281-286.
(44) Kluczynski, P.; Lundqvist, S.; Westberg, J.; Axner, O. *Appl Phys B* **2011**, *103*, 451-459.
(45) Elia, A.; Lugarà, P.; Di Franco, C.; Spagnolo, V. In *Nitric Oxide*, McCarthy, H. O.; Coulter, J. A., Eds.; Humana Press, 2011, pp 115-133.
(46) Rothman, L.; Gordon, I.; Babikov, Y.; Barbe, A.; Chris Benner, D.; Bernath, P.; Birk, M.; Bizzocchi, L.; Boudon, V.; Brown, L. *J Quant Spectrosc Ra* **2013**, *130*, 4-50.
(47) Berden, G.; Peeters, R.; Meijer, G. *Int Rev Phys Chem* **2000**, *19*, 565-607.
(48) O'Keefe, A.; Deacon, D. A. G. *Rev. Sci. Instrum.* **1988**, *59*, 2544-2551.

(49) Romanini, D.; Lehmann, K. K. *J. Chem. Phys.* **1993**, *99*, 6287-6301.
(50) Romanini, D.; Gambogi, J.; Lehmann, K. K. In *50'th International Symposium on Molecular Spectroscopy*: Ohio State University, Columbus OH, 1995.
(51) Romanini, D.; Kachanov, A. A.; Sadeghi, N.; Stoeckel, F. *Chem. Phys. Lett.* **1997**, *264*, 316-322.
(52) Paldus, B. A.; Harb, C. C.; Spence, T. G.; Zare, R. N.; Gmachl, C.; Capasso, F.; Sivco, D. L.; Baillargeon, J. N.; Hutchinson, A. L.; Cho, A. Y. *Opt. Lett.* **2000**, *25*, 666-668.
(53) Romanini, D.; Lehmann, K. K. *J Chem Phys* **1993**, *99*, 6287-6301.
(54) Fritsch, T.; Brouzos, P.; Heinrich, K.; Kelm, M.; Rassaf, T.; Hering, P.; Kleinbongard, P.; Mürtz, M. *Nitric Oxide* **2008**, *19*, 50-56.
(55) Marquardt, D. W. *J Soc Ind Appl Math* **1963**, *11*, 431-441.
(56) Bevington, P. R.; Robinson, D. K. *Data reduction and error analysis for the physical sciences*; McGraw-Hill New York, 1969; Vol. 336.
(57) Lehmann, K. K.; Huang, H. In *Frontiers of Molecular Spectroscopy*, Laane, J., Ed., 2008, pp 624-658.
(58) Huang, H.; Lehmann, K. K. *J Phys Chem A* **2011**, *115*, 9411-9421.
(59) Reich, M.; Schieder, R.; Clar, H. J.; Winnewisser, G. *Appl. Opt.* **1986**, *25*, 130-135.
(60) Spencer, M. N.; Chackerian, C.; Giver, L. P.; Brown, L. R. *J Mol Spectrosc* **1994**, *165*, 506-524.
(61) Hart, T. W. *Tetrahedron Lett* **1985**, *26*, 2013-2016.
(62) Broniowska, K. A.; Diers, A. R.; Hogg, N. *BBA- Gen Subjects* **2013**, *1830*, 3173-3181.
(63) Stamler, J. S.; Simon, D. I.; Osborne, J. A.; Mullins, M. E.; Jaraki, O.; Michel, T.; Singel, D. J.; Loscalzo, J. *Proc Nat Acad Sci USA* **1992**, *89*, 444-448.
(64) Gaston, B.; Reilly, J.; Drazen, J. M.; Fackler, J.; Ramdev, P.; Arnelle, D.; Mullins, M. E.; Sugarbaker, D. J.; Chee, C.; Singel, D. J. *Proc Nat Acad Sci USA* **1993**, *90*, 10957-10961.
(65) Fang, K.; Ragsdale, N. V.; Carey, R. M.; MacDonald, T.; Gaston, B. *Biochem Biophys Res Co* **1998**, *252*, 535-540.
(66) Allan, D. W. *P IEEE* **1966**, *54*, 221-230.
(67) Fiorin, V.; Borthwick, D.; King, D. In *Model Systems in Catalysis*, Rioux, R., Ed.; Springer New York, 2010, pp 175-201.
(68) Kishi, K.; Roberts, M. *P Roy Soc Lond A. Mat* **1976**, *352*, 289-302.
(69) Brown, W. A.; King, D. A. *J Phys Chem B* **2000**, *104*, 2578-2595.
(70) Pope, R. S.; Wolf, P. J. *J Mol Spectrosc* **2001**, *208*, 153-160.

Appendix B: Important Tables of Statistics:

Pressure broadening coefficients from literature:

HWHM Pressure Broadening Coefficients for R(13/2) in MHz/Torr		
	Ω = ½	**Ω = 3/2**
Self[13]	2.438	2.643
Air[13]	2.205	2.327
He[12]	2.008	2.185

Transit time broadening:

$$\Delta\nu = \frac{0.4v_{\perp}}{w} = \frac{0.4\sqrt{\frac{2kT}{\mu}}}{w}$$

[10](??)

(From equation 3.63 in Demtröder). For w = 0.63 mm we obtain 280 kHz.

Cavity mode spacing

Transverse: 135.2 MHz

Longitudinal (FSR): 428 MHz

Mirror diameter: 12.7 mm

Mirror radii of curvature: ∞ (input), 100 cm (output)

Spacing: 35 cm

Compatibility of NO with materials[26]

This table is provided for common metals, plastics, and O-ring materials

S = satisfactory; C = conditional, U = unsatisfactory, I = Insufficient data

Material	**Compatibility**	**Material**	**Compatibility**
Brass	U	Carbon Steel	S
Stainless Steel	S	Aluminum	C
Zinc	I	Copper	S
Monel	S	Kel-F	S
Teflon	S	Tefzel	S
Kynar	S	PVC	S
Polycarbonate	S	Viton	S
Kalrez	S	Buna-N	U
Neoprene	U	Polyurethane	I

For NO_2, produced by reaction of NO with O_2:

Material	**Compatibility**	**Material**	**Compatibility**
Brass	U	Carbon Steel	S
Stainless Steel	S	Aluminum	C
Zinc	I	Copper	U
Monel	S	Kel-F	S
Teflon	S	Tefzel	S
Kynar	U	PVC	U
Polycarbonate	I	Viton	U
Kalrez	C	Buna-N	U
Neoprene	U	Polyurethane	U

Indices of refraction at HeNe (632 nm) and IR (5263 nm)[27]

Medium	n at 632.8 nm	n at 5263 nm	dn/dλ at 5263 nm (μm^{-1})
CaF_2	1.43289	1.39571	-0.0127
BaF_2	1.47327	1.44932	-0.00667
MgF_2	1.37698	1.32948	-0.0179
Sapphire	1.75787	1.60267	-0.0620
ZnSe	2.59073	2.42858	-0.00362
Ge	N/A (opaque)	4.01469	-0.00531
Si	N/A (opaque)	3.42151	-0.00197

Appendix C: Comparison of NO spectroscopic detection methods

Method	Advantages	Disadvantages	Limit of sensitivity
Laser absorption spectroscopy	Absolute measurement of concentration	High number of passes needed to detect change in laser power over laser noise	0.164 ppbv[22]
Photo-acoustic spectroscopy	Ease and tolerance of alignment	High power laser required, not absolute method	4.9 ppbv[23]
Faraday Modulation Spectroscopy	Smaller optical path required	Limited to small J values	0.38 ppbv[24]
Cavity Ringdown Spectroscopy	Compact and insensitive to laser power fluctuations	Difficulty in alignment of cavity	< 0.7 ppbv[4]

The above values for limit of sensitivity are for 1 s of averaging time.

Appendix D: Strong Transitions

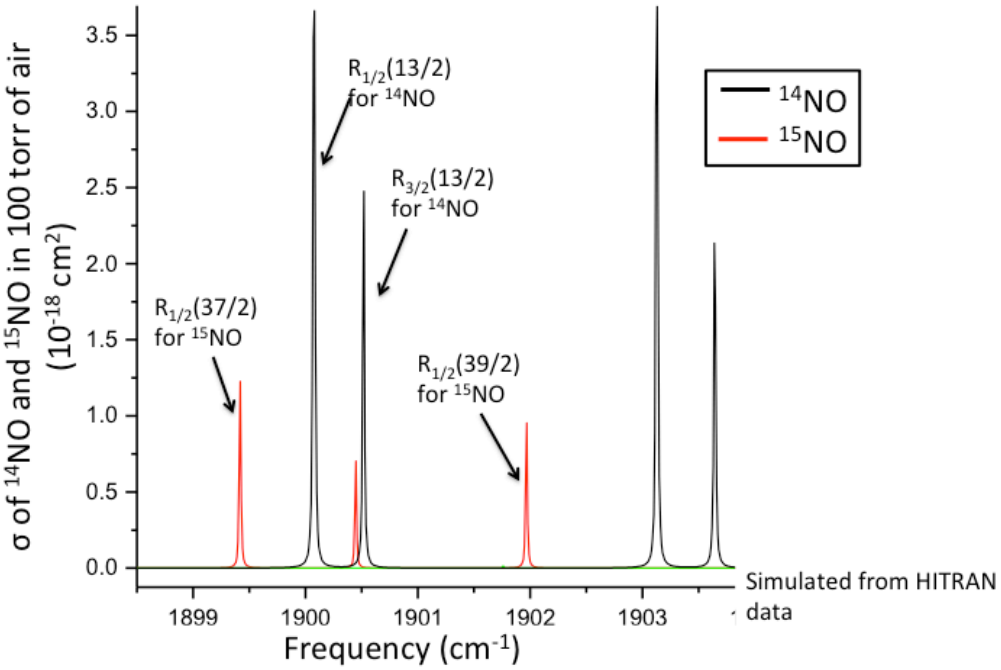

Figure 80: Strongest transitions of ^{14}NO, and nearby ^{15}NO lines.

Wavenumber	Relative Freq (MHz)	Line intens. cm^-1 per (molec per cm^2)	Einstein A Hz	Air broad. width cm^-1 per	Self-broad. width cm^-1 per atm	Type (P or R)	Lower state J	Lambda doublet state	Integrated Line Intens. cm^-1 per (molec per cm^2)	Weighted position of line center v (cm^-1)	Δv to prev. line (MHz)
14NO											
R 13/2; X1/2 e											81516.3704
1900.070578	0.00	2.03E-20	1.46E+00	0.0559	0.0618	R	6.5	e			
1900.070593	0.45	2.32E-20	1.49E+00	0.0559	0.0618	R	6.5	e			
1900.070596	0.54	1.77E-20	1.46E+00	0.0559	0.0618	R	6.5	e	6.19E-20	1900.070607	
1900.072052	44.22	3.67E-22	3.03E-02	0.0559	0.0618	R	6.5	e			
1900.072147	47.07	3.67E-22	2.65E-02	0.0559	0.0618	R	6.5	e			
R 13/2; X1/2 f											329.539859
1900.079250	0.00	3.67E-22	2.65E-02	0.0559	0.0618	R	6.5	f			
1900.079550	9.00	3.67E-22	3.03E-02	0.0559	0.0618	R	6.5	f			
1900.081594	70.32	2.32E-20	1.49E+00	0.0559	0.0618	R	6.5	f	6.19E-20	1900.081591	
1900.081628	71.34	1.77E-20	1.46E+00	0.0559	0.0618	R	6.5	f			
1900.081636	71.58	2.03E-20	1.46E+00	0.0559	0.0618	R	6.5	f			
R 13/2; X3/2											13079.0142
1900.516783	0.00	1.956E-22	2.56E-02	0.059	0.0671	R	6.5	e			
1900.516903	3.60	1.956E-22	2.92E-02	0.059	0.0671	R	6.5	e			
1900.517093	9.30	1.238E-20	1.44E+00	0.059	0.0671	R	6.5	e			
1900.517196	12.39	1.080E-20	1.41E+00	0.059	0.0671	R	6.5	e			
1900.517276	14.79	9.429E-21	1.41E+00	0.059	0.0671	R	6.5	e	6.600E-20	1900.517559	
1900.517453	20.10	1.956E-22	2.56E-02	0.059	0.0671	R	6.5	f			
1900.517688	27.15	1.956E-22	2.92E-02	0.059	0.0671	R	6.5	f			
1900.517870	32.61	1.238E-20	1.44E+00	0.059	0.0671	R	6.5	f			
1900.517956	35.19	1.080E-20	1.41E+00	0.059	0.0671	R	6.5	f			
1900.518033	37.50	9.429E-21	1.41E+00	0.059	0.0671	R	6.5	f			
15NO:											
R 37/2; X1/2											
1899.4149	0	5.80E-23	1.79E+00	0.0499	0.0595	R	18.5	e	1.16E-22		
1899.4223	222	5.80E-23	1.79E+00	0.0499	0.0595	R	18.5	f		1899.4186	
											30864
R 37/2; X3/2											
1900.4457	0	3.00E-23	1.787	0.0518	0.0629	R	18.5	e	6.00E-23	1900.4474	
1900.4491	102	3.00E-23	1.788	0.0518	0.0629	R	18.5	f			

Figure 81: Numerical data for R(13/2) transitions of 14NO

Bibliography

1. A. Okeefe and D. A. G. Deacon, Review of Scientific Instruments **59** (12), 2544-2551 (1988).
2. B. Mayer, S. Pfeiffer, A. Schrammel, D. Koesling, K. Schmidt and F. Brunner, Journal of Biological Chemistry **273** (6), 3264-3270 (1998).
3. M. W. Foster, D. T. Hess and J. S. Stamler, Trends in Molecular Medicine **15** (9), 391-404 (2009).
4. A. A. Kosterev, A. L. Malinovsky, F. K. Tittel, C. Gmachl, F. Capasso, D. L. Sivco, J. N. Baillargeon, A. L. Hutchinson and A. Y. Cho, Applied Optics **40** (30) (2001).
5. D. R. Herriott and H. J. Schulte, Applied Optics **4** (8), 883-889 (1965).

6. F. Dominec, in *Inkscape*, edited by Laser_resonator_stability.svg (Wikimedia Commons, 2007), Vol. nominally 722 × 673 pixels, file size: 38 KB, pp. A diagram of stability of an optical resonator. The parameters g1 and g2 are obtained as g1=1-(L/R1) and g2=1-(L/R2), where R is the mirror curvature radius and L is the resonator length.
7. S. Forget and N. Paillard, edited by fig19.jpg (Université Paris - Nord 13, Optical Resonators and Gaussian Beams: Laser and non-linear optics, 2007), Vol. 499x399; 781.2 kB.
8. A. Yariv, *Quantum Electronics*, 2nd ed. (John Wiley & Sons, 1975).
9. R. D. Nelson Jr, D. R. Lide Jr and A. A. Maryott, 1967.
10. W. Demtröder, *Laser Spectroscopy*. (Springer, 2008).
11. H. M. Foley, Physical Review **69** (11-12), 616-628 (1946).
12. R. S. Pope and P. J. Wolf, Journal of Molecular Spectroscopy **208** (2), 153-160 (2001).
13. L. S. Rothman, D. Jacquemart, A. Barbe, D. C. Benner, M. Birk, L. R. Brown, M. R. Carleer, C. Chackerian, K. Chance, L. H. Coudert, V. Dana, V. M. Devi, J. M. Flaud, R. R. Gamache, A. Goldman, J. M. Hartmann, K. W. Jucks, A. G. Maki, J. Y. Mandin, S. T. Massie, J. Orphal, A. Perrin, C. P. Rinsland, M. A. H. Smith, J. Tennyson, R. N. Tolchenov, R. A. Toth, J. Vander Auwera, P. Varanasi and G. Wagner, Journal of Quantitative Spectroscopy & Radiative Transfer **96** (2), 139-204 (2005).
14. M. Reich, R. Schieder, H. J. Clar and G. Winnewisser, Applied Optics **25** (1) (1986).
15. , edited by W. N. Haynes (Taylor & Francis, 2014).
16. E. E. Whiting, Journal of Quantitative Spectroscopy and Radiative Transfer **8** (6), 1379-1384 (1968).
17. R. H. Dicke, Physical Review **89** (2), 472-473 (1953).
18. J. Domyslawska, S. Wojtewicz, A. Cygan, K. Bielska, D. Lisak, P. Maslowski, R. S. Trawinski and R. Ciurylo, Journal of Chemical Physics **139** (19) (2013).
19. F. Ramian, (Rohde & Schwarz, 2012), pp. 16.
20. W. J. Riley, *Handbook of Frequency Stability Analysis*. (Hamilton Technical Services, Beaufort, SC, 2007).
21. G. Giusfredi, S. Bartalini, S. Borri, P. Cancio, I. Galli, D. Mazzotti and P. De Natale, Physical Review Letters **104** (11) (2010).
22. J. B. McManus, D. D. Nelson, S. C. Herndon, J. H. Shorter, M. S. Zahniser, S. Blaser, L. Hvozdara, A. Muller, M. Giovannini and J. Faist, Applied Physics B-Lasers and Optics **85** (2-3), 235-241 (2006).
23. L. Dong, V. Spagnolo, R. Lewicki and F. K. Tittel, Optics Express **19** (24), 24037-24045 (2011).
24. R. Lewicki, J. H. Doty, III, R. F. Curl, F. K. Tittel and G. Wysocki, Proceedings of the National Academy of Sciences of the United States of America **106** (31), 12587-12592 (2009).
25. V. I. Stsiapura, V. K. Shuali, B. M. Gaston and K. K. Lehmann, Analytical Chemistry **87** (6), 3345-3353 (2015).
26. Praxair, (2012), Vol. 2015, pp. The compatibility data that follows has been compiled to assist in evaluating appropriate materials for use in handling various gases. It is extremely important that all gas control equipment be compatible with the gas being used. The use of a device that is not compatible may damage the unit and cause a leak that could result in property damage or personal injury. To reduce potentially dangerous situations, always check for the compatibility of materials before using any gases in your gas control equipment.
27. M. Polyanskiy, (2015), Vol. 2015.